EINDHOVEN
UNIVERSITY OF
TECHNOLOGY

Eindhoven University of Technology

MASTER

ALD metal oxides for passivating contacts in c-Si solar cells

Scheerder, R.W.H.S.

Award date:
2017

Link to publication

Disclaimer
This document contains a student thesis (bachelor's or master's), as authored by a student at Eindhoven University of Technology. Student theses are made available in the TU/e repository upon obtaining the required degree. The grade received is not published on the document as presented in the repository. The required complexity or quality of research of student theses may vary by program, and the required minimum study period may vary in duration.

General rights
Copyright and moral rights for the publications made accessible in the public portal are retained by the authors and/or other copyright owners and it is a condition of accessing publications that users recognise and abide by the legal requirements associated with these rights.

- Users may download and print one copy of any publication from the public portal for the purpose of private study or research.
- You may not further distribute the material or use it for any profit-making activity or commercial gain

Technische Universiteit Eindhoven
University of Technology

plasma & materials processing

ALD Metal Oxides for Passivating Contacts

in c-Si Solar Cells

R.W.H.S. Scheerder

March 1, 2017

Department of Applied Physics
Plasma and Materials Processing

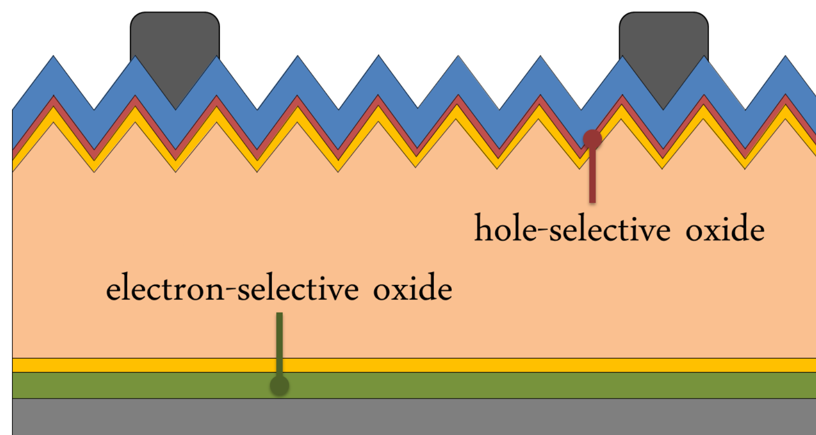

Supervisors:
Dr. ir. J. Melskens (TUe)
Ir. B.W.H. van de Loo (TUe)
Prof. dr. ir. W.M.M. Kessels (TUe)

Abstract

The silicon heterojunction (SHJ) solar cell is a very promising concept nowadays as a record efficiency of 26.6% has already been reached with this concept while the theoretical limit is 29%. The use of hydrogenated amorphous silicon (a-Si:H) in these cells limits the cell in performance by parasitic absorption, the low thermal stability, and the use of doped regions to induce selectivity. Furthermore, the record efficiency is achieved with a so-called interdigitated back contact SHJ cell which is a complex structure requiring a lot of processing steps. Transparent metal oxides that could passivate the crystalline silicon (c-Si) surface and, at the same time, induce selectivity for one type of charge carrier would be the ideal passivating contact material. This is why passivating, selective, transparent and stable metal oxides, that could also decrease the process complexity, are the topic of this research. Atomic layer deposition (ALD) is an ideal deposition method to control thickness and uniformity of such metal oxides. Moreover, it enables low temperature and "soft" deposition of these materials.
In this work, a new metal oxide material was introduced as a potential hole-selective contact: ruthenium oxide (RuO_x). The thermal and chemical stability, high conductivity, and relatively high work function ($\geq 5\,eV$) were expected to make it a promising material for c-Si solar cells. An extensive material study was performed to evaluate its potential as hole-selective passivating contact. First, a thermal ALD process was developed to deposit RuO_x films with (ethylbenzene)(1,3-cyclohexadiene)Ru as (zero-valent) metal-organic precursor and O_2 as reactant. Polycrystalline RuO_x films with a rough surface and containing a Ru metal fraction were obtained over a temperature range of $150°C$ to $300°C$. By increasing the O_2 exposure time the O/Ru ratio could be increased. No carbon incorporation was detected and a H content between 4 at.% to 10 at.% was measured. Furthermore, the films had a resistivity of $\sim 3 \cdot 10^2\,\mu\Omega \cdot cm$, which is an order of magnitude higher than the bulk literature value, and a high carrier density $10^{21} - 10^{23}\,cm^{-3}$. This high carrier density was also the reason why the RuO_x had a high optical absorption coefficient. The deposited RuO_x films did not passivate the c-Si surface and the high absorption limited the potential as passivating contact material.
Recently, titanium oxide (TiO_x) was shown to be able to passivate the c-Si surface and it can potentially serve as hole-blocking when it is only a few nm in thickness. So TiO_x films, deposited with ALD, were investigated as electron-selective passivating contacts. It was concluded that amorphous TiO_x films deposited with a thermal ALD process gave the best passivation on n-type Si wafers. Furthermore, the best passivation performance was achieved with the metal-organic precursor titanium isopropoxide. It already passivated the c-Si surface in the as-deposited state as opposed to the two other precursors used. After 15 minutes of forming gas anneal treatment at $300°C$ record minority carrier lifetime $\tau_{eff} \approx 2.0\,ms$ and a surface recombination current density $J_0 = 12.3\,fA/cm^2$ with $\sim 5\,nm$ thick TiO_x films were achieved. The minimal contact resistivity of an Al/TiO_x/c-Si stack was $\rho_c = 0.4\,\Omega \cdot cm^2$ which could, together with the low J_0, lead to maximum solar cell efficiencies of around $\eta = 26-27\%$ in an idealized case. However, when using the ALD TiO_x films on cell level, the open-circuit voltage (suns-V_{oc}) values dropped significantly opposed to the excellent implied open-circuit voltage (iV_{oc}) values of these cells. This demonstrates by a lack of selectivity in the cells and it needs further investigation to establish the source of the problem.

Table of Contents

Abstract **I**

1 General Introduction **1**

1.1 Photovoltaics . . . 1

1.2 Silicon Solar Cells . . . 2

1.3 ALD for PV . . . 6

1.4 Project Goals . . . 7

2 Theory of Passivating Contacts **8**

2.1 Passivating layers . . . 9

2.2 Carrier Selectivity . . . 11

2.3 Evaluating Passivating Contacts . . . 12

3 Ruthenium Oxide **14**

3.1 Introduction . . . 15

3.1.1 Applications of Ruthenium Oxide . . . 15

3.1.2 ALD of Ruthenium and Ruthenium Oxide . . . 15

3.2 Experimental Details . . . 16

3.3 Process development . . . 17

3.3.1 ALD process . . . 17

3.3.2 Structural properties of RuO_x . . . 20

3.3.3 Temperature influence . . . 27

3.4 Optical and Electrical Properties of ALD RuO_x . . . 30

3.5 Passivation Qualities . . . 35

3.6 Conclusion and Outlook . . . 36

4 Titanium Oxide **38**

4.1 Introduction . . . 39

4.1.1 Background on Titanium Oxide in Solar Cell Applications . . . 39

4.1.2 Titanium Oxide as Passivating Contact . . . 39

4.2 Experimental Details 41
4.3 Results 44
4.3.1 TTIP ALD TiO_x Results 44
4.3.2 Solar Cell Concepts with Titanium Oxide 50
4.3.3 Comparison Titanium Precursors 53
4.4 Conclusion and Outlook 58

5 Overall Conclusion and Outlook **60**

Acknowledgements **63**

Appendix **64**

Bibliography **69**

Chapter 1

General Introduction

1.1 Photovoltaics

Using a renewable energy source is becoming a must with the conventional fossil fuels being limited. One way to create electricity is by using light from the sun, the virtually infinite power source, to convert photons into charge carriers. A photon with an energy equal to or higher than the band gap of a semiconductor material can be absorbed by exciting an electron to the conduction band leaving at the same time a hole in the valence band. These light-generated charge carriers induce a voltage in the device due to this photovoltaic effect and when they are extracted they generate a DC current thus giving rise to power generation.

In practice, nearly all photovoltaic energy conversion uses semiconductor material in the form of a *p*-*n* junction. A positively doped material, *p*-type, is in contact with a negatively doped material, *n*-type. This structure induces a depletion region with an intrinsic electric field which prohibits the majority carriers, being electrons for the *n*-type and holes for the *p*-type semiconductor, to diffuse to the other side. A schematic structure of a *p*-*n* solar cell is given in figure 1.1.1.

The process of light absorption creates an electron-hole pair, thus a majority and minority carrier are introduced in the *p*- and *n*-type material. The light-generated current can be extracted when the *n* and *p* side are connected by an external circuit and a current can flow. The minority carrier will only exist for a certain time given by the minority carrier lifetime before it recombines. This parameter will become important as it indicates the quality of the cell.

If these charge carriers are prohibited of leaving the solar cell device in open-circuit condition the collection of light-generated charge causes an increase in electrons in the *n*-type side and holes in the *p*-type side as minority carriers will be swept to the other side by the intrinsic electric field. This will decrease the effective electric field at the junction up to a point of equilibrium where a voltage exists over the *p*-*n* junction which is called the photovoltaic effect. The voltage across the cell required for this is called the open-circuit voltage V_{oc}.

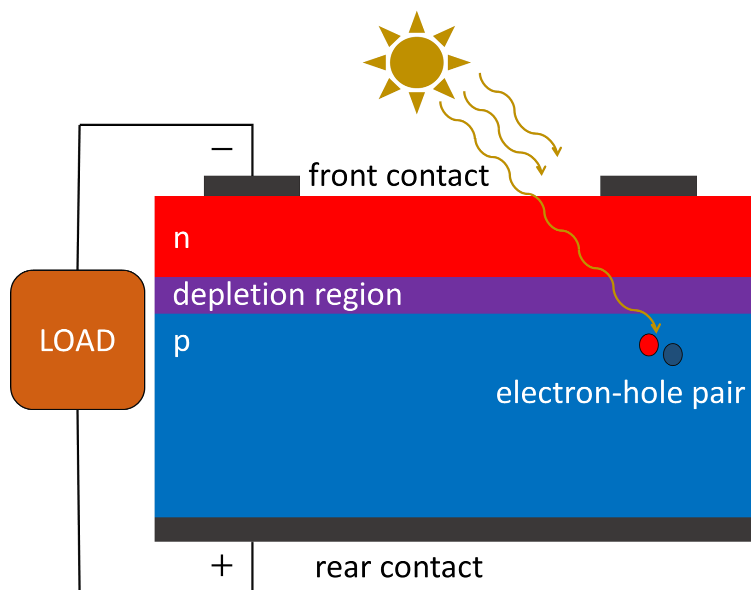

Figure 1.1.1: *Schematic of p-n junction solar cell. Sunlight creates light-generated charge carriers (electrons and holes) in the semiconductor material. These carriers can be collected to generate a current and the photovoltaic effect gives a voltage across the cell. The power generated can dissipate into the load and other parasitic resistances.*

1.2 Silicon Solar Cells

The cumulative installed photovoltaic (PV) capacity has been growing strongly in the last years due to the increasing global demand for sustainable energy. The PV market is over 90% based on silicon solar cells [1]. Its success comes from the cost effectiveness of the silicon based solar cells. These particular cells have a predicted fundamental limit of 29.4% efficiency [2] which is not yet reached (up to 26.6% on a practical cell size [3]). Although the market is dominated by crystalline silicon (c-Si) solar cells there are still several different types of solar cells. Record efficiencies are being recorded with for example; GaAs (Gallium Arsenide), InP (Indium Phosphide), CdTe (Cadmium Telluride) and CIGS (Copper Indium Gallium Selenide) solar cells with efficiencies above 20% [4]. Multijunction solar cells, where multiple *p*-*n* junctions in a stack of different semiconductors produce electrical current in response to different wavelengths, have a theoretical limit of 86.8% for infinite number of semiconductors [5]. Furthermore, perovskite solar cells are of high interest for research nowadays and efficiencies are increasing steadily, as can be seen in Figure 1.2.1.

With the industry being almost completely based around silicon solar cells the market will also be dominated by it. When looking at figure 1.2.1 the relative lesser increase in c-Si solar cell efficiency is noticeable but just a few tens of percentage increase can already improve the levelized cost of electricity (LCOE) a lot. The balance of system costs, which include the wiring, optics, mounting, batteries, etc., are relatively increasing more in the overall system price and thus reducing the needed surface area or the cost of the cell is of utmost importance. This will come down to further increase the conversion efficiency of silicon based solar cells which can be done by decreasing the recombination losses of the created electron-hole pairs resulting in an increase of open-circuit voltage. These recombination processes can occur in the silicon bulk and at the surface and are further elaborated on in

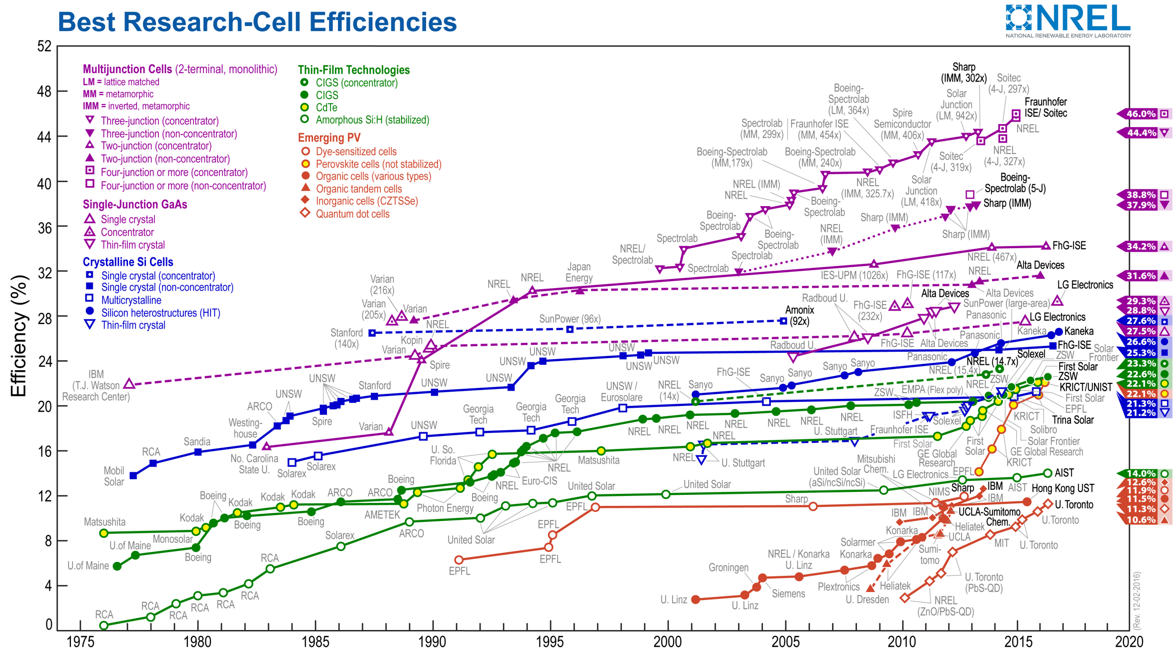

Figure 1.2.1: *Solar cell efficiency chart from 1976 to 2016 with record efficiencies indicated. The single crystalline silicon solar cells (without concentrator) are indicated with blue solid squares and heterojunction structured silicon cells are indicated with blue solid circles. (This plot is a courtesy of National Renewable Energy Laboratory, Golden, CO.)*

chapter 2. Furthermore, cheap and less complex cell structures contribute to the realization of highly efficient industrial solar cells. A brief overview of how the Si solar cell has developed throughout the last years with industrial cell structures as an example will be discussed.

Although p-type Czochralski (CZ) c-Si wafers have dominated the market, the most efficient cells are acquired with n-type silicon as bulk material [6]. Some properties of the n-type crystalline silicon such as, most importantly, the absence of boron-oxygen related light-induced degradation (LID) [6, 7] makes it more efficient as a base material. Furthermore, the n-type material exhibits enough strength against common impurities [8]. Commonly impurities in Si, like Fe, are positively charged and hence capture electrons more efficiently. Since the minority carriers in n-type Si are holes (rather than electrons), the minority carrier diffusion length is general larger in n-type, posing another benefit over p-type. With the benefits offered by n-type substrates it has become attractive to use these substrates in solar cell module technology. This being said about the bulk, the main contribution to the loss in lifetime of charge carriers is due to surface defects. Dangling silicon bonds, especially at the top surface, need to be reduced or else the surface recombination has a big detrimental effect on the efficiency. This is called the passivation of the Si surface.

As one can see in Figure 1.2.1, the 25.0% efficiency line of monocrystalline Si solar cells was already reached in 1999 by UNSW (University of New South Wales, AUS). These solar cells are also called homojunction solar cells, meaning that the p-n junction is formed within one type of base material with different doping. They consist of a c-Si base with an electron and hole-selective side induced by phosphorous and aluminium doping respectively. To reduce the back surface recombination an oppositely highly doped region at the back creates a p^+-p junction with the lower doped region of the bulk which induces an electric field, the Back

Surface Field (BSF). For the standard p-type CZ Si solar cell this would be a highly p^{++} Al doping, hence the name Al-BSF. Such a Al-BSF homojunction cell is shown in figure 1.2.2(a). Eventually, with a so-called PERL (passivated emitter and rear locally diffused) structure which shown in figure 1.2.2](b), the cell efficiency can increase up to 25.0% but the processing complexity increases significantly. The front contacts penetrate the anti-reflection coating (ARC) to extract charge carriers from the bulk, but these metal-silicon interfaces lead to significant recombination losses and heavily limit the efficiency of such a cell. Furthermore, higher doping levels induce more Auger recombination (explained in Chapter 2). This is currently the reason why the efficiency of a homojunction cell has not been strongly improved since [9].

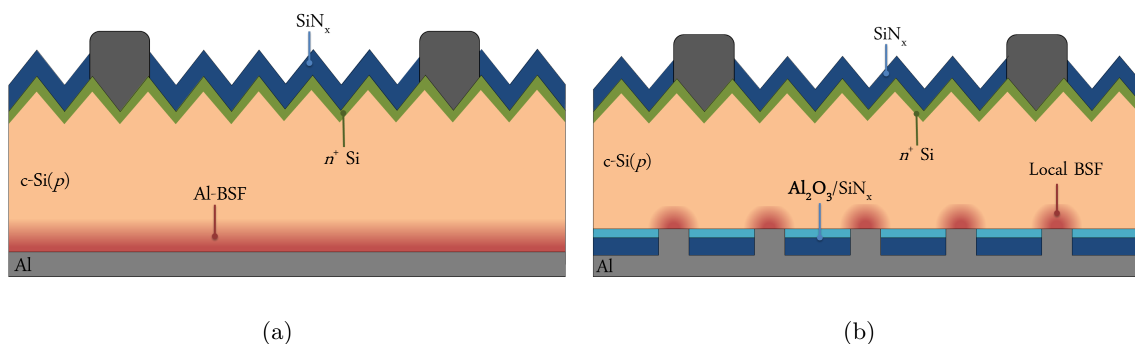

Figure 1.2.2: *Schematics of diffused homojunction cells [10]. In (a) an Al-BSF cell which is commonly mass-produced is shown, these have efficiencies of* $\sim 19-20\,\%$. *In (b) a more complex PERL cell is shown which render efficiencies approaching* $\sim 25.0\,\%$.

An alternative to the traditional homojunction c-Si solar cell is the silicon heterojunction (SHJ) solar cell. This particular cell consists of a c-Si bulk which is passivated on both sides with intrinsic (i) hydrogenated amorphous silicon (a-Si:H). The a-Si:H(i) is an excellent passivation layer for the c-Si which minimizes the surface recombination losses of the electron-hole pairs generated in the bulk. The charge carrier selectivity on the front and rear side is induced by p-type and n-type doped a-Si:H respectively. A transparent conductive oxide (TCO) is added to conduct the charge carriers to the metal contacts while avoiding significant parasitic absorption losses. The TCO is necessary, as opposed to the homojunction cells, because the mobility of charge carriers in the a-Si:H regions is very low compared to p^+ and the n^+ regions in the homojunction cells. The structure can be seen in figure 1.2.3(a).

With a so-called interdigitated back contact (IBC) structure the record efficiency of 26.6% has been reached by the Japanese Kaneka Company in 2016 [3] as can be seen in figure 1.2.1. Here only the rear side has metal conductor structures to omit the shadowing losses of the front metallization and thus the front layer only has to be an ARC. Interdigitated regions at the back with p and n dopants make these certain regions selective for holes or electrons respectively as is shown in figure 1.2.3(b). The interest in heterojunction cells keeps increasing in the PV community and with an efficiency of 26.6% reached the theoretical limit is coming closer and closer [9].

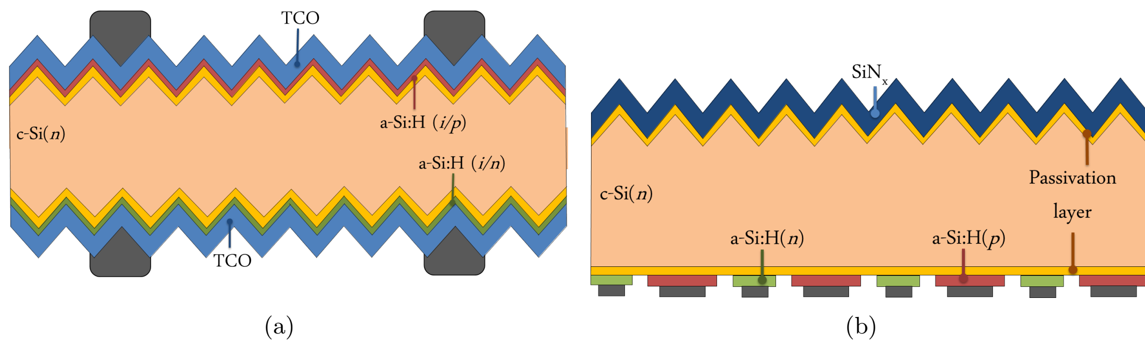

Figure 1.2.3: *Schematic of silicon heterojunction (SHJ) solar cells [10]. The passivation of the Si interface is done by the a-Si:H and the selectivity comes from the doping of this material either n or p-type. In (a) a schematic of a SHJ is shown with a TCO on the front and back carrying the current laterally to the contacts. In (b) an IBC-SHJ cell is shown with the interdigitated doped a-Si:H back contacts without front contacts.*

The a-Si:H in these SHJ cells can degrade by exposure to the atmosphere and high temperatures [9, 12]. Furthermore, it causes parasitic absorption as it has a rather low bandgap energy and lateral transport of charge carriers is diminished due to the low charge carrier mobility. Thus the research for more stable, process friendly and less absorbing *passivating contacts* becomes of interest. To introduce a commercially viable innovation with an increase in efficiency is becoming harder as the theoretical efficiency limit comes closer every time [2]. A full area passivating contact of a transparent material like metal oxides could potentially be this wanted innovation.

The aforementioned passivating contacts, a powerful concept for the further improvement of PV heterojunctions, are the topic of this thesis. These are thin layers (or stacks) which passivate the silicon interface and are at the same time selective for one type of charge carrier, being electrons or holes. The passivation is needed to decrease the surface defect density and thus to reduce the recombination of charge carriers at the silicon surface. A selective contact must induce a strong conductivity for one type of charge carrier. If both the passivating and selective qualities could be induced by a single transparent semiconductor material, for example a metal oxide, it could significantly reduce the number of processing steps and the processing complexity. An ideal structure is given by a schematic representation in figure 1.2.4. This relatively simple model needs no complex structures, no metal firing steps and just a few different materials. The long term goal is to create such an efficient metal oxide passivating contact cell.

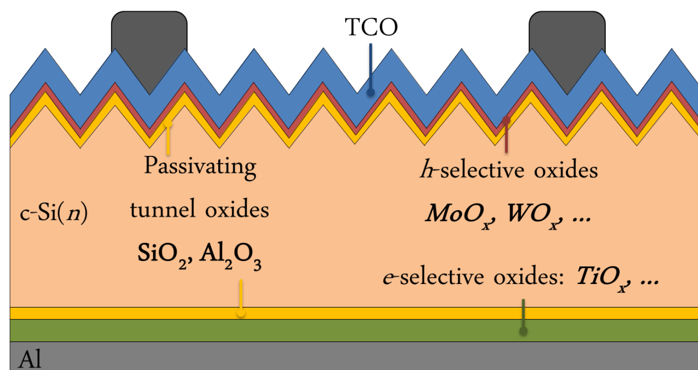

Figure 1.2.4: *Schematic of a metal oxide based cell is given with a full area electron-selective back contact, a transparent full area hole-selective front contact and a TCO. The passivating tunnel oxides could be introduced if the metal oxide is not sufficiently passivating the Si interface on its own [10].*

1.3 ALD for PV

As elaborated before, thin films or stacks of thin films are of interest which is where Atomic Layer Deposition (ALD) comes into play. ALD is a vapour based deposition technique for thin films which is based on sequential, self limiting surface reactions of gas phase chemicals, typically called precursors. Because of this self limiting aspect of the technique, atomic scale thickness control is possible. One ALD cycle consists of two or more sub-cycles, commonly referred to as half-cycles. Eventually, the surface is exposed to multiple ALD cycles to deposit a layer of desired thickness and composition. During the first half-cycle a vaporized precursor material reacts with the groups on the surface of the substrate. The newly formed surface groups need to be non-reactive with the precursor molecule which causes the self limiting character. After purging the reaction products and left-over precursor, a different reactant is introduced in the second half-cycle. This reactant reacts with the ligands of the adsorbed precursor molecule, again in a self-limiting manner.

The growth rate of the deposited material during an ALD process is generally expressed in growth per cycle (GPC). This way, by choosing the right amount of cycles, the desired thickness can be precisely controlled. A well-known ALD process is the deposition of Al_2O_3 with trimethylaluminum (TMA) as precursor and H_2O as reactant. A schematic of this ALD cycle is shown in figure 1.3.1.

With ALD, precise thickness control, uniformity, conformality, high purity, low deposition temperature and the soft deposition nature are some advantages in comparison with other methods like CVD or sputtering. These aspects of ALD make it an excellent candidate for the deposition of passivating contacts, and hence a powerful tool in the further improvement of silicon solar cells. Due to its apparent potential for instance in PV industry, demonstrated in typical small-scale research ALD reactors, there have been recent developments in the ALD field to enable high volume deposition. Techniques such as batch ALD and spatial ALD [14, 15], already being successfully demonstrated for Al_2O_3 ALD [16], are finding its way to the market and it is therefore expected to become a widespread application in the industry.

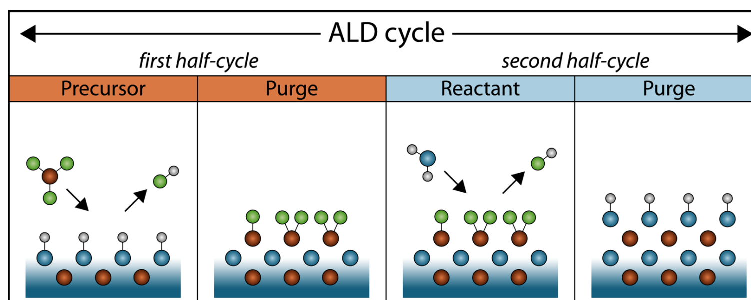

Figure 1.3.1: *Schematic of an ALD cycle for Al_2O_3. In the first half-cycle TMA is used as precursor which absorbs on the surface. In the second half-cycle H_2O is used as reactant to remove the precursor ligands. (This picture is a courtesy of the PMP group from TU/e.)*

1.4 Project Goals

In novel heterojunction solar cells new materials are needed to replace (doped) a-Si:H which suffers from parasitic absorption and instability. The goal of this project is to form selective and passivating metal oxide films or stacks to increase the efficiency or to simplify the c-Si solar cell production process and structure.

A material which has so far not been used in the c-Si PV is ruthenium oxide (RuO_x). Due to its relatively high work function, good conductivity and thermal and chemical stability it could be of interest as hole-selective material. However, an ALD process for RuO_x needs to be developed first and its potential as candidate hole-selective material has to be evaluated. A brief literature study on the ALD process of ruthenium's oxide and metal and properties together with the developed deposition process with the film analysis are discussed in Chapter 3.

Furthermore, titanium oxide (TiO_x) can have hole-blocking and passivating properties which is why this material is a potential electron-selective passivating contact. ALD is used to deposit the TiO_x films as film thickness and deposition method is shown to influence the quality. Another benefit is that very thin TiO_x layers already could exhibit these selective and passivating qualities so that a *nm* thin full-area back contact does not require any lateral transport of charge carriers. Research has been conducted on the material properties and the annealing effects on the passivating and carrier-selective qualities of the titanium oxide layers in silicon solar cells. This will be discussed in Chapter 4.

Chapter 2

Theory of Passivating Contacts

To increase the conversion efficiency of crystalline silicon solar cells it is important to reduce recombination losses of the charge carriers between the photo-active part of the solar cell and the metal contact. This is done ideally by decreasing surface defects at the interface and by making the contact selective for one type of charge carrier. If a contact layer has both these abilities it is called a passivating contact, as the selectivity is already part of the *contact* definition. In the next sections the background for passivation of the surface is given and the ways to make it selective for a certain charge carrier, i.e. electrons or holes, are discussed. First, the working principle of the charge transport in a solar cell is discussed, which serves as background for the selectivity.

Charge Carrier Transport in Solar Cells

A solar cell is commonly seen as a *p-n* junction with an intrinsic electric field. But this is not the operating point of the solar cell device as this electric field, which is present in the dark, is the consequence of thermal equilibrium and can effectively not do work on the charge carriers [18]. The driving forces of charge carrier transport in a semiconductor are the gradients of the quasi-Fermi levels which is shown next.

The two most important forces for solar cell operation, to which electrons and holes are exposed, are the electric force and the other "generalized" force which is related to the gradient of their concentration [17]. Following [18], if an electric field E is the only force applied then the charge current of particle i with a charge $z_i e$, e being the elementary charge, is:

$$j_{f,i} = z_i e n_i \mu_i E = \sigma_i E = -\frac{\sigma_i}{z_i e} \nabla (z_i e \cdot U) \tag{2.0.1}$$

where n_i is the concentration of carrier i, μ_i its mobility, $\sigma_i = z_i e n_i \mu_i$ the electrical conductivity and U is the electric potential. The unit of $[z_i e \cdot U]$ is now in the unit of energy J. When there is only a concentration gradient of particles i present and no electric field, the charge current is the charge times drift given by Fick's law of diffusion with diffusion coefficient D_i:

$$j_{d,i} = z_i e(-D_i \nabla n_i) = -z_i e n_i D_i \frac{\nabla n_i}{n_i}. \tag{2.0.2}$$

One can use Einstein's relation $D_i = \mu_i kT/e$ between the diffusion coefficient and the mobility, and thereafter the chemical potential $\phi_i - \phi_{i,0} = kTln(n_i/N_i)$ of particle i due to concentration non-uniformity with a standard value of the chemical potential $\phi_{i,0}$ and the effective density of states N_i to get:

$$j_{d,i} = -\frac{\sigma_i}{z_i e}\nabla\phi_i \tag{2.0.3}$$

because one can substitute $\nabla(n_i)/n_i$ by $\nabla(ln(n_i/N_i))$.

The resulting electric and chemical forces are now $-\nabla(z_i e \cdot U)$ and $-\nabla\phi_i$ respectively, with the latter causing diffusion. Adding these gives the resulting force $-\nabla(\phi_i + z_i e \cdot U) = -\nabla\eta_i$, η_i being the electrochemical potential of particles i. The identity of this electrochemical potential is (assuming Maxwell-Boltzmann statistics) by definition that of the Fermi energy. Under illumination a non-equilibrium situation arises in the semiconductor as excess charge carriers are created. Now the distribution of electrons and holes are described by their own quasi-Fermi levels, E_{Fn} and E_{Fp}, respectively. Leading to electrochemical potential for electrons $\eta_n = E_{F_n}$ and for holes $\eta_p = -E_{F_p}$. Combining this, the current in the case of electrons $i = n$ and $z_n = -1$ is:

$$j_n = \frac{\sigma_n}{e}\nabla E_{F_n} \tag{2.0.4}$$

and for holes $i = p$ and $z_p = 1$:

$$j_p = \frac{\sigma_p}{e}\nabla E_{F_p}. \tag{2.0.5}$$

2.1 Passivating layers

Excess charge carriers created by the absorption of light can recombine and lose their free energy. This process is caused by different recombination pathways or channels. Some of these processes are unavoidable as they are intrinsic to the material. More specifically, direct recombination is the term used for energy transfer to a photon and/or electron, and there is Auger recombination where energy is transferred to a third carrier. The latter is more prone to happen when there is a higher carrier concentration as it depends on three different elements to react. This is the case when the Si is highly doped thus making the Auger recombination a dominant process.
Extrinsic lattice defects, which form available energy states in the band gap of Si, are also pathways for recombination. This effect is named after Shockley, Read and Hall (SRH) who formulated the theory [19]. In particular at the surface, as the silicon lattice terminates, a high density of Si dangling bonds is natively present. These form defect levels and therefore induce strong SRH recombination [10]. The goal is now to reduce the recombination rate at the surface U_s which can be done in several ways.

One way of doing this is via *chemical passivation* where a layer is deposited onto the silicon surface. This layer can be bonded to the dangling bonds of the Si and moreover can

release hydrogen which can passivate the remaining defects. This hydrogen can effuse to the interface by a post-deposition annealing treatment, possibly in a hydrogen rich gas, when the hydrogen is not already actively passivating after the deposition. The passivation layers need to exhibit few defects themselves in the band gap of c-Si, therefore materials with low impurity content and a wide band gap are the most successful. This is also why placing a metal directly on the Si causes large recombination losses as it has no band gap and these available energy states gives rise to significant amount of carrier recombination.
Typical materials used as a chemical passivation layer are thermally grown SiO_2 [20], a-Si:H and ALD Al_2O_3 [21].

Another way to reduce U_s is to reduce either the electron or hole concentrations at the surface. Such reduction can be achieved by band bending in the Si energy band diagram near the Si top surface. Fixed charge in a passivation layer can exhibit this band bending and is known as *field-effect passivation*. For example, ALD Al_2O_3 films have a strong negative fixed charge density Q_f [22] while SiN_x has a strong positive Q_f. The fixed charge induces a space charge region at the interface which leads to band bending in the c-Si. In figure 2.1.1, as taken from [10], an example is given for a fixed negative charge inducing upwards band bending thus reducing the electron concentration at the surface. The three stated recombination processes and the surface defect states D_{it} are indicated.

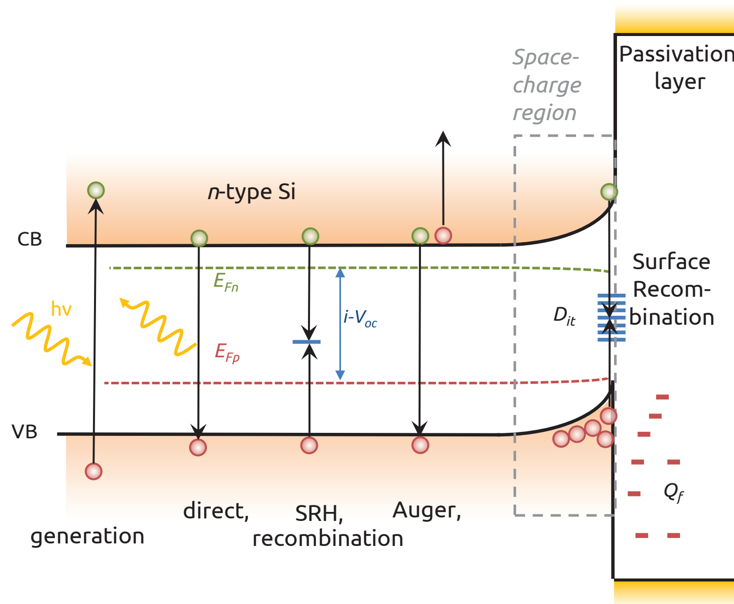

Figure 2.1.1: *Schematic band diagram of a passivated silicon surface, the band gap, valence band (VB), conduction band (CB) and quasi Fermi levels E_{Fn} and E_{Fp} are given. The recombination processes of the excess carriers which can take place (direct, SRH and Auger) are indicated. Also, a high density of defect states D_{it} at the interface which cause surface recombination are drawn. These can be passivated by a layer which reduces the D_{it} (chemical passivation). A negatively fixed charge induces space charge and upwards band bending so that the electron concentration reduces at the interface and thus reducing chance of recombination [10].*

2.2 Carrier Selectivity

The possibility to make a passivating layer carrier selective as well is an upcoming field of high interest in the PV industry. The layer has to act like a selective membrane for either electrons or holes. In order to be carrier selective the film must induce a strong asymmetry in the electron current j_n and hole current j_p. As is apparent from equations 2.0.4 and 2.0.5, selective transport can result from different conductivities of electrons and holes in the contact. This is also the reason why a *p-n* junction works as a solar cell as the doping provides good selective conductivity; the fact that it also induces a built-in electric field is not the main factor in charge separation. To achieve this asymmetry in currents also other methods could be applied, as doping causes more Auger recombination.

One way to get selectivity is by *band alignment*. A wide band gap material on the c-Si with little or no offset to either the conduction or valence band has good conductivity for electrons or holes respectively. It does need a large offset to the other band which is why the wide band gap is needed, this greatly reduces the hole or electron current for a large valence or conduction band offset, respectively.

A different way to create selectivity is by *induced band bending*. In the previous section band bending by fixed charge is given as a passivation scheme but it also aids in selectivity. This can also be induced by a high work function, or a high electron affinity, of the material deposited on the c-Si. The electron affinity, used to determine the band offsets with Anderson's rule of semiconductor-semiconductor junctions, gives the energy between the lowest conduction band state and the vacuum level. When the two semiconductors align the vacuum level, the offsets between their conduction and valence bands can be determined by this rule and Poisson's equation calculates the shape of the bending. If the work function of a material deposited on c-Si is high enough this would induce upward band bending rendering hole-selectivity. The bandgap of c-Si is $E_g = 1.12\,eV$ and its work function is $\approx 4\,eV$ which would need a work function $> 5.1\,eV$ to induce upward band bending.
In figure 2.2.1 the two discussed paths to selectivity are schematically shown.

One can see the gradient in the quasi-Fermi levels for holes and electrons. Where they come together, on the right side of the figure, a metal contact (or TCO) is typically used. If this gradient is high then the conductivity for this type of carrier is low for a given current. The quasi-Fermi level for the carrier to be extracted should be as flat as possible by this rule. In figure (a) one can see the band alignment to the conduction band which renders the contact electron-selective. In figure (b) one can see the upward band bending at the c-Si surface by a high work function leading to inversion, which causes hole-selectivity.

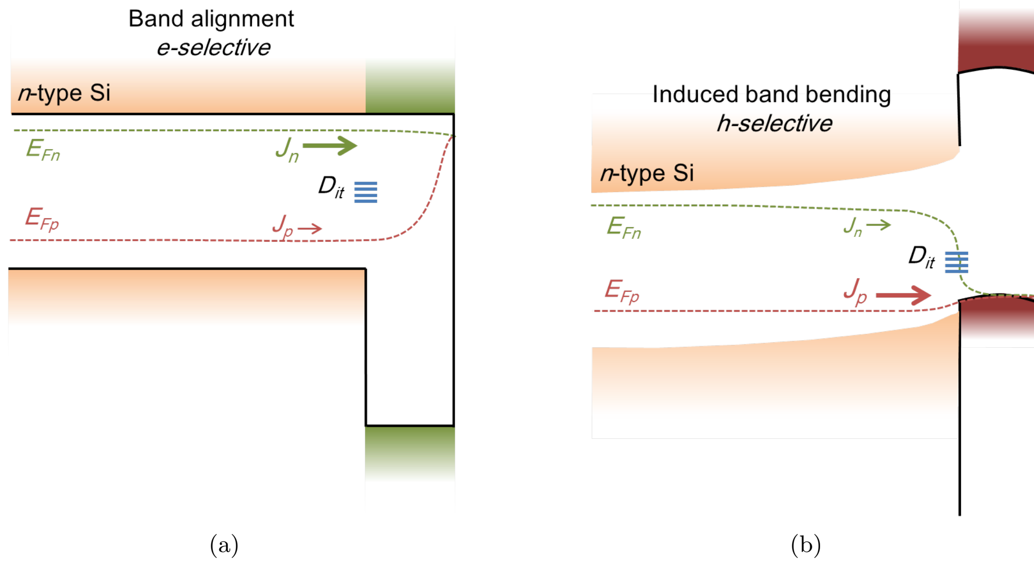

(a)

(b)

Figure 2.2.1: *Schematic representation of the introduced selectivity schemes taken from [10]. No other layers, free charge or defect states are drawn for simplicity. In (a) band alignment of the conduction bands of the n-type Si and a metal oxide rendering it electron selective is shown. In (b) upwards band bending induced by a high work function of a metal oxide film rendering the contact hole selective is shown.*

2.3 Evaluating Passivating Contacts

To evaluate the quality of a passivating contact some requirements need to be met. The important figures of merit that can be obtained experimentally corresponding to passivation and selectivity are [10]:

- The contact resistivity ρ_c. This should be as low as possible for the charge carrier the contact is made for, thus being an indicator for the conductivity of the majority carriers.
- The recombination current density J_0 which should be as low as possible. This is an indicator for the conductivity of the minority carriers. J_0 is inversely proportional to the effective lifetime of these minority charge carriers (τ_{eff}) which is a measure for the passivation quality.

The contact resistivity can influence the power one can get out the device. The ratio of the maximum obtainable power, being $P = I \cdot V$, to the $V_{oc} \cdot I_{sc}$ product is the fill factor (FF). Here V_{oc} is the open circuit voltage and I_{sc} the short circuit current. The resistivity ρ_c takes into account the internal losses due to series and shunt resistance and is thus in relation to the FF. The recombination current limits this V_{oc} which thus also limits the power obtainable from the device. With these two parameters an upper bound for the efficiency of a solar cell featuring a full area passivating contact can be calculated. The simulation approach, given by Melskens et al. [11], to calculate the efficiency accounts for optical losses and also for Auger recombination. An intrinsic Si wafer with a high resistivity of $10^6\,\Omega \cdot cm$ is used as bulk to simplify the results. The plot as function of J_0 and ρ_c is given in figure 2.3.1.

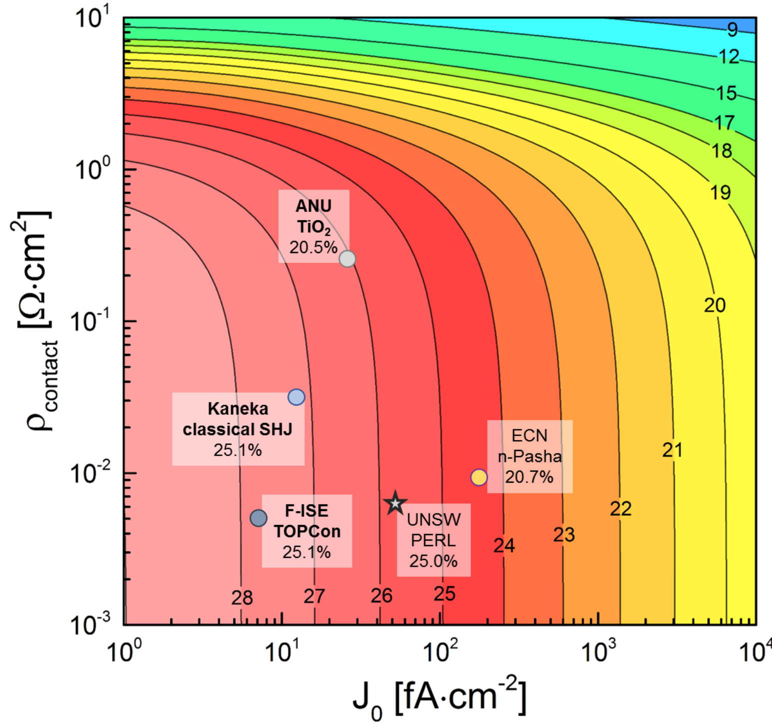

Figure 2.3.1: *The upper bounds of the solar cell efficiency with a full area passivating contact are indicated by the iso-efficiency lines which are a function of J_0 and ρ_c [11]. This way the contour plot can be constructed. Several data points of cells or cell precursors are given for comparison in the plot along with the efficiency of the full cell. These include the UNSW PERL cell [23], ECN n-Pasha cell, the classical SHJ concept [24], the TOPCon concept [25] and a TiO_2 contact from ANU [58].*

The maximum open circuit voltage one could obtain is the energy difference of the quasi-Fermi levels in illuminated state, this is called the implied open circuit voltage (iV_{oc}), which is also indicated in figure 2.1.1. This value can be obtained by measuring the average excess carrier concentration which is in relation to the photoconductance. The iV_{oc} is given by [26]:

$$iV_{oc} = \frac{kT}{q} \ln\left(\frac{\Delta n(N_A + \Delta n)}{n_i^2}\right). \tag{2.3.1}$$

Here, kT/q is the thermal voltage, n_i the equilibrium intrinsic carrier density, N_A is the base doping and Δn the minority carrier concentration in non-equilibrium.
However, the V_{oc} one measures from the device could be lowered by recombination current as the contact is not selective enough or Ohmic losses in the contact occur. The selectivity can then be qualified by the difference $\Delta V = iV_{oc} - V_{oc}$.

Chapter 3

Ruthenium Oxide

Abstract: Ruthenium oxide (RuO_x) is expected to have a high work function which could possibly render the RuO_x films as a hole-selective contact in silicon solar cells. This property could be used in novel SHJ solar cells in which the RuO_x layers need to be deposited on the Si wafer. ALD is a promising technique for RuO_x deposition as it is a soft deposition with excellent thickness and composition control which can be important in terms of desired film properties. RuO_x films were deposited with ALD using the zero-valent metal-organic (ethylbenzene)(1,3-cyclohexadiene)Ru (EBCHDRu) precursor and O_2 gas, within a temperature range of $150°C$ to $300°C$. Polycrystalline RuO_x films with a rough surface and containing a Ru metal fraction were initially deposited in the Volmer-Weber growth mode (island growth) over the whole temperature range. By increasing the O_2 exposure time the O/Ru ratio can be increased. No carbon contaminations are detected with RBS or XPS and a H content between 4% to 10% was measured with elastic recoil detection. Furthermore, the optical and electrical properties were determined with spectroscopic ellipsometry, four point probe and Hall measurements. These show that the film has a high conductivity, $\sim 338\,\mu\Omega \cdot cm$, and high carrier density. This high carrier density as well as the Ru metal fraction in the film is also the reason why the RuO_x has a high absorption coefficient. The deposited RuO_x films do not passivate the c-Si surface and the large absorption limits the potential of this material as passivating contact.

3.1 Introduction

3.1.1 Applications of Ruthenium Oxide

Ruthenium (Ru) is a transition metal, meaning it has a partially filled d sub-shell [28], belonging to the platinum group. Ruthenium is a versatile metal used as hardener in alloys and has many electronic or catalytic applications. Some applications include wear-resistant electrical contacts, electrodes in DRAM/FRAM or gate electrodes in MOSFETs [30].
Oxides of ruthenium are RuO_2 and RuO_4; RuO_2 is a solid at room temperature but RuO_4 becomes a volatile liquid. The latter is a strong oxidizer and could react with organic material which is potentially dangerous as it is gaseous at an elevated temperature of $40°C$.
Ruthenium is not totally unknown in the solar energy sector, some ruthenium-complexes are being used for energy conversion. For example an anionic ruthenium-terperydine complex called "Black Dye", which is used in dye-sensitized solar cells (DSSCs) [33], was introduced in 1999. This dye has a probability of around 80% to convert a photon into an electron.

Its most stable oxide RuO_2 is widely used in electronic applications and as catalyst. Its low resistivity, superior thermal and chemical stability, and catalytic activity make it an excellent electrode [29, 30]. It also has a very high capacitance and is therefore studied in the high-performance supercapacitor field [34]. In integrated circuits (IC), Ru and RuO_2 are used as efficient diffusion barriers [31, 32].
The reported (direct) band gap energy of the RuO_2 is around $2.2 - 2.4\,eV$ [34, 35] and it is believed to have a relatively high work function of $\geq 5\,eV$ [36] which would make it suitable for making a hole selective contact. Although the band gap is not that wide, the potentially high work function makes it a worthy candidate to investigate as passivating contact.

The goal of this project is to make a hole-selective passivating contact RuO_x film. From literature this material seems like a good candidate but has never been applied as contact in c-Si PV and, first of all, a method has to be found to deposit the metal oxide layer with ALD.
The precursor used for the ALD process is the zero-valent (ethylbenzene)(1,3-cyclohexadiene)Ru(0) (EBCHDRu, $C_{14}H_{18}Ru$) as seen in figure 3.1.1.

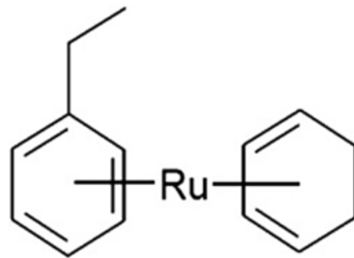

Figure 3.1.1: *The zero-valent Ru precursor (Et-Be)Ru(CHD) used in the ALD process reproduced from Hämäläinen et al. [37]*

3.1.2 ALD of Ruthenium and Ruthenium Oxide

There are several published Ru and RuO_2 ALD processes involving a large range of precursors [37]. There is less literature on zero-valent precursors and only one group from Korea,

where the used precursor is synthesised, has yet published on the ALD process with EBCHDRu [42, 43].

The most important problem one encounters with the Ru-precursors is a long nucleation delay. This is attributed to the reactant step where O_2 needs to dissociate into reactive O atoms and chemisorb onto the substrate, eventually reacting with the precursor ligands. Initially, the substrate material is not able to catalyse the dissociation of O_2 which can lead to long nucleation delays. When using a O_2 plasma step, O atoms are already present in the plasma which could prevent the delay. But experimentally it is experienced that Ru and RuO_2 films can be etched relatively easily by an oxygen plasma.

It is argued that zero-valent Ru-precursors do not suffer from long nucleation delays. This was first demonstrated for the ToRUS (RuO_4) precursor [39] where Ru metal films where deposited with thermal ALD using H_2O in a small temperature window around $100°C$. The zero-valent IMBCHRu shows negligible nucleation delay of Ru metal films on SiO_2 and TiN surfaces [41] which form continuous films at approximately $3\,nm$. In [42] the zero-valent EBCHDRu is shown to have near no nucleation delay for Ru and RuO_x ALD films. Although the reason for this behaviour has not been found yet, it was the reason the zero-valent EBCHDRu precursor was chosen for this project.

The common way to deposit metal oxide films with ALD is an A-B process, like in figure 1.3.1, with a metal organic precursor and an oxidation step with H_2O or O_2 gas or plasma. Molecular oxygen has been widely used as the reactant step for Ru and RuO_2 ALD, and no other reactants have been used in a RuO_2 A-B process to our knowledge. With the proposed ALD process it comes down to the oxidation of the metallic film. It is stated in [40] that O_2 can be incorporated at Ru defects like: vacancies, adatoms, surface roughness or domain boundaries. It is shown in [44] that the O coverage of the film is in relation with the exposure of O_2, being the time pressure product of the reactant step. It is expected that this needs to be increased to a certain level to get a metal oxide film. This is also demonstrated by Methaapanon et al. [45] where the effect of the oxygen exposure in Ru metal ALD was investigated with the $Ru(DMPD)_2$ precursor. For the purpose to work as a passivating contact a fully oxidized film without a metal fraction is required as metal is an efficient recombination reaction site. From prior work on MoO_x [46] and WO_x [47] it is known that stoichiometry is important as it can influence the work function. In aforementioned examples a higher oxygen content results in a higher work function which would preferably be as high as possible for the application as hole-selective contact.

In the next section the experimental approach is described. Subsequently, the results of the zero-valent EBCHDRu precursor in an A-B ALD process with O_2 gas as a reactant is presented.

3.2 Experimental Details

The process development of the RuO_x films was conducted in a home-built ALD reactor (ALDii). This reactor consists of a vacuum chamber connected to a gas inlet from the top; the gas inlet passes through an ICP plasma source. The pumping system consists of a rotary pump and a turbomolecular pump inducing base pressures in the order of $10^{-6} mbar$. The

valve to the pressure gauge to the chamber was closed at the precursor step to save it from parasitic deposition, at the reactant and purge steps it was used to measure the pressure in the chamber. The reactant step that was used operated at relatively high pressure (note that high exposure is expected to be essential for the forming of metal oxide) at around $p_{O_2} = 1\,mbar$ which was at the limit of the turbopump. Ar gas is used as a carrier gas during the precursor step flowing the EBCHDRu into the reactor chamber. A line with N_2 can be used to purge the chamber of reaction products and other species.
The precursor bubbler temperature is set to $90°C$ to get a sufficiently high vapour pressure [43], and the line temperature to $110°C$ to prevent condensation. The chamber wall can only be heated up to $100°C$.

Two inclined ports at the side of the chamber are used to mount the source and detector of a spectroscopic ellipsometry (SE) measurement device. This way *in-situ* measurements can be performed making use of a J.A. Woollam, Inc. M2000U ellipsometer to monitor the ALD growth.

n-type Czochralski (CZ) Si is used as substrate which has a native oxide layer (SiO_2) of $1.2 - 1.7\,nm$. At every run also a CZ Si wafer piece with a thermal oxide SiO_2 of around $450nm$ thick, which functions as a dielectric barrier for electrical measurements on the RuO_x films, is also placed in the reactor.

The chosen table temperature is $T_h = 200°C$ as the only reported ALD process with this precursor [43] was performed at a substrate temperatures of $185°C$ to $270°C$. Moreover, $200°C$ is a reasonable working temperature in the PV industry as some functional layers of a solar cell, especially a-Si:H, can be affected by high temperatures [12]. Note that the substrate table setting is not the effective substrate temperature which is by definition lower due to the temperature measurement in vacuum. This depends on multiple aspects of the reactor like pressure, size and the time a sample is placed on the table before deposition is started. The substrate temperature can be estimated with an *in-situ* SE model. The table temperature is varied over a wide range to determine the possible ALD window and the properties of these RuO_x films are studied which is elaborated in section 3.3.3.

3.3 Process development

3.3.1 ALD process

In previous studies on Ru and RuO_x ALD the nucleation delays and long dosing time form the main issues of this process. The zero-valent precursor should help overcome the nucleation delay as mentioned in 4.1.2. Long dosing times, taking from seconds to tens of seconds, contribute to the high exposure that is probably needed for metal oxide like films.
The first results obtained are with a thermal ALD recipe with an O_2 reactant step at a table temperature of $T_h = 200°C$. The pressure at the reactant step is kept constant in the upcoming results at the instrumental maximum of $p_{O_2} = 1\,mbar$. The precursor dosing time and reactant dosing time are $5\,s$ and $30\,s$, respectively. The purge times are taken longer than mentioned in literature to be sure that purging saturation is reached. The precursor purge is $5\,s$ and the reactant purge is $7\,s$ long.
The growth of the RuO_x films is monitored *in-situ* by SE every 10 cycles. The modelling

of the films is very complicated, as will be explained in section 4.3.2, so a mathematical B-Spline model is used to parametrize the dielectric function. This gives an estimation of the film thickness and optical constants. The growth curve of the first successful deposition is shown in figure 3.3.1.

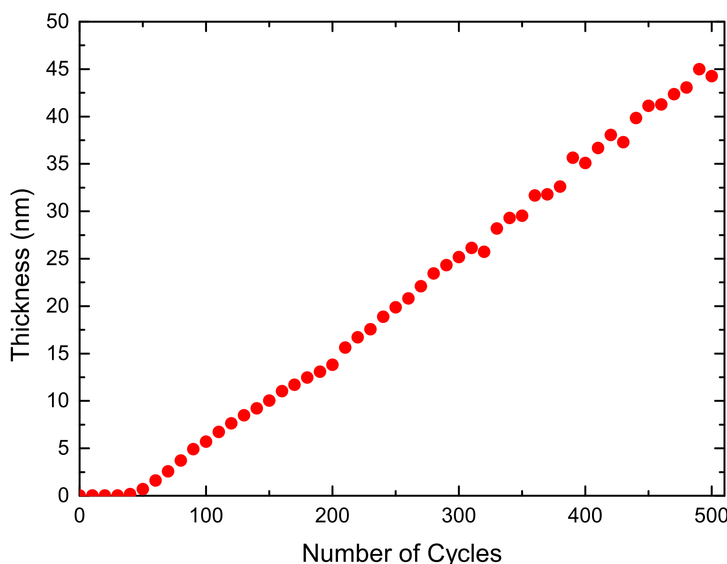

Figure 3.3.1: *Growth curve of 500 cycles of* $5\,s$ *precursor dosing and* $30\,s$ *oxygen dosing time as* RuO_x *ALD recipe at* $T_h = 200°C$*. The thickness is modelled with the mathematical B-Spline model.*

According to these data there is still a growth delay of ∼50 cycles. From the starting point at 50 cycles up to 300 cycles a GPC can be derived which is 0.96Å. Deviations in the measured GPC can be due to different processes run in between depositions, although conditioning of the chamber (1000 cycles of Al_2O_3 ALD and 500 cycles RuO_x ALD) was executed prior to each deposition series. Also, a certain error in the GPC determination should be taken into account for which the reason will be explained in section 4.3.2.
After acquiring the first growth one can eliminate the possibility of CVD effects by studying the effect of increasing purge times and precursor dosing without a reactant step. In this way, a self-limiting ALD process can be validated.
First, a recipe with a long precursor step of $15\,s$ with a purge step of $5\,s$ without a reactant step was done for 150 cycles on a bare substrate, no growth was observed. Afterwards a layer of RuO_x was deposited of $19.30\,nm$, then a precursor pulsing of $15\,s$ with a purge step of $5\,s$ was done for 100 cycles. Again, no growth was observed of the already present layer, thus the precursor without a reactant does not induce growth. The length of the purge steps are checked to be in saturation and the results are shown in the appendix figure 5.0.1.

After validating that it is indeed an ALD process, the saturation curves for precursor dosing and reactant dosing are experimentally determined. The precursor dosing was chosen to be alternated at a reactant dosing time of $30\,s$ which would suffice according to literature [43], although the process is developed on a different home made reactor as is done by Yeo et

al. For the ALDii reactor, at a table temperature of $T_h = 200°C$ and at a oxygen dosing pressure of $p_{O_2} = 1\,mbar$, the saturation curves are shown in figure 3.3.2. From the *in-situ* SE measurements one can estimate the substrate temperature which was typically around $180°C$, which is still different to the set temperature of $200°C$ even with the good thermal conductivity in the high pressure O_2 step.

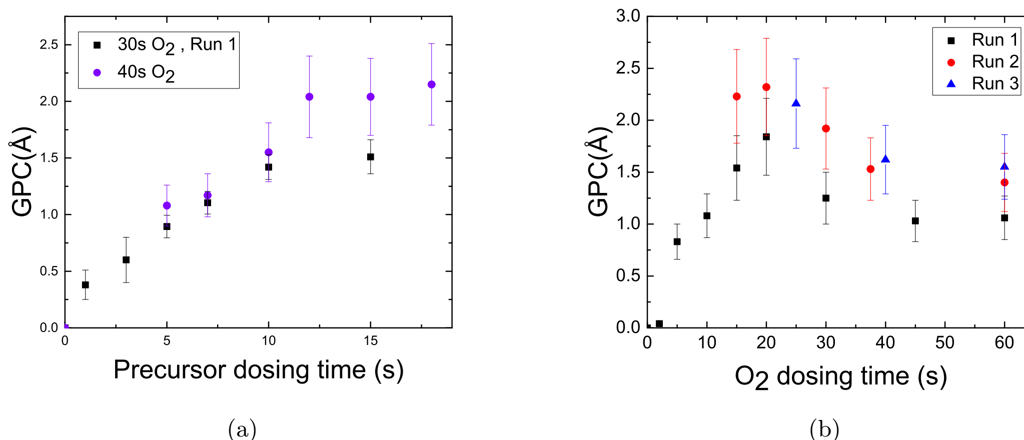

(a) (b)

Figure 3.3.2: *Saturation curves for precursor and reactant dose in the ALDii reactor where the substrate table is set to $T_h = 200°C$ and the oxygen pressure is kept constant at $p_{O_2} = 1\,mbar$. In (a) the saturation curve of the precursor dosing time at an oxygen reactant step of $30\,s$ is shown in black and for $40\,s$ oxygen in purple. In (b) the saturation curve of the oxygen dosing time at a precursor dosing step of $15\,s$ is shown. The data points have been taken from several different deposition runs while other activities have been undertaken in the reactor in between. A difference in absolute GPC can be observed.*

After the saturation curve of the precursor dosing time had been constructed for $30\,s$ oxygen dosing shown in figure 3.3.2(a) in black, $15\,s$ dosing time was chosen to be in saturation regime although no longer precursor dosing times have been measured. The O_2 dosing time shows a reproducible deviating trend from a standard saturation curve at around the $[15 - 30]s$ interval. The GPC increases significantly before reaching saturation after the $30\,s$ point. Therefore, $40\,s$ oxygen dosing time is chosen to make sure saturation is achieved. The saturation curve for the precursor dosing time was constructed again for a O_2 dosing time of $40\,s$. The result is shown in figure 3.3.2(a) in purple. One can conclude that $15\,s$ precursor dosing time is still well in the saturation regime as for $18\,s$ dosing the GPC does not significantly differentiate.
The ALD recipe for the RuO_x films is schematically shown in figure 3.3.3.

Now the ALD recipe is well defined, the question arises what kind of material is deposited. An extensive material analysis has been conducted on the influence of precursor dose and especially on the oxygen dose time. The behaviour of the O_2 saturation curve is particularly unusual, which calls for a systematic investigation of the deposited material. Therefore, several techniques like X-Ray Diffraction (XRD), Rutherford Backscattering Spectroscopy (RBS) together with Elastic Recoil Detection (ERD) and Scanning/Transmission Electron Microscopy (SEM/TEM), have been used to study the RuO_x ALD films.

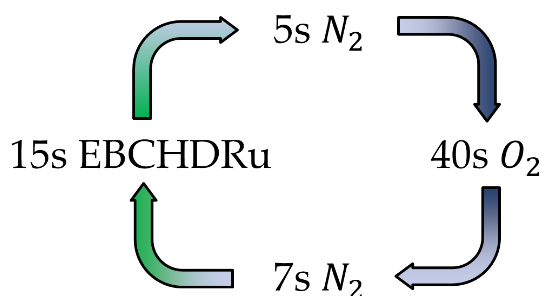

Figure 3.3.3: *A schematic representation of the ALD recipe used to deposit RuO_x films*

3.3.2 Structural properties of RuO_x

First, cross-sectional TEM images, figure 3.3.4, of the standard saturated recipe (figure 3.3.3) films were taken. A film of about $20\,nm$ ($19.43\,nm$ according to B-Spline model fit) is deposited on a CZ Si wafer with native oxide. On the RuO_x film an Al capping layer is evaporated to acquire a clear contrast in the TEM images.

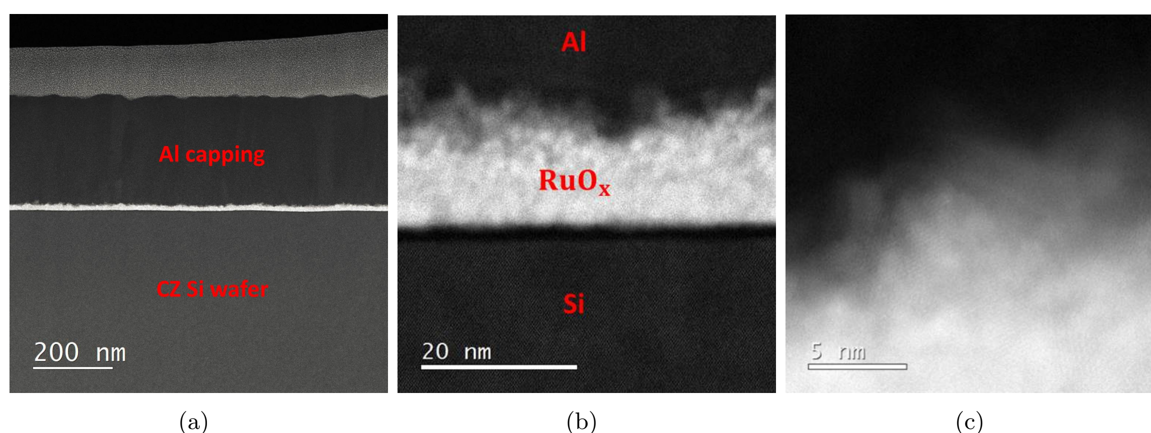

(a) (b) (c)

Figure 3.3.4: *Different magnifications of High-Angle Angular Dark Field (HAADF) TEM images, showing (a) the RuO_x layer sandwiched between the Si wafer and the Al capping layer, (b) the RuO_x film which has a rough surface and the atomic arrangement in the c-Si wafer, and (c) the top layer of the RuO_x film, illustrating the crystallinity and the rough surface morphology.*

Additionally, a high resolution TEM image is taken from this cross-section which is shown in figure 3.3.5.

In figure 3.3.4 (a) the RuO_x film in white is sandwiched between the CZ Si wafer and the Al capping layer. In (b) the rough surface of the film is noticeable which is in the order of a couple nm. Zooming in even further, shown in (c), a polycrystalline structure can be seen in the RuO_x film and the rough surface morphology. From figure 3.3.5 one can again see the polycrystalline structure and also measure the native oxide which has a thickness of $(1.93 \pm 0.08)\,nm$.
From these TEM images it is clear that the SE model fitting becomes problematic due to the surface roughness. The roughness is on the same order of magnitude of the total film thickness which could explain the deviating results per deposition on the same parameter settings.

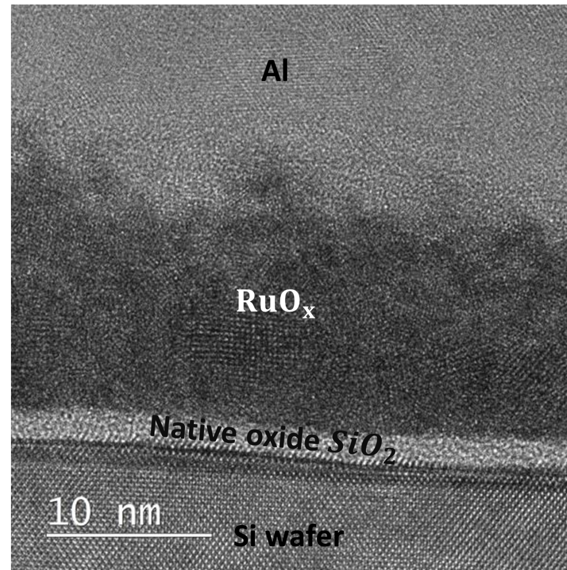

Figure 3.3.5: *High Resolution TEM (HRTEM) image clearly showing the polycrystallinity of the RuO_x layer and the native oxide of the Si wafer.*

If the thickness is measured on multiple points in the picture it is in agreement with that of the B-Spline model, concluding it can be used as a satisfying estimation of the layer thickness.

XRD can be used to determine which crystal orientations occur in the film. A PANalytical X'Pert Pro MRD system with an X-ray source of $Cu\ K\alpha 1 = 1.54$Å was used to perform $\omega - 2\Theta$ scans where the ω offset is 3 degrees to significantly reduce the crystalline silicon substrate's signal. A thickness series of 150/300/750/1500 cycles is deposited with the standard recipe (figure 3.3.3) as the film seems to change with thickness during the growth process. XRD measurements were performed systematically and the results are shown in figure 3.3.6.

The measured peaks correspond to certain crystalline orientations of RuO_2 which are indicated in green in figure 3.3.6. Increasing peak intensities are observed with increasing thickness for all the orientations of RuO_2. The results also show different peaks which do not belong to crystalline RuO_2, but originate from crystalline Ru metal indicated in purple. Hence, the films contain some fragments of Ru metal phases according to the XRD results. This metal phase is not the desired result of the ALD process as is discussed in section 3.1.2, since the goal is to deposit metal oxide RuO_x, as metal has very poor passivation qualities on a c-Si surface. From literature [38,44] the oxygen exposure ($time * pressure$) is credited a large role in the film composition. With increasing the oxygen exposure, which is increasing the O_2 dosing time as the pressure cannot be increased while using the turbopump, the formation of a more metal oxide-like film is expected. The oxygen exposure already seems to have a significant influence if one looks at the saturation curve in figure 3.3.2 (b). A RuO_x film deposited with a 25 s exposure, which is in the "bump" of the saturation curve, is also investigated, together with the 40 s standard recipe and an extended 60 s O_2 exposure.
XRD measurements are performed for these 3 films, which were deposited with 150 ALD cycles, to determine structural differences and see if the (crystalline) metal fraction decreases with a longer oxygen exposure. The film thicknesses are 25.90 nm, 19.43 nm and 18.63 nm respectively for 25 s, 40 s and 60 s O_2 dosing times, and the results are shown in figure 3.3.7

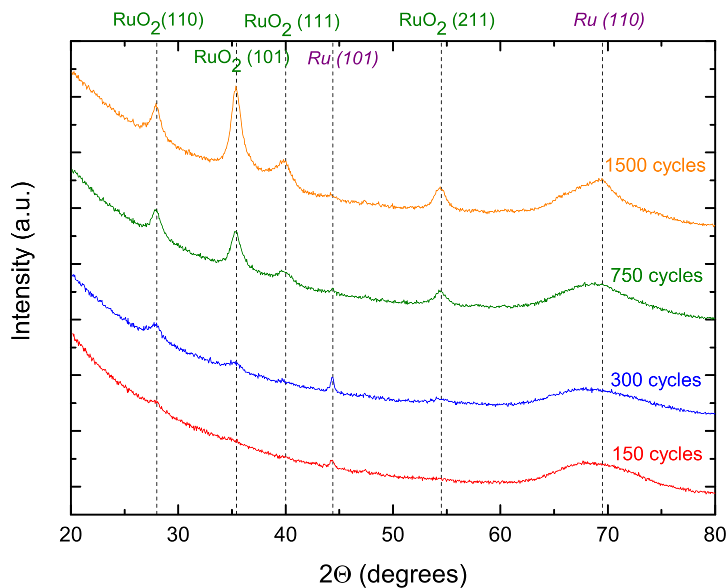

Figure 3.3.6: *XRD measurements on RuO_x films deposited with the standard recipe. The films were created with 150/300/750/1500 cycles on Si substrates with a native oxide. A match for the crystalline orientations and the 2Θ peak positions are found in literature [48].*

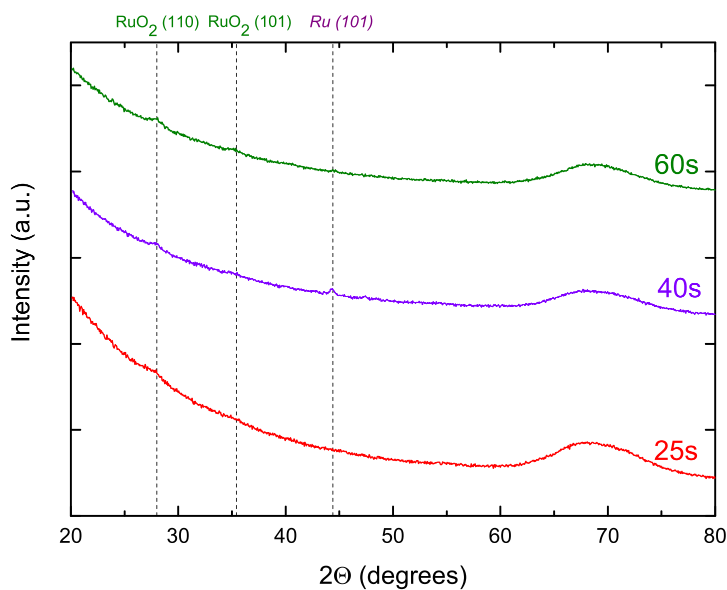

Figure 3.3.7: *XRD measurements on RuO_x films deposited with varying oxygen dosing times. The films were created with 150 cycles on a Si substrates with a native oxide. A match for the crystalline orientations and the 2Θ are found in the database [48].*

Just like one could observe in figure 3.3.6, the signals of the crystalline orientations are weak for a film created with 150 cycles. The difference between the standard recipe sample and the 60 s dosing sample with almost the same thickness is however significant. The Ru(101) metal peak disappears and the RuO_2 peaks seem to increase which would indicate a more metal oxide-like layer. There is still a possibility that the metal fraction is amorphous and not noticeable with XRD.
Furthermore, there are almost no crystalline peak signals noticeable for the 25 s O_2 dosing sample. This sample has a larger layer thickness, 25.9 nm as opposed to the others $\pm 20\,nm$, so the signal loss is not due to the fact that the film is too thin. Hence, this could indicate a more amorphous film.

To complement the XRD results, RBS and ERD measurements were performed on these samples to precisely determine the stoichiometric and elemental composition, hydrogen content and eventually the film density. A native oxide from the wafer causes an overestimation of the oxygen content in the film. A correction is performed with the assumption of an amorphous SiO_2 density $\rho_{SiO_2} = 2.2\,g/cm^3$ [49] and molar mass $M_{SiO_2} = 60.1\,g/mol$. The amount of native oxide SiO_2 is given by:

$$N_{SiO_2} = \frac{\rho_{SiO_2} \cdot N_A}{M_{SiO_2}} = 2.2 \cdot 10^{22}\, SiO_2\, molecules/cm^3. \tag{3.3.1}$$

In the previous equation $N_A = 6.02 \cdot 10^{23}$ is Avogadro's number. For SiO_2 (consisting of a Si atom and 2 O atoms) one can derive a correction factor for the oxygen content which is $2 \cdot N_{SiO_2} = 4.4 \cdot 10^{15}\, at/cm^2$ per nm native oxide. The correction factor is multiplied by the thickness of the native oxide, determined by SE.
The results are shown in the table 3.3.1 for the samples deposited with varying oxygen dosing times. Note that the films were exposed to the ambient after taken out of the reactor, stored and transported for the RBS measurement, so the influence of this on the stoichiometry cannot be neglected.

Table 3.3.1: *Properties of the RuO_x films deposited with varying oxygen dosing times of 25 s, 40 s and 60 s. The layer thickness and GPC are determined by SE. The amount of deposited Ru [at. nm^{-2} $cycle^{-1}$] and chemical composition were determined by RBS; the hydrogen content was determined by ERD. Carbon contamination in the bulk was below the RBS detection limit of 5 at% for all films. The accuracies for H, O and Ru are respectively 7%, 5% and 2%. Typical errors are indicated.*

O_2 dosing time (s)	Film thickness (nm)	GPC (Å)	O/Ru (-)	[H] ($at.\%$) ($\frac{at}{nm^2 \cdot cycle}$)	Deposition rate Ru (g/cm^3)	Mass density
25	25.9	2.16 ± 0.33	1.89 ± 0.10	9.4 ± 0.7	4.55 ± 0.08	5.8 ± 0.3
40	19.4	1.62 ± 0.33	1.98 ± 0.10	7.5 ± 0.5	3.53 ± 0.07	6.0 ± 0.3
60	18.6	1.55 ± 0.31	2.16 ± 0.10	6.1 ± 0.4	3.64 ± 0.07	6.6 ± 0.3

The density of the RuO_x films is lower than the RuO_2 bulk density of 6.97 g/cm^3 [49]. The 25 s sample is less dense and it has the lowest O/Ru ratio as well. With increasing oxygen exposure one can detect an increase in O/Ru ratio, which corresponds to a more oxide like-film as was expected. Furthermore, with the increase of oxygen dosing time one notices an increase in density and decrease in hydrogen content. This can be explained by the fact that a less dense film can incorporate more H atoms.
From this point on the choice is made to further investigate the 60 s recipe because the more oxide-like characteristic is preferable for the application as passivating contact. The XRD measurement does not show a Ru metal peak and the RBS measurement gives the highest O/Ru ratio of 2.16 which could be beneficial for a higher work function as stated in section 3.1.2.

Top view TEM images were made of the growth process of the 60 s O_2 dosing recipe to visualize the growth and better understand the process. Small windows were used to image the layer after varying the number of cycles where a 5 nm layer of SiO_2 was deposited beforehand with ALD to imitate the native oxide. In figure 3.3.8 the pictures are shown for 50/100/150/300/500 cycles of the RuO_x ALD process with a 60 s oxygen dosing step and a schematic of the TEM windows to clarify its structure.

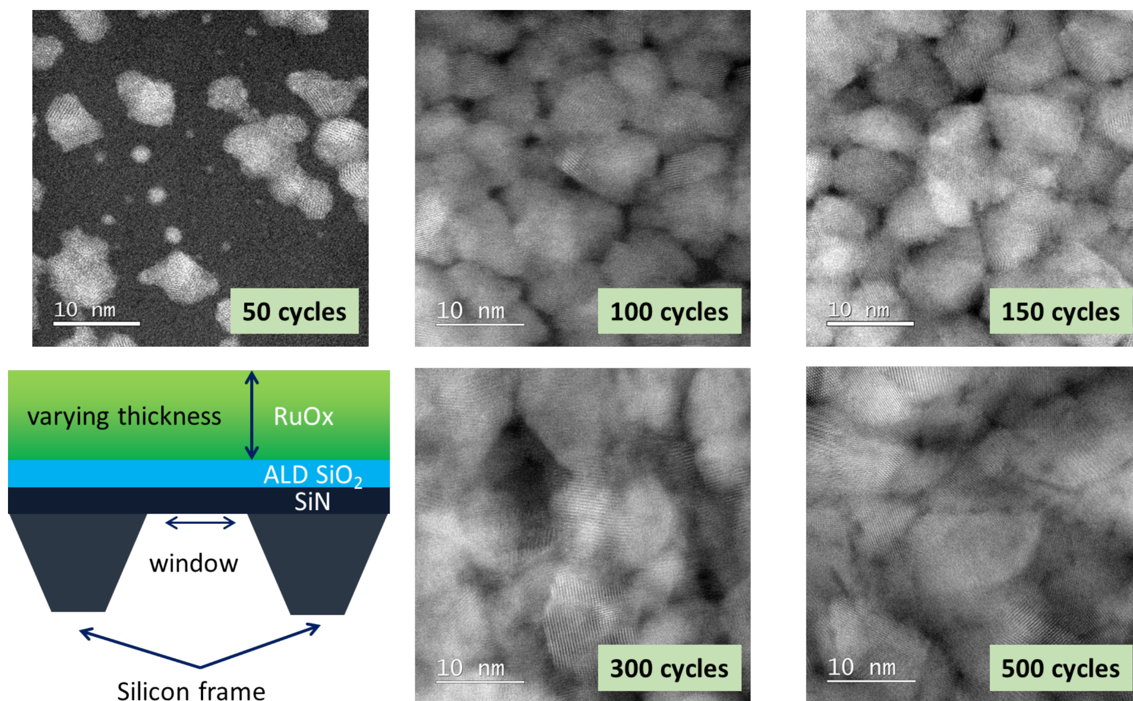

Figure 3.3.8: *HAADF-TEM images of varying number of cycles, indicated in the frame, with the 60 s O_2 dosing step RuO_x ALD. In the bottom left corner a schematic of the used TEM windows is shown.*

When looking at the image of 50 ALD cycles there is already a substantial amount of material deposited, but the SE measurements suggest that this would be the start of deposition at the end of some sort of delay. In the first frame of figure 3.3.8 it is obvious that these islands are polycrystalline and is also visible in the different polycrystalline grains in the thicker layers. From the start of the growth a nucleation site grows multiple crystalline phases. As the

growth continues, the islands grow in size to eventually merge and form a closed layer. This growth mode is called the Volmer-Weber mode [50] where adsorbate-adsorbate interaction is stronger than the adsorbate-surface interactions, hence the island growth.
Zooming out of this 50 cycles image, as shown in the left top corner of figure 3.3.9, one can again spot a substantial amount of deposition. The layer is far from closed and the growth seems to prefer sites where nucleation has occurred as it takes at least 100 cycles to close as the voids in the top view TEM, figure 3.3.9, seem to close. This leads to the rough surface as seen in figure 3.3.4. Furthermore, it explains why the SE data shows no growth in the first tens of cycles as seen in figure 3.3.1. The SE measurement spot, which is in the order of $1\,cm^2$, mostly measures the bare substrate at the start although there is already island growth. This is again a reason why the GPC is hard to determine as the growth is not uniform on the substrate.

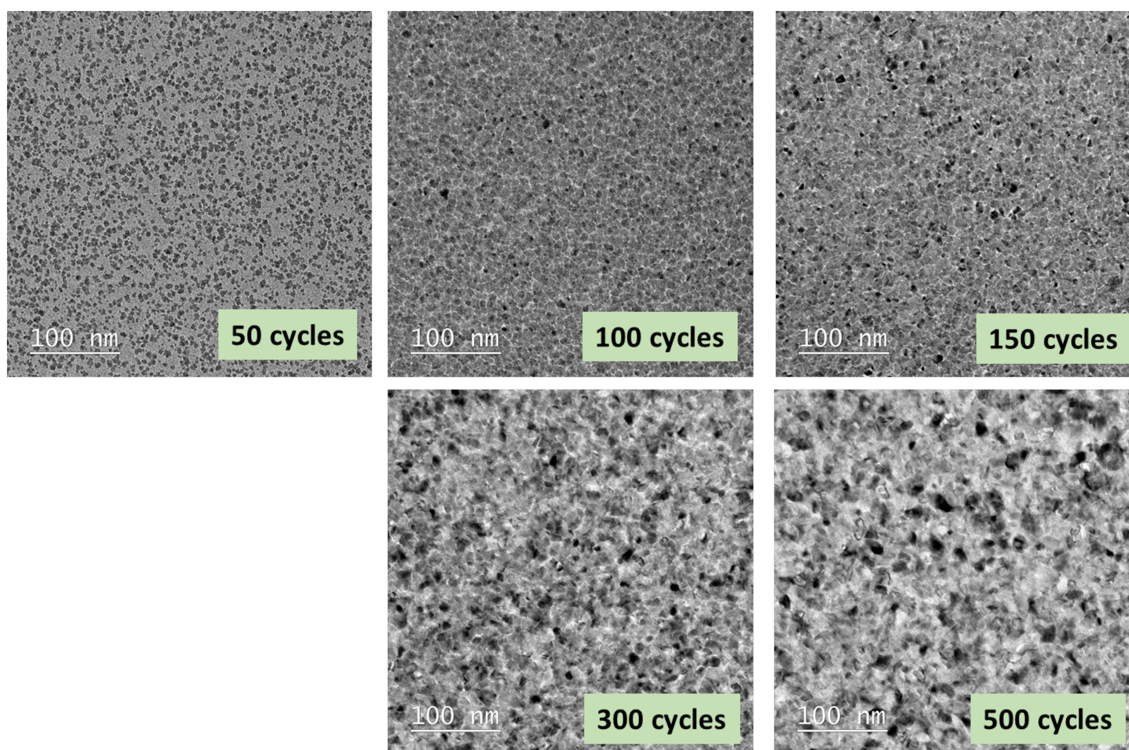

Figure 3.3.9: *Bright Field TEM of* $60\,s$ O_2 *dosing step* RuO_x *ALD. For the 50 ALD cycles sample the substrate is still visible in the lighter shade of grey, and numerous islands of* RuO_x *appear across the sample in the darker shade of grey.*

With every TEM image an electron diffraction pattern has been measured resting on the quantum mechanical principle that an electron can also be represented as a wave. In TEM one can also detect the diffracted electron beams from an atom present in the film instead of the transmitted electrons used for the TEM image. Spatially, the electron beams can have interference if diffraction occurs by regular spacing between atoms, thus creating an interference pattern. Polycrystalline structures have a ring pattern as is the case in these RuO_x films. The rings can be linked to different orientations [48] which are also indicated in figure 3.3.10.

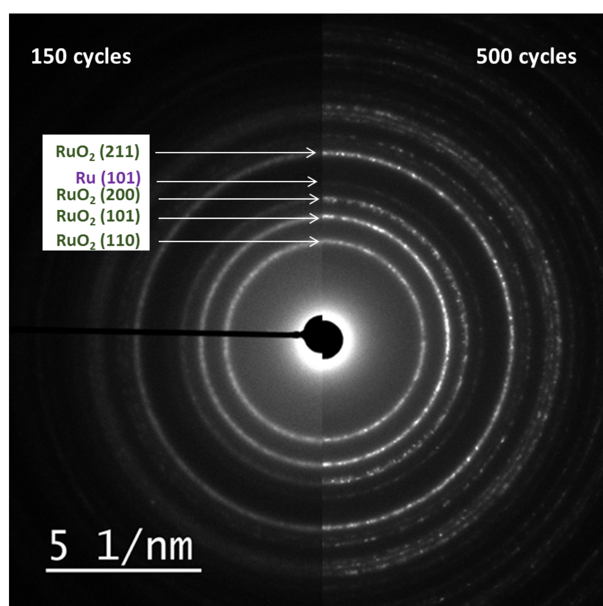

Figure 3.3.10: *Electron diffraction patterns of 150 cycles compared to 500 cycles of RuO_x ALD with a 60 s O_2 reactant step. The interference rings become brighter as the layer thickens. RuO_2 rings are the most apparent originating from crystalline RuO_2(110), RuO_2(101), RuO_2(200) and RuO_2(211). But also a weaker ruthenium metal ring is present from the Ru(101) orientation which could not be detected with the XRD measurement.*

The rings increase in intensity as the layer grows thicker which indicates there is more crystalline material to diffract from. The same orientations can be found as in the XRD diffractograms but also the metal Ru(101) is noticeable although it is very weak. Thus, even with a 60 *s* O_2 reactant step the film still contains a metal phase. It is believed that the growth starts with a Ru nucleation eventually growing a more oxide-like layer. In the appendix figure 5.0.3, XPS results show that the binding energy of the Ru-O bond goes more to a Ru-Ru bond as the layer is sputtered, which agrees with this expectation. Here, preferential sputtering of oxygen needs to be taken into account as a possible side effect thus this result does not provide concluding evidence. This initial metallic nuclei is reported by R. Methaapanon et al. [53] with *in-situ* XRD of ALD RuO_x growth on amorphous SiO_2.

3.3.3 Temperature influence

Up to this point only the set table temperature of $200°C$ has been used. Different deposition temperatures generally lead to different film properties so this has also been investigated. First, the standard recipe (figure 3.3.3) was used on different temperatures. Steps of $50°C$ were taken in the set temperature of the table so that the ALD process was performed on a $[100 - 400]°C$ interval. A temperature window in which deposition occurs was found from $150°C$ to $300°C$ and the GPC according to table temperature is shown in figure 3.3.11.

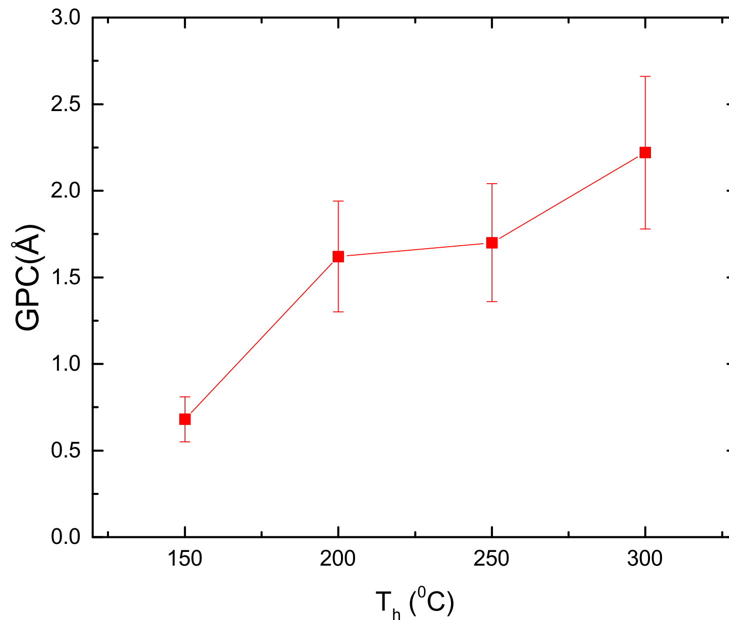

Figure 3.3.11: *Temperature window where the GPC is plotted against the table temperature. The standard RuO_x ALD recipe with 15 s precursor dosing and 40 s oxygen dosing was used.*

Below $150°C$ no deposition was found on the substrate after 150 cycles. This could be explained by the fact that the precursor is not reacting with the substrate because of the low thermal budget. However, it could also be that for lower temperatures there is a long nucleation delay which takes longer than 150 cycles. On a table set temperature of $150°C$ it has to be noted that the ALD process is hardly repeatable. For temperatures higher than $300°C$ there is likewise no deposition present on the substrates. This could be explained by the fact that the precursor decomposes entirely or is unstably bonded to the substrate.
These samples were further investigated with the use of XRD and RBS to characterize the temperature influence on the structural material properties. In figure 3.3.12 the XRD diffractograms are shown for the different set temperatures and in table 3.3.2 the RBS results are displayed.

RuO_2 related peaks and the Ru(101) metal peak can be observed in all the films. As the films have varying thickness it is clear that, with the standard recipe, the formation of the metal phase cannot be obstructed or prevented by changing the temperature.

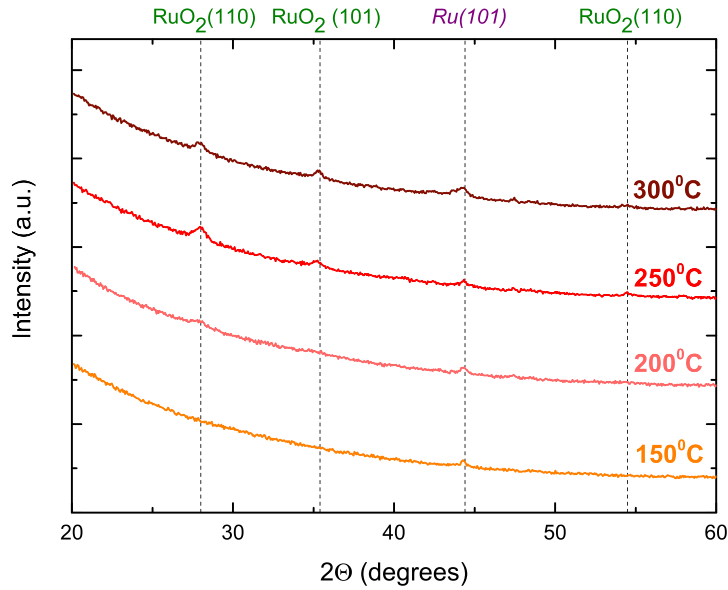

Figure 3.3.12: *XRD measurements on RuO_x films deposited with different set temperatures. The films were created with 150 cycles on Si substrates with a native oxide. The different film thicknesses can be found in table 3.3.2. A match for the crystalline orientations and the 2Θ positions are found in literature [48].*

Table 3.3.2: *Properties of the RuO_x films deposited with varying table temperatures. The layer thickness and GPC are determined by SE. The amount of deposited Ru [at. nm^{-2} $cycle^{-1}$] and the chemical composition were determined by RBS; the hydrogen content was determined by ERD. Carbon contamination in the bulk was below the RBS detection limit of 5 at% for all films. The accuracies for H, O and Ru are respectively 7%, 5% and 2%. Typical errors are indicated.*

Deposition temperature ($°C$)	Film thickness (nm)	GPC (Å)	O/Ru (-)	[H] ($at.\%$)	Deposition rate Ru ($\frac{at}{nm^2 \cdot cycle}$)	Mass density (g/cm^3)
150	8.2	0.68 ± 0.13	2.18 ± 0.10	29.2 ± 2.0	0.74 ± 0.01	3.1 ± 0.1
200	19.4	1.62 ± 0.32	1.98 ± 0.10	7.5 ± 0.5	3.53 ± 0.07	6.0 ± 0.3
250	20.4	1.70 ± 0.34	1.66 ± 0.07	4.6 ± 0.3	4.46 ± 0.08	6.9 ± 0.4
300	29.3	2.22 ± 0.44	1.04 ± 0.05	7.0 ± 0.5	5.44 ± 0.10	5.4 ± 0.3

Clearly, there are large differences between the $150°C$ sample and the other samples. The $150°C$ film is still an unclosed layer which explains why the deposition rate is so low and the hydrogen concentration is so high as hydroxyl groups (O-H) are present at the substrate's native oxide surface.

When looking at the other three films one notices a sharp decrease in O/Ru ratio as the temperature increases. The $250°C$ sample has a noticeably higher density, which is almost the same as the bulk density of $6.97\,g/cm^3$ [49], and a lower hydrogen concentration [H] which is expected with higher density. Furthermore, the deposition rate of Ru atoms increases with temperature as is in agreement with the increasing GPC. The $200°C$ setting, which was used in the previous section for the film characterization, is the best option to create the RuO_x with the desired properties.

Undeniable still is the island formation which causes the growth process to be less controllable as an ALD process needs to be highly uniform and conformal. Also, the metal phase is problematic for the application of this material as a possible passivating contact and it seems this cannot easily be avoided. Preliminary attempts have been made with a plasma-enhanced ALD recipe with the EBCHDRu precursor with O_2 plasma. This resulted in no film growth but products of the precursor, like Ru and carbon-hydrogen chains, were measured in the reaction chamber by a Quadrupole Mass Spectrometer (QMS). The hypothesis is that the deposited material is etched away faster by the plasma than it is deposited.

3.4 Optical and Electrical Properties of ALD RuO_x

There are still some other properties which are important if this material would be used in a solar cell device. The optical properties, more precisely the absorption coefficient and refractive index, are important to determine where it could be used in a solar cell. Furthermore, the conductivity of the material could limit the thickness if it were too low and the cell structure possibilities.
These properties are also investigated for the RuO_x films and the results are discussed next.

Optical Properties
The refractive index n and extinction coefficient k can be determined with the SE model. The problem with the data on the RuO_x films is that there seems to be no obvious physical model that can accurately describe the raw data except for the mathematical B-Spline model. This model specifies the optical constants versus wavelength using a series of control points which are equally spaced in photon energy $[eV]$ [51]. A downside is that this model is dependent on the settings one uses as starting values for n, k and the amount of control points one uses for the B-Spline to fit. This could significantly influence the outcome for the same kind of RuO_x films. The amount of fit points were chosen such that a low enough MSE (Mean Square Error) value was achieved, thus a proper fit was constructed, but not too many as it otherwise over-parametrizes the data. With the B-Spline model the optical constants have been determined for the deposited films and a typical result is shown in figure 3.4.1.

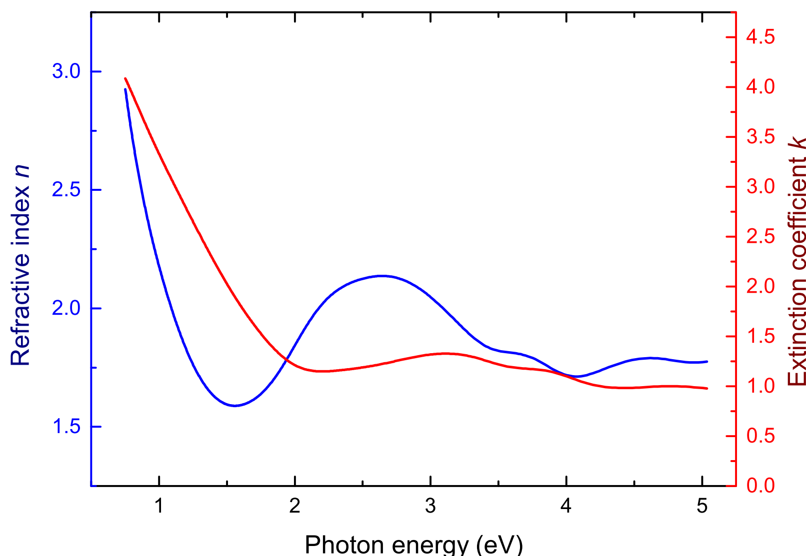

Figure 3.4.1: *Refractive index n and extinction coefficient k of a RuO_x film deposited on a Si wafer with native oxide with 150 cycles of the standard ALD recipe on $200°C$. The data was obtained with in-situ SE. Only a B-Spline model could be used to obtain the optical constants.*

The result is in good agreement with the experimentally determined n and k values of single crystalline rutile RuO_2 [52] which are shown in the appendix figure 5.0.2. From the extinction coefficient k one can see that the film is very absorbing. Normally a semiconductor has a bandgap such that basically no light is absorbed up until a certain band gap energy E_g. This would be around $2.2\,eV$ for RuO_2 as is known from literature, see section 4.1.1.. The band tail is noticeable around this energy but a large Drude absorption, which is caused by free charge carriers, prevents total transmission. In the Drude model for metals most electrons are free and not bound to nuclei which eventually leads to a high absorption coefficient in the lower frequency region. This large Drude contribution could be expected from the free charge carriers present in the $3d$ shell of RuO_2 but is probably also caused by the metal phase in the material deposited as seen in the film analysis in section 3.3.2.
One can calculate the absorption coefficient α from the extinction coefficient k by using:

$$\alpha = \frac{4\pi f k}{c} = \frac{4\pi k}{\lambda} \tag{3.4.1}$$

as the velocity of light in a vacuum is $c = \lambda f$ where λ is the wavelength of the light. Now the absorption coefficient can be plotted for different photon energies. In figure 3.4.2 one can see the α of the deposited RuO_x layers and other interesting hole-selective contacts for comparison; the solar spectrum irradiance in the AM1.5G is plotted as a reference.

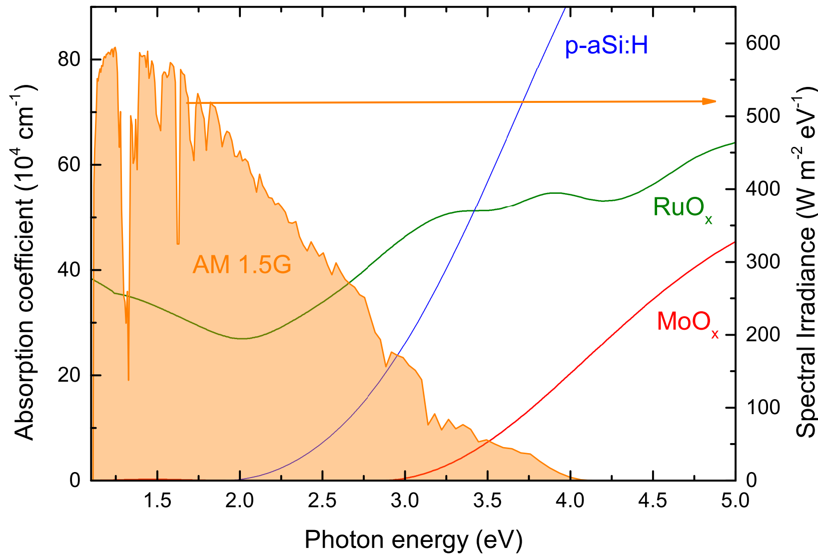

Figure 3.4.2: *Absorption coefficient α of RuO_x and other hole selective contacts MoO_x and p-type a-Si:H. The solar spectrum, $AM1.5G$, is shown for reference.*

These results show that the RuO_x films are not suitable for use on the front of a solar cell. The optical losses are much larger for RuO_x when compared to other hole-selective contact materials, such as p-type a-Si:H and MoO_x, which is due to the large free carrier density manifesting itself as a large absorption of the lower energy photons. However, RuO_x could still be used on the backside of a solar cell, as it does not contribute much to the optical losses there.

Electrical Properties

To characterize the electrical properties Four Point Probe (FPP) measurements and Hall measurements were performed. From the FPP one can determine the sheet resistance, and thus the resistivity when the thickness is known, and from the Hall measurements one could determine the carrier mobility and the majority carrier density. The films that were deposited with 150 cycles, as was noted from the TEM images in figures 3.3.8 and 3.3.9, had a long delay before the RuO_x films were closed which is also dependent on the deposition conditions. This can interfere with the electrical measurements as one is not always sure if the layer is fully closed or not which can explain all the outliers which are measured. The values for the sheet resistance R_s are used to determine the bulk resistivity ρ by the definition of $\rho = R_s \cdot d$ with d the layer thickness. All the measured sheet resistances are plotted in figure 3.4.3 against layer thickness and a $R_s = \frac{10\rho}{d}$ fit is used to determine the bulk resistivity which gives a result of $\rho = (417 \pm 31)\,\mu\Omega \cdot cm$. The residual of the fit is plotted in the inset of the graph, from this can be concluded that there is a big uncertainty in the measurements, especially for the thinner layers which is attributed to unclosed films.

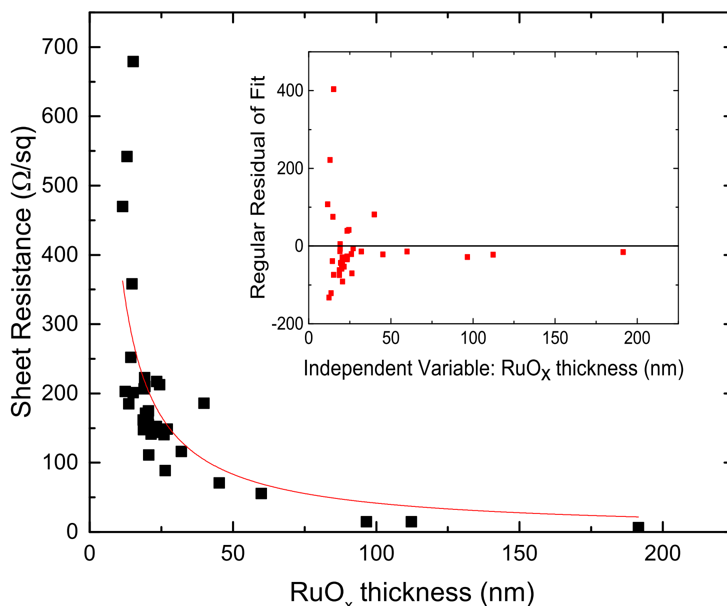

Figure 3.4.3: *The measured sheet resistance in Ω/sq is plotted against the RuO_x layer thickness. A fit through the results gives the bulk resistivity ρ. The residual of the fit is plotted in the inset of the graph which shows a large spread for the thinner layers.*

The results of the calculated bulk resistivity are shown in figure 3.4.4 and figure 3.4.5 in terms of precursor and O_2 dosing time.

The resistivity measurements have a wide spread and no big influence of the precursor dosing time is noticeable. The O_2 dosing time should increase the O/Ru ratio with longer dosing time. This would expect to lead to an increase in resistivity as the bulk resistivity of Ru, $7.4\,\mu\Omega \cdot cm$ [38], is lower than that of bulk RuO_2, $35.2\,\mu\Omega \cdot cm$ [38] and reported to be 60 to 300 $\mu\Omega \cdot cm$ with EBCHDRu ALD RuO_x by Park et al. [42].

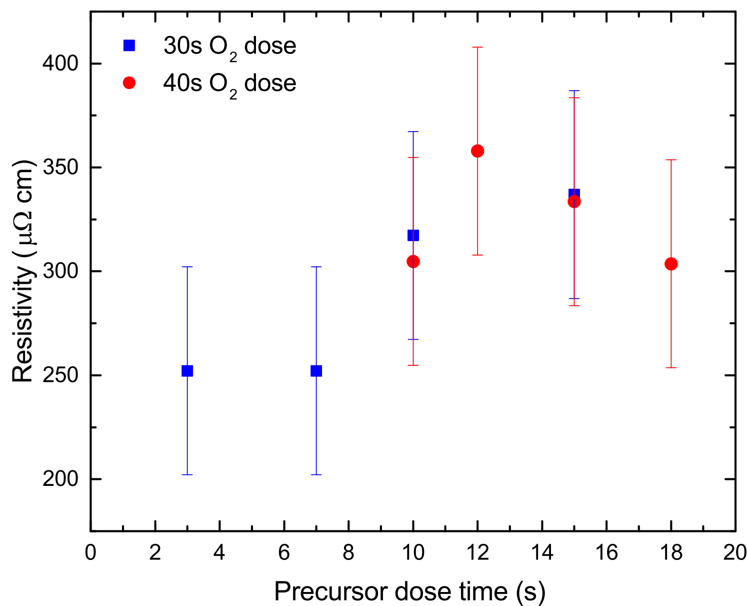

Figure 3.4.4: *Resistivity, given in $\mu\Omega \cdot cm$, determined from sheet resistance measurements for varying precursor dosing time. The O_2 dosing time is 30 s visualized in blue and 40 s visualized in red.*

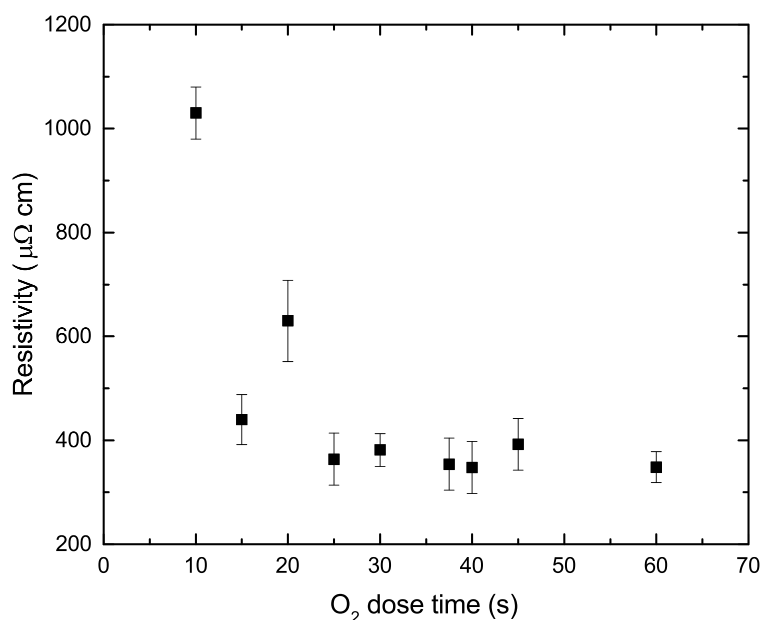

Figure 3.4.5: *Resistivity, given in $\mu\Omega \cdot cm$, determined from sheet resistance measurements for varying O_2 dosing time. The precursor dosing time is 15 s.*

However, this can not be concluded from the measurements.
The error is too big to define any influence and the outlier for lower dosing times is probably due to unclosed films. The averaged resistivity is $(338 \pm 43)\,\mu\Omega \cdot cm$ without including the biggest outliers which is higher than literature values. The bulk resistivity of the ALD RuO_x is expected to be lower as the thicker closed layers have a negative residual but can not be confirmed with the deposited samples.

Hall measurements were also performed but encountered the same issues. Very high bulk carrier concentrations in the order of 10^{21}-$10^{23}\,cm^{-3}$ are measured, which is more typical for metallic films than it is for semiconductors. The measured values for bulk charge carrier concentration were mostly negative which would indicate a n-type conductor, but sometimes positive values were measured as well. Furthermore, the carrier mobility in the films was too low to determine with the used set-up and is the probable cause for the measurements which gave faulty results like a positive carrier concentration.

3.5 Passivation Qualities

As discussed in chapter 2.1 one needs to reduce the recombination rate U_s but this quantity is experimentally not directly accessible. A different, and more directly accessible, quantity is the effective lifetime of the minority charge carriers τ_{eff} which is determined by the photoconductance decay curve of a sample. The lifetime is calculated from the carrier concentration decay over time [27]. A Silicon Wafer Lifetime Tester from Sinton Instruments is used to perform these measurements. With this technique lifetimes down to a couple of μs can be measured.

The Si wafers used for this are high quality n-type Float Zone (FZ) (100) wafers ($\rho = 1.0 - 5.0\,\Omega \cdot cm$) so that the bulk defect effects on the effective lifetime are minimized. The interface is now the cause for the biggest losses and this interface needs to be passivated. Different RuO_x layers are deposited on both sides of the FZ wafers to measure the influence of the RuO_x films on the minority carrier lifetime. FZ Si wafers are cleaned in a 1% HF solution to remove the native oxide. The cleaned Si wafers can undergo a Nitric Acid Oxidation Step (NAOS, HNO_3) treatment after the 1% HF cleaning to form a new, well defined, SiO_2 interlayer or an a-Si:H interlayer can be deposited by CVD. Consequently, samples with a Si/RuO_x, Si/SiO_2/RuO_x and a Si/a-Si:H/RuO_x interface, respectively, are created. Moreover, different ALD recipes are tested where thickness and oxidation time ($40\,s$ and $60\,s$) are varied. The samples are shown schematically in figure 3.5.1.

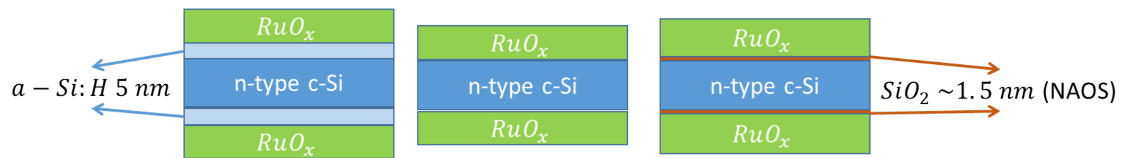

Figure 3.5.1: *Schematic representation of the lifetime samples used to qualify the passivation of the RuO_x films. The RuO_x films are deposited with 50 to 100 ALD cycles also varying oxidation time to $40\,s$ or $60\,s$. The FZ Si wafers undergo a 1% HF dip to remove the native oxide. Afterwards, different interlayers can be created; SiO_2 with a NAOS treatment or a-Si:H with CVD.*

The results of the Si/RuO_x and Si/SiO_2/RuO_x wafers show no passivation as the lifetime is around $3\,\mu s$ which corresponds to a bare unpassivated wafer. This can be due to multiple reasons like an unclosed film or recombination in a defective RuO_x layer itself. Moreover, the Ru metal phase in the film can potentially be formed at the interface. A metal is an efficient recombination site at the surface as it has no bandgap and there is no selectivity for either charge carrier. In this way, as explained in chapter 2.1, significant recombination losses will occur.
The only way a reasonable minority carrier lifetime of $\tau_{eff} = 1.8\,ms$ was obtained was with a $5\,nm$ thick a-Si:H interlayer and a $250°C$ forming gas anneal (FGA) which causes chemical passivation of the interface. The result is shown in figure 3.5.2. Now the function of the RuO_x is its selectivity which is also the case for the hole-selective MoO_x [46].

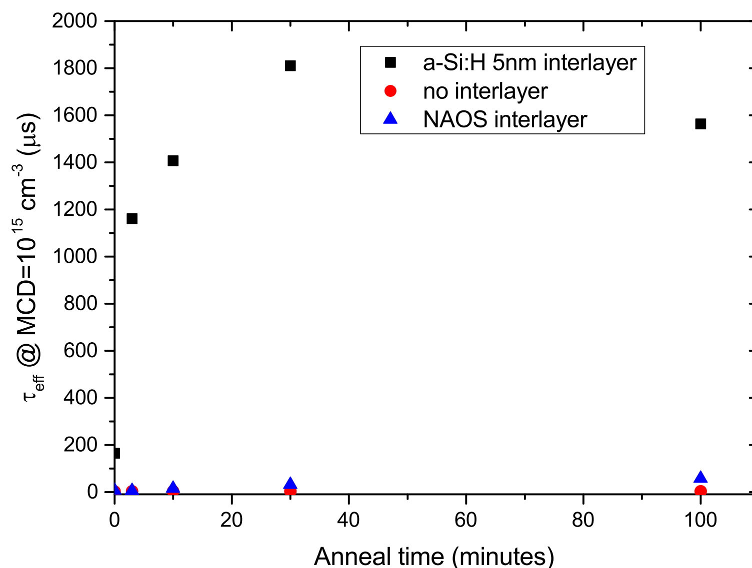

Figure 3.5.2: *Minority carrier lifetime measured with a lifetime tester determined at a minority carrier density of* $10^{15}\,cm^{-3}$*. Only decent passivation is measured with a* $5\,nm$ *thick a-Si:H interlayer after a* $250°C$ *FGA. The deposited* RuO_x *layers are* $\pm 10\,nm$ *thick for the results shown in this graph.*

3.6 Conclusion and Outlook

Conclusion

A thermal ALD process with O_2 reactant step is developed to deposit RuO_x films on Si/SiO_2 substrates using (ethylbenzene)(1,3-cyclohexadiene)Ru(0). Polycrystalline RuO_x films with a rough surface and metal fraction are deposited in a temperature window of $[150 - 300]°C$. The deposited materials are systematically studied in terms of structural, optical as well as electrical properties.

It is hard to control and reproduce the growth with a thermal recipe. The growth process is very complex since the material properties change throughout the thickness and the influence of changing the reactant step is still noticeable even in the saturation regime. The growth mode is Volmer-Weber mode where adsorbate-adsorbate interaction is stronger than the adsorbate-surface interactions, hence the island growth. This indicates that the EBCHDRu precursor reacts more with the RuO_x islands than with the Si/SiO_2 substrate. It may be that a surface pre-treatment would enhance a more conformal growth where the surface is functionalized for the Ru-precursor adsorption. Furthermore, the ALD process could be altered to get a more controlled growth with a plasma reactant step. This was briefly tried but no growth with the EBCHDRu precursor was observed, although it is known that PEALD of RuO_x is possible [38]. The hypothesis is that the deposited material during a cycle has a higher etch rate than deposition rate, especially in the nucleation regime.

The passivation quality does not need to come from the RuO_x itself but could be induced by interlayers like SiO_2 or a-Si:H. The results show that a $5\,nm$ thick a-Si:H interlayer can

provide enough passivation ($\tau_{eff} = 1.8\,ms$) for a RuO_x/a-Si:H/c-Si stack. Now the function of the RuO_x is its selectivity which is also the case for the hole-selective MoO_x [46]. But then the question remains if the RuO_x is even hole-selective and is its contact resistivity low enough.

Overall, the goal to prove that we can deposit RuO_x layers as a functioning hole-selective passivating contact has not been completed yet. The deposited films have a metallic fraction believed to be at the interface which probably makes it not passivating, non-selective and conductive for both types of charge carriers. Furthermore, the WF still needs to be determined of the deposited material so that it can be demonstrated as being hole-selective and the contact resistivity needs to be determined.

There are also different applications for Ru and RuO_x for which maybe a mixed phase material could be used. In the IC gate structures it could for example still be used as a diffusion barrier and electrode as the metal and oxide are both conductive and thermally and chemically stable.

Outlook

The deposited RuO_x films still show a metal phase which is preferentially absent for the application as passivating contact. The ALD process can potentially be altered to prevent the formation or remove this metal fraction from the film. Further investigation is needed to improve this process.

To get an idea of the hole-selectivity, the Work Function (WF) of the deposited material needs to be determined as this needs to be high enough to induce upwards band bending. A way to do this is with X-Ray Photoelectron Spectroscopy (XPS) where X-rays ($h\nu > 1000\,eV$) are used to emit electrons from the material. The kinetic energy of these electrons escaping the surface are measured, the lower energy bound where the electron emission spectrum has cut-off is the minimal energy required for this emission which corresponds to the WF. With lower energy photons ($h\nu < 50\,eV$) using ultraviolet (UPS) [54] only the valence levels can be ionized with such low energies, thus creating a thin excitation line. The experimental determination of the work function using XPS or UPS is not a straightforward task as the photons can influence the sample in different ways [55]. Moreover, the WF could be dependent on stoichiometry and, for thin films, the thickness which could be enhanced so that the WF is high enough.

Contact resistance samples are already in preparation. The RuO_x layers have a high conductivity so to define a better contact surface and prohibit lateral transport, the film needs to be etched away in between the Al contact dots. It is proposed to do this with an O_2/H_2 plasma treatment which is already experimented to etch away the deposited RuO_x films.

Chapter 4

Titanium Oxide

Abstract: Titanium oxide (TiO_x) potentially exhibits hole-blocking properties which can be used to make an electron-selective contact in silicon solar cells. It has been reported that it can also passivate the Si surface which is why this material could possibly be used as a passivating contact. As TiO_x is transparent due to its high bandgap and well known as ALD material, it might be a good candidate as a passivating contact in efficient SHJ solar cells to potentially simplify the production process of industrial SHJ cells.
It is concluded that amorphous TiO_x films deposited with a thermal ALD process give the best passivation on n-type Si wafers while plasma-enhanced ALD recipes possibly induce damage due to high energy UV-radiation which can only be repaired by annealing to some extent. Furthermore, the best passivation performance is achieved with the metal-organic precursor titanium isopropoxide (TTIP), which already passivates the c-Si surface in as-deposited state as opposed to the two other precursors used. After 15 minutes of FGA treatment on $300°C$ record carrier lifetime $\tau_{eff} \approx 2.0\,ms$, $iV_{oc} = 698\,mV$ and $J_0 = 12.3\,fA/cm^2$ with $\sim 5\,nm$ thick TiO_x films are achieved.
The minimal contact resistivity of an Al/TiO_x/c-Si stack is $\rho_c = 0.4\,\Omega \cdot cm^2$ which can, together with the low recombination current density, lead to maximum solar cell efficiencies of around $\eta = 26 - 27\%$ under the assumption that the front side of the cell does not induce any optical or electrical losses. This enables the formation of TiO_x as full area passivating contact which shows its industrial potential.
However, when using the ALD TiO_x films on cell level, the open-circuit voltage (suns-V_{oc}) values drop significantly opposed to the excellent implied open-circuit voltage (iV_{oc}) values of these cells. This was caused by a lack of selectivity in the cells which needs further investigation to establish the source of the problem.

4.1 Introduction

4.1.1 Background on Titanium Oxide in Solar Cell Applications

In the early days of photovoltaics TiO_2 was used as an anti-reflection coating (ARC) [56]. An ARC reduces the reflective losses due to different refractive indices between two layers. This implies that the ARC needs to have a selected refractive index between the values of the coupled mediums, while using a single coating so the reflectance at a specific wavelength can be diminished to a value near zero. The refractive index of TiO_2 is typically $n = 1.9 - 2.45$ which is near the geometric mean of the adjacent materials (Si and glass/air) diminishing reflective losses. Together with its low extinction coefficient $k < 0.1$ for $\lambda > 350\ nm$ made it an excellent candidate for an ARC on silicon solar cells.

Over time, it got replaced by SiN_x due to the superior passivation quality of SiN_x of the bulk and on the n^+ emitter [57]. However, with the growing interest in n-type wafers, which typically have a lower bulk defect density when compared to p-type wafers, passivation is needed on the p^+ emitter and this is where TiO_2 comes back into play. Cui et al. [58] show that TiO_2 exhibits passivation qualities both on p and p^+ and on n and n^+ Si surfaces, but it is superior on the p^+ over n^+ diffused regions, which makes the potential on n-type Si clearly bigger.

Also, on a side note, TiO_2 is used in perovskite solar cells as a mesoporous charge conductor on which the active absorber layer, the perovskite, is coated. TiO_2 is the most commonly used electron transport layer in this device which should yield a suitable work function, low surface recombination rate, and high conductivity and has achieved the best perovskite solar cell device performance up to date [59].

4.1.2 Titanium Oxide as Passivating Contact

TiO_2 as a passivating contact has drawn a lot of attention since it has been introduced as a passivating ARC as mentioned in the previous section.
TiO_2 is transparent with a bandgap of $E_g \approx 3.35\,eV$ [68] and is able to form an electron-selective contact with c-Si due to its band alignment to the conduction band of the c-Si (a small offset of typically $\Delta E_C \approx\ 0.05 - 0.1\ eV$) and a large valence band offset with respect to the c-Si valence band [60]; this is shown in Figure 4.1.1.

Recently, several reports have appeared on the passivating and carrier-selective qualities of TiO_2 on solar cell level. In 2013, Avasthi et al. [60] showed the hole-blocking properties of TiO_2. Here the current was measured through p-type Si with an Al contact with and without an interlayer of $3\,nm$ of TiO_2. For p-type Si and Al normally a linear IV curve can be extracted, i.e. not blocking for holes. However, with the TiO_2 interlayer no current could be measured for small positive bias values ($< 0.5V$). The contacts were made in the mm scale so the TiO_2 films also seem pin-hole free to at least this macroscopical scale.

More recently, different publications showed an increasing trend in passivating qualities of TiO_2 layers and cell designs were tested. In 2014, Yu et al. [61] made their best performing passivating $8\,nm$ thick TiO_2 layer, which yielded $\sim 300\,\mu s$. Their layers were relatively thick

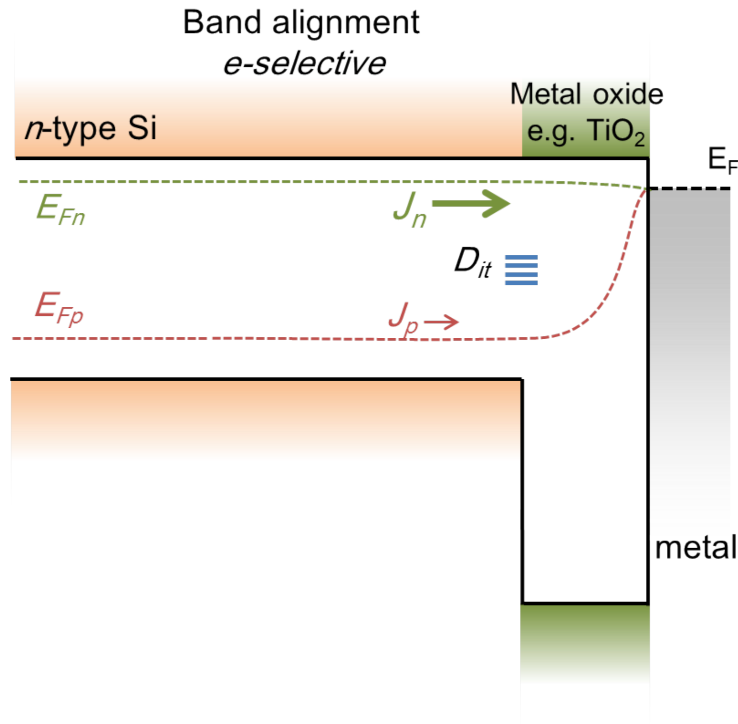

Figure 4.1.1: *Schematic band diagram of TiO_2 as electron selective contact ($J_n >> J_p$) on c-Si. The selectivity is realized through band alignment of the conduction bands, the hole current J_p is greatly reduced by the large valence band offset. The band diagram is illustrated under the situation of illumination which induces the quasi-Fermi levels. [10]*

as they went up to $66\,nm$. By Liao et al. [62] excellent passivation qualities have been obtained on p and n-type Si with the $TiCl_4$ precursor. Post-deposition treatments were used to increase the passivation quality: after annealing the lifetime went up to $\sim 1.5\,ms$ and after a light-soaking treatment even up to $\sim 4\,ms$. They also showed that the quality drastically decreased when crystalline (anatase) TiO_x was deposited at $300°C$.

In 2016, Cui et al., Gad et al. and Yang et al. [58,63–65] showed improved passivation results and concept cells with solar cell conversion efficiencies exceeding 20%. The films differ in optimum thickness, precursor usage and deposition temperature. However, the overall trend is that a couple of nm would already suffice to achieve good passivation and the thickness has a noticeable influence on the quality. Furthermore, as the TiO_x films start to crystallize, for deposition temperatures $\geq 300°C$, the passivation quality drops significantly. The best performance of a n-type FZ Si ($d = 190\,\mu m, \rho = 1.0\,\Omega \cdot cm$) lifetime sample [63] yielded an $iV_{oc} = 703\,mV$ and $\tau_{eff} = 865\,\mu s$.
A fully contacted back side cell with $4.5\,nm$ of ALD TiO_x as electron-selective contact, tested by Yang et al. [64], led to a champion cell with an efficiency of $\eta = 21.6\%$.
This shows the promising qualities of the relatively cheap and thin layered TiO_2 films in a relatively simple cell structure, which could lead to very cost efficient and high performance c-Si solar cells.

From these publications one can also derive that ALD is important as a deposition technique. The performance is highly affected by nm scale differences in thickness and the phase

and structure of the TiO_2, which are controllable aspects with ALD. The literature mostly focusses on an optimization of the TiO_x thickness and achieving a high cell efficiency. This work focusses on a material study and the differences in Ti-precursor while varying ALD processes, temperature, thickness and post-deposition annealing treatments.
In the next section the experimental details for the investigation of the TiO_x films as electron-selective passivating contact are explained.

4.2 Experimental Details

The ALD TiO_x films were deposited with an Oxford Instruments FlexAl ALD System. Spectroscopic ellipsometry is used to determine the layer thickness and optical characteristics of the TiO_x. A Tauc-Lorentz model is applied which makes use of the Lorentz oscillator and the Tauc joint density of states. It assumes a fully transparent material for photons with a lower energy than the bandgap energy which can be extracted from the fit.

Passivation:
After deposition, the passivation qualities can possibly be improved with a post-deposition annealing treatment. The optimum settings for this treatment were investigated with a Jipelec Rapid Thermal Annealler (RTA). The used annealing treatment is a Forming Gas Anneal (FGA) at a ratio of N_2:H_2=9:1. Anneal treatments provide a thermal budget for processes like hydrogen diffusion or structural reorganization which depend on the temperature and time of the treatment. For the passivation tests a treatment is mostly chosen just above the deposition temperature to prevent any damage due to a too high thermal budget, but also faster high temperature anneal treatments are investigated.

Carrier lifetime measurements were performed with the Sinton Silicon Wafer Lifetime Tester to determine τ_{eff}, J_0 and iV_{oc} of lifetime samples with the ALD TiO_x. For the comparison in passivation quality τ_{eff} is reported which is directly measured from the excess carrier density induced by a light flash which causes a change in photoconductance. This is why the lifetime is used as comparison instead of J_0 as the τ_{eff} is directly measurable. J_0, which is the important parameter for qualifying a passivating contact, is determined from a linear fit to the inverse lifetime (τ_{eff}^{-1}) and reported for the best passivating TiO_x films. The iV_{oc} is also measured directly from the excess carrier density as shown in equation 2.3.1.

The lifetime samples were made with 280 μm thick n-type FZ (100) Si ($\rho = 1.0 - 5.0\,\Omega \cdot cm$) on which the TiO_x films were deposited with varying ALD recipes. Furthermore, a bare Si wafer can be dipped in a nitric acid (HNO_3) bath for 10 minutes before TiO_x deposition to form a 1-2 nm thin SiO_2 layer. This SiO_2 interlayer could improve the overall passivation qualities as it provides chemical passivation of the c-Si surface. Moreover, an optional AlO_x capping layer could be used to potentially increase the passivation quality as hydrogen in the AlO_x layer could diffuse to the Si interface in the post-deposition anneal treatment. A schematic of the lifetime samples with optional interlayer and capping layer is given in figure 4.2.1.

The actual V_{oc} could be measured directly with a standard IV tester with a lamp spectrum approximating the spectrum of AM1.5G. The spectrum commonly used for solar research make use of air mass (AM) 1.5 as the solar zenith angle is inclined $\approx 48.2°$. However, suns-

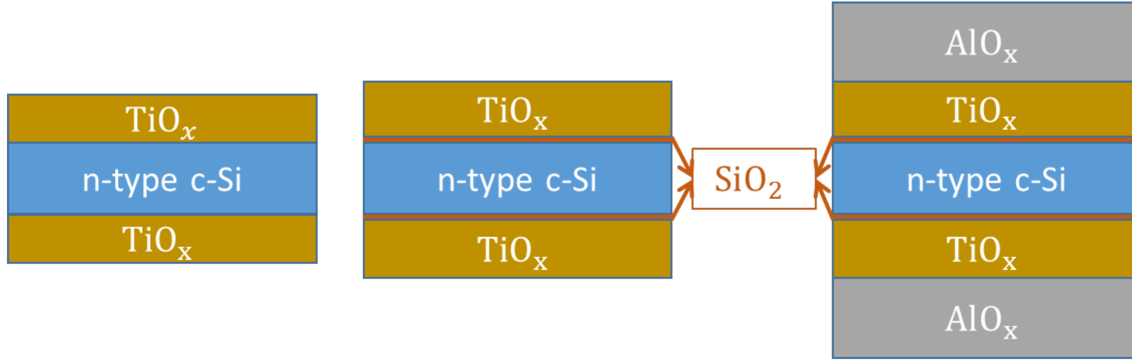

Figure 4.2.1: *Schematic representation of the lifetime samples used to qualify the passivation of the TiO_x films. n-type FZ c-Si (100) wafers of 280 μm thick with $\rho = 1.0 - 5.0\,\Omega \cdot cm$ are used as bulk material. An optional SiO_2 interlayer could be introduced like is shown in the middle. An AlO_x capping layer could be deposited on the sample like is shown on the right.*

V_{oc} measurements [26] were performed on half-cell devices with the deposited TiO_x films. Here, only the V_{oc} is directly measured in open-circuit condition as function of light intensity, typically from a few suns to below 0.1 suns, and no current is measured. The suns-V_{oc} at 1 sun intensity should coincide with that of the actual V_{oc} of the cell if the spectrum of the lamp is similar and the cell is at the same temperature.

Contact resisitivity:
The contact resistivity with c-Si (ρ_c) also needs to be determined as this gives an indication of the majority carrier conductivity. Here the Cox-Strack method [67] is applied to determine the contact resistivity of the Al/TiO_x/Si stack, where Al is the metal contact and n-type Si is used as bulk. This is exactly the relevant contact resistivity parameter as the current runs through this stack as the solar cell is operational.

Traditional transmission line measurements (TLM) can determine the contact resistivity of a semiconductor to the metal contact. One measures the lateral current path through the semiconductor which is not the relevant direction for a full contact area solar cell. The fact that the TiO_x film is not conductive enough and the current path with the Cox-Strack method is more representative for a cell, made this method preferred for determining ρ_c. A schematic representation of the Cox-Strack resistance measurement sample is given in figure 4.2.2.

Several contributions play a role in the resistance one measures in this way. The total resistance R_t measured consists of the contact resistance R_c, a spreading term R_s and a residual term R_0. The residual resistance is due to the substrate or contact resistance on the back side. This term is made as low as possible with high quality Si wafers and an Ohmic back side. The contact resistance, to a first order approximation, is given by $R_c = \frac{\rho_c}{\pi(d/2)^2}$. The spreading term of a circular disk, where the contribution of the Si wafer is dominant, is given by $R_s = B\frac{\rho}{2d}$. Here B is a correction factor experimentally determined to be $B = \frac{2}{\pi}arctan(\frac{4}{d/t})$. The other terms are given by the diameter of the contact d, the thickness of the film t and its resistivity ρ. As the biggest contribution to the spreading is the Si wafer itself, as the TiO_x films are just a couple of nm thick, the values of the Si wafer are given to

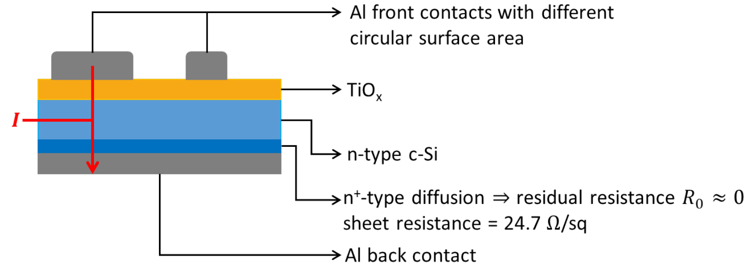

Figure 4.2.2: *Schematic of a contact resistance measurement sample; note that the different layers or not drawn to scale. The current is measured transversely through the stack of TiO_x and n-type c-Si as it would in an operating cell. The n^+ diffusion on the back side, with a corresponding sheet resistance of $24.7\,\Omega/sq$, is essential to create an Ohmic contact between the Si and the full Al back contact where the resistance is low.*

t and ρ as approximation. This leads to a total measured resistance of:

$$R_t = \frac{\rho}{d\pi} arctan(\frac{4}{d/t}) + \frac{4\rho_c}{d^2\pi} + R_0. \tag{4.2.1}$$

The total measured resistance is plotted against the inverse if the contact diameter $(1/d)$ where R_0 is the offset on the y-axis. In this way, the contact resistivity ρ_c could be determined knowing t and ρ of the Si wafer. Contact diameters of 0.5 up to $10\,mm$ were used as was done by Yang et al. [63]. Contacts with a diameter of 0.1 to $0.4\,mm$ were added to acquire a better representation of equation 4.2.1 by the measurement data.

Precursors:
Several metal-organic precursors were used for deposition to discover optimum quality thin TiO_x films as passivating contacts. These precursors are $Ti(Cp^{Me})(NMe_2)_3$, tetrakis (dimethylamino) titanium ($C_8H_{24}N_4Ti$, TDMAT) and titanium isopropoxide ($C_{12}H_{28}O_4Ti$, TTIP) and different thermal and plasma-enhanced ALD processes were used. $Ti(Cp^{Me})(NMe_2)_3$ is an experimental precursor which was used for PEALD in a [100-350]$°C$ temperature window and with high GPC by Sarkar et al. [66]. With this TiO_x ALD process preliminary studies are performed. TDMAT and TTIP are already industrial metal-organic Ti-precursors for which the passivation qualities are investigated. First off, the most promising results are shown with the TTIP precursor using a thermal ALD recipe.

4.3 Results

4.3.1 TTIP ALD TiO_x Results

The TiO_x films deposited with the TTIP precursor already show good passivating qualities in the as-deposited state, $\tau_{eff} \approx 900\,\mu s$ being the best performance as-deposited, and led to the best performance for which is why these films are extensively investigated.
A thermal recipe with H_2O as reactant at $T_h = 200°C$ with a GPC of 0.15Å is used to deposit the TiO_x layers. ALD on $T_h = 80°C$ did not yield any growth and no other temperatures are tested. The recipe consisted of a $2\,s$ precursor dose step and a $250\,ms$ H_2O dose step with $4\,s$ reaction time in the chamber before purging.

In figure 4.3.1 the deposited TiO_x film with the thermal TTIP recipe is imaged with cross-sectional TEM. The TiO_x is deposited on a FZ wafer which was cleaned for 1 minute in a 1% HF solution to remove the native oxide. After the TiO_x deposition, a thick AlO_x capping layer was deposited onto the TiO_x film with ALD to enhance the contrast.

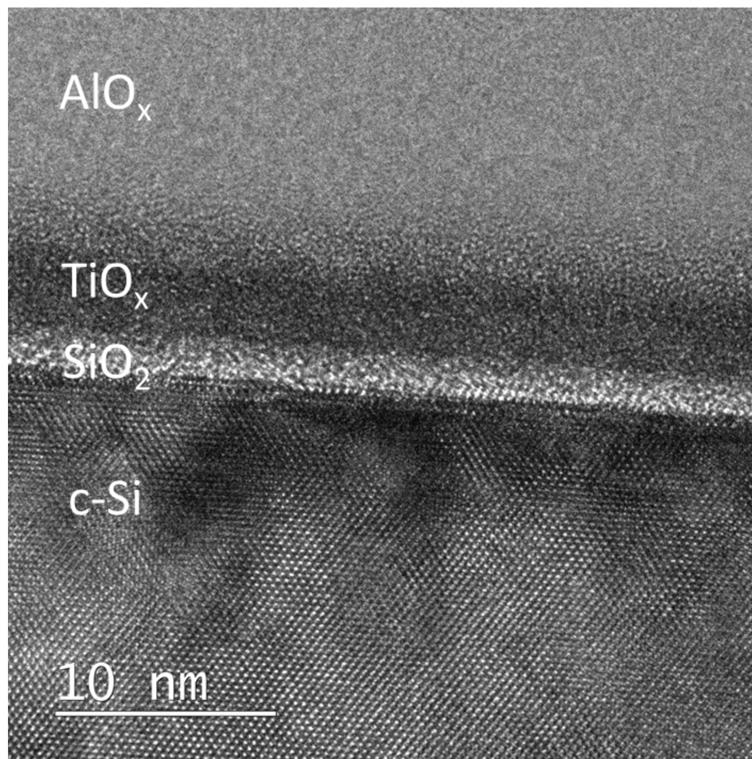

Figure 4.3.1: *TEM image of a $5\,nm$ TiO_x film deposited on HF cleaned FZ Si with the thermal TTIP ALD recipe at $200°C$.*

An amorphous TiO_x film can be seen in figure 4.3.1 with the desired thickness of $5\,nm$. One can observe that the thermal recipe grows a SiO_2 interlayer as the TiO_x film is deposited which can also contribute to the passivation quality.

Passivation results

Lifetime samples are created on high quality n-type FZ wafers ($d = 280\,\mu m$ and $\rho = 1.0 - 5.0\,\Omega \cdot cm$). Here the TTIP ALD recipe is used to deposit the films on HF cleaned substrates to get rid of the native oxide. Samples which had a NAOS treatment and those who had a bare c-Si surface are compared. From the iV_{oc} measurements the minority carrier lifetime τ_{eff} is determined for wafers with TiO_x layers deposited with TTIP. In figure 4.3.2 the passivation quality of the bare FZ Si, which has a SiO_2 interlayer created during the TTIP ALD process, and the FZ Si which has a NAOS created SiO_2 interlayer are compared for different FGA times at $300°C$ and different TiO_x layer thicknesses.

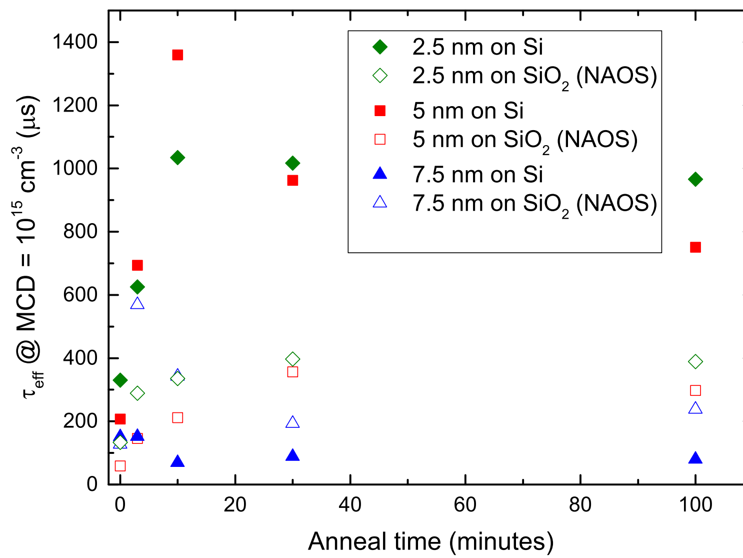

Figure 4.3.2: *Minority carrier lifetime measured with a lifetime tester determined at a minority carrier density (MCD) of* $1 \cdot 10^{15}\,cm^{-3}$. *Different* TiO_x *thicknesses are investigated for increasing FGA* (N_2:H_2=9:1) *time at* $300°C$. *The quality of the* SiO_2 *is important for the passivation quality; the* SiO_2 *interlayer, which forms during the ALD process, results in a better lifetime than the NAOS grown* SiO_2.

For the thermal TTIP TiO_x films there seems to be a dependence on anneal time and thickness for the optimum passivation quality determined by τ_{eff}. The thicker layers of $7.5\,nm$ perform significantly worse. Furthermore, the difference in quality of the SiO_2 interlayer is apparent from these results. The SiO_2 interlayer grown during the ALD process, performs better than the NAOS created interlayer. It is possible that with the elevated temperatures during the ALD process it grows a more dense SiO_2 film with less defect states. A NAOS induced interlayer normally needs to be activated after deposition with an annealing step ($\approx 450°C$) which could cause hydrogenation. In literature [73, 74] it is also reported that thermally grown SiO_2 has a better passivation quality than wet-chemical grown SiO_2 and the difference is attributed to a lower interface defect state density. The oxidation of the c-Si wafer happens during the ALD process itself and does not require any additional processing step.

Thin layers of just a few nm perform the best as passivating layer. The thicker layers are more likely to crystallize in the post-deposition anneal step as is shown with Raman spectroscopy, depicted in figure 4.3.3. This is detrimental for the passivation quality of TiO_x, as was also shown in other studies [62, 68]. The other signal peaks present in the spectrum belong to the c-Si wafer.

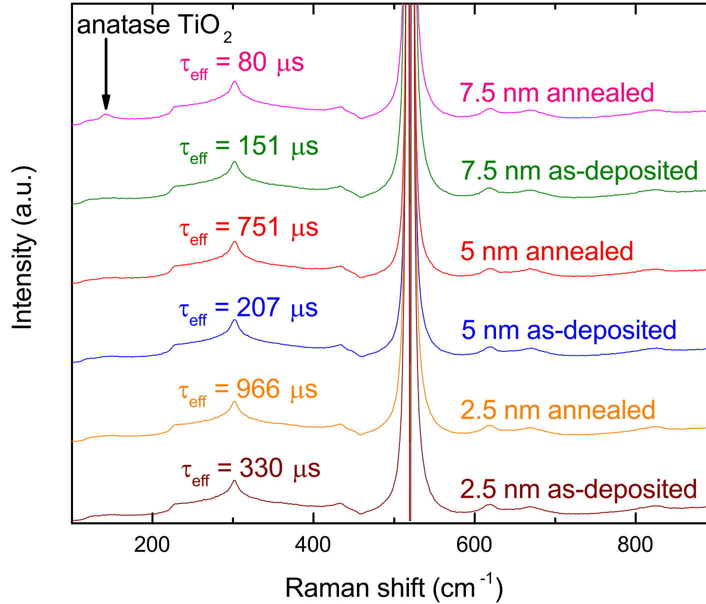

Figure 4.3.3: *Raman spectra of TiO_x films deposited with the TTIP ALD recipe. As-deposited and* 100 *minutes* $300°C$ *annealed layers are shown for* $2.5\,nm$, $5\,nm$ *and* $7.5\,nm$ *of* TiO_x*. The annealing can crystallize the film which does occur faster for thicker layers of* TiO_x*. This is shown by the anatase phase which is visible in the spectrum for the* $7.5\,nm$ *annealed film. The lifetime decreases significantly when crystallization occurs; the respective values are indicated in the graph.*

The dependence of the lifetime on the anneal time and thickness is closer investigated as the influence seemed significant in the first few minutes of the anneal treatment which was seen in figure 4.3.2. In figure 4.3.4 different TiO_x thicknesses from 2 to $6.5\,nm$ are investigated as part of a more precise FGA at $300°C$. For the best samples the minority carrier lifetime was so long that the light flash was set too short to measure at the lower injection level of $10^{15}\,cm^{-3}$. For this reason the results are extrapolated to this value and reported as such.

The best iV_{oc} is $698\,mV$ and the champion J_0 is $12.3\,fA/cm^2$ which were measured after 15 minutes of FGA at $300°C$ on $5.2\,nm$ thick TiO_x. The related lifetime was $\tau_{eff} \approx 2.0\,ms$. With all the TiO_x thicknesses a high lifetime has been obtained. Just $2\,nm$ needs a longer anneal treatment. The thicker $6.5\,nm$ shows an overall lesser quality in passivation which could be explained that it has started to crystallize as is more likely to happen with thicker layers. Although, Raman spectroscopy does not show a crystalline phase yet for the $6.5\,nm$ thick TiO_x after annealing. The corresponding iV_{oc} and J_0 values are plotted in the appendix figure 5.0.7 for the same TiO_x films as in figure 4.3.4.

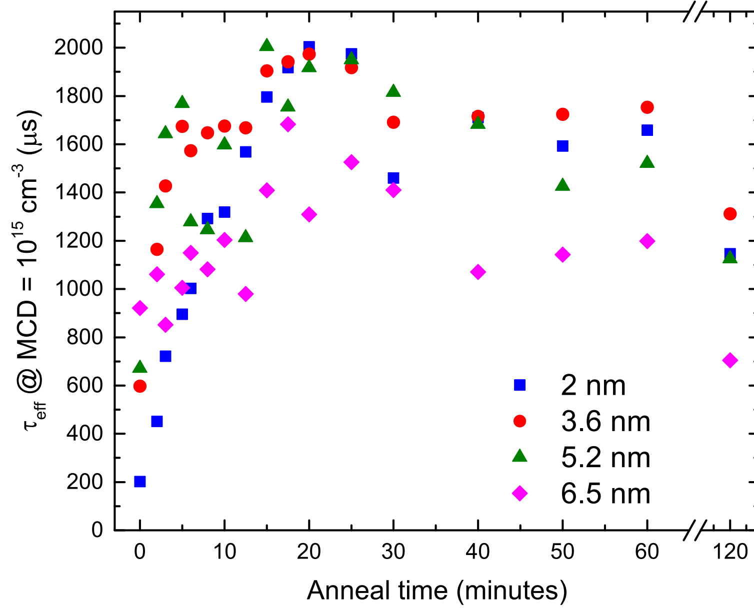

Figure 4.3.4: *Minority carrier lifetime measured with a lifetime tester determined at a minority carrier density (MCD) of* $10^{15}\,cm^{-3}$ *and for the better samples extrapolated to a MCD=*$10^{15}\,cm^{-3}$*. Different* TiO_x *thickness were investigated for increasing FGA (*N_2*:*H_2*=9:1) time at* $300°C$*.*

The lifetime results, also determined at a MCD = $10^{15}\,cm^{-3}$, of the TiO_x layers with an AlO_x capping layer are shown in appendix figure 5.0.8. This AlO_x capping layer is not necessary for the already excellent passivating TiO_x films. The results of the capped samples, even after annealing, are inferior to the uncapped TiO_x films.

The passivation quality of these samples, indicated by the effective lifetime, is superior to the literature values reported to our knowledge of TiO_x passivation of a c-Si surface with only a post-deposition anneal treatment. However, Yang et al. [63] achieved a slightly higher iV_{oc} ($\Delta iV_{oc} = 5\,mV$), which is ascribed to a thinner and better bulk quality c-Si wafer ($d = 190\,\mu m$ and $\rho = 1\,\Omega \cdot cm$). The passivation of the TTIP ALD TiO_x films of c-Si eventually lead to low J_0 values with a determined minimum of $12.3\,fA/cm^2$. Now the contact resistivity ρ_c is determined to show the potential of TiO_x as a passivating contact.

Contact resistivity results

The contact resistivity of an Al/ALD TiO_x/c-Si stack has been determined by the Cox-Strack method as presented in section 4.2. A voltage sweep was performed and the current was measured, thus the total resistance can be determined. The contact dot diameter from the shadow mask ranges from $10\,mm$ down to $100\,\mu m$. The contact dot sizes are remeasured with an optical microscope to determine the actual diameter as shadowing effects from the Al evaporation process occur which is especially significant for the smaller contacts. There is an Ohmic characteristic in the IV measurement until the compliance of the setup is reached which was maximal $\pm 400\,mV$ and could not be set to a higher value. Note that the resistance at the typical solar cell operating voltage of around $650 - 700\,mV$ could not be measured due to this compliance. The total resistance is plotted against the inverse contact diameter so that equation 4.2.1 can be fitted with the Si bulk resistivity set to $\rho = 3\,\Omega \cdot cm$ and the wafer thickness to $t = 280\mu m$. This way ρ_c can be determined as explained in section 4.2. An example of a model Cox-Strack fit is shown in figure 4.3.5.

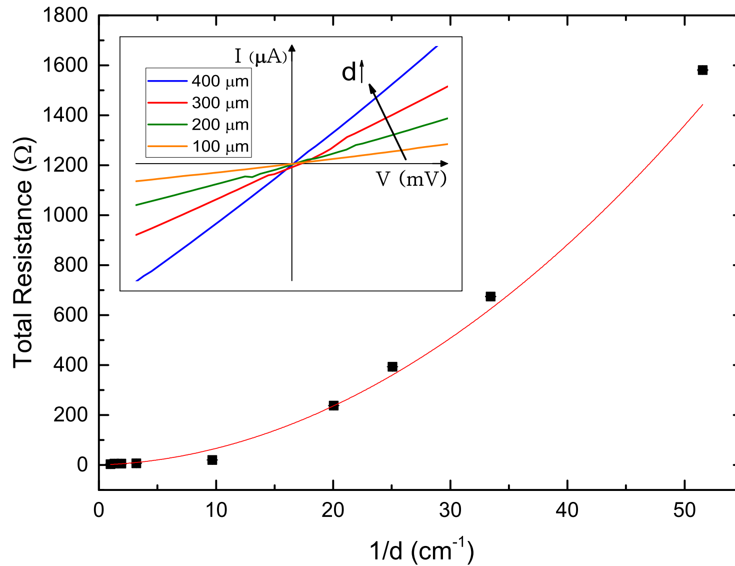

Figure 4.3.5: *The total measured resistance is plotted against the inverse contact diameter. This measurement is performed on a sample with $5.5\,nm$ of TiO_x. All IV-measurements are performed at least 3 times on different spots on the contact. The results are averaged which gives a certain error but is mostly smaller than the data marker. The contact diameters measured with a microscope are used and the error in this value is also smaller than the data marker. In the inset four IV-measurements on different contacts are shown from which the total resistance is determined. The smallest $100\,\mu m$ contact dot did not have a well-defined surface area as was determined with a microscope, so it is not included in the fit. The fit through the data points is given by equation 4.2.1. Here the Si bulk resistivity is set to $\rho = 3\,\Omega \cdot cm$ and the wafer thickness $t = 280\mu m$.*

The contact resistivity plotted against layer thickness of TiO_x in the as-deposited and annealed state is shown in figure 4.3.6. The lowest achieved contact resistivity is $\rho_c = 0.4\,\Omega{\cdot}cm^2$. No clear influence of the anneal step on the contact resistivity is noticeable. Only the increase for the $7\,nm$ thick TiO_x film after anneal is distinct which could be attributed to the formation of an anatase phase in the material. The annealed $4\,nm$ thick TiO_x sample was

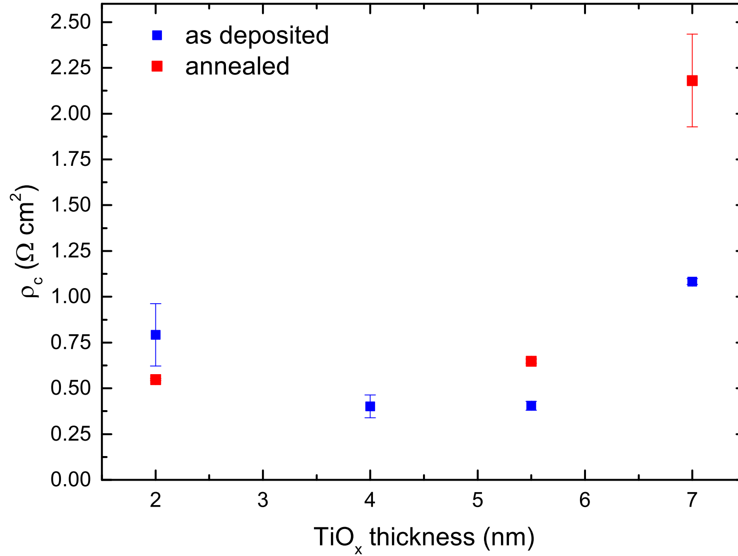

Figure 4.3.6: *The calculated contact resistivity is plotted against the TiO_x film thickness in as-deposited and annealed state. The lowest achieved contact resistivity is $\rho_c = 0.4\,\Omega \cdot cm^2$. The annealed 4 nm thick TiO_x sample was an outlier and is not included in the results. The error is the given by the fit of formula 4.2.1.*

an outlier and is not included in the results.

Yang et al. [64] also determined the contact resistivity with the Cox-Strack method. They showed that ρ_c decreases an order of magnitude, to a minimum of $0.02\,\Omega \cdot cm^2$, after a FGA treatment of $250°C$ of 3 minutes of Si/TiO_x/Al and Si/SiO_2/TiO_x/Al stacks. These stacks were initially, before annealing, the same order of magnitude as the results shown in figure 4.3.6. They attributed the decrease of ρ_c after annealing to a higher oxygen vacancy density in the TiO_x. An Al-rich AlO_x interface formed between the TiO_x and Al contact after annealing from which the oxygen came from the TiO_x layer. TiO_x shows a higher conductivity as oxygen vacancies increase which is the case after their FGA treatment shown with TEM. This effect could possibly be explained by the different (halide) Ti-precursor, $TiCl_4$, used for the ALD process of the TiO_x films by Yang et al. which could show different properties.

With the champion ρ_c and J_0 determined for the TTIP ALD TiO_x films an upper bound efficiency can be located in figure 2.3.1 for a full TiO_x back contacted cell. This point is indicated in figure 4.3.7 with a star symbol. If J_0 and ρ_c are the only limiting factors it could theoretically lead to a solar cell efficiency between $\eta = 26 - 27\%$, if there is no loss at all on the front side of the solar cell. The passivation quality is superior to the references indicated and when ρ_c is low enough it does not contribute significantly to the maximum obtainable efficiency as the iso-efficiency lines are almost vertical below $0.4\,\Omega \cdot cm^2$. The TiO_x deposited by TTIP ALD potentially have a low enough ρ_c but this could still be improved.

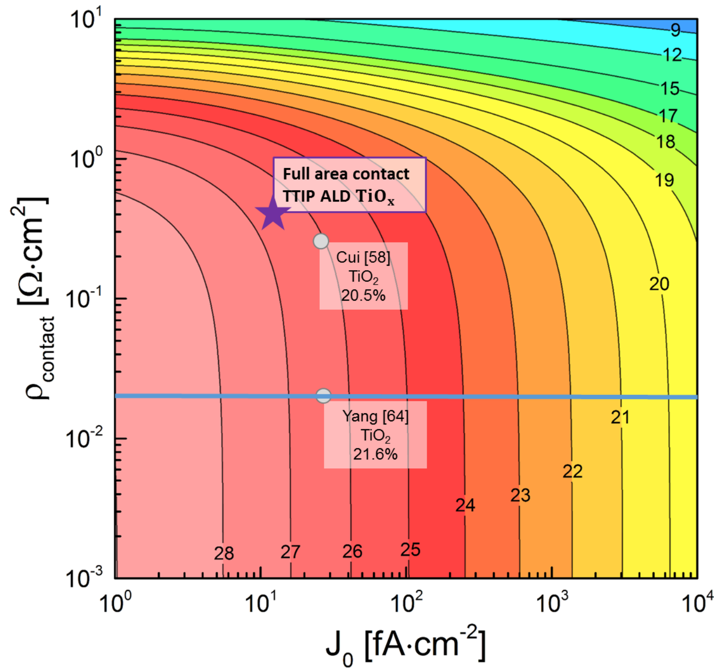

Figure 4.3.7: *Properties of the TTIP ALD TiO_x passivating electron-selective contact indicating the maximum obtainable efficiency if used in a c-Si solar cell [11]. Full area TiO_x contacts by Cui et al. [58] and Yang et al. [64] are given as reference with achieved cell efficiencies. Yang et al. did not report the J_0 values but the point indicated is the estimated value for they work at the same group at the Australian National University (ANU) as Cui et al. with the same passivation results of a lifetime value of 800 μs.*

4.3.2 Solar Cell Concepts with Titanium Oxide

Now the TiO_x films are optimized for passivation quality, they are implemented on solar cell half fabricates. Two different kind of cells were used: the bifacial n-Pasha cell and a SHJ cell with an intrinsic (i) a-Si:H layer, both are received from ECN (Energieonderzoek Centrum Nederland). The two structures are shown in figure 4.3.8. The n-Pasha c-Si solar cell had a bulk resistivity of $5\,\Omega \cdot cm$ and there were 3 types of SHJ solar cells which had varying bulk resistivities of 2, 5 and $5.5\,\Omega \cdot cm$. Furthermore, the provided n-Pasha cells had a distinction in processing steps. Cell G1S1 had the SiN_x layer deposited in two steps, G1S2 had its SiN_x deposited in one step and G2 also had the SiN_x deposited in one step but the metallization on the front side was not fired.

Samples with a thickness variation of TiO_x are prepared on the half-fabricates and a TCO (ZnO_x:Al) is deposited by ALD on the back side to function as an electrical contact to enable current measurements without metallization. Suns-V_{oc} and iV_{oc} measurements are performed on the half fabricates in the as-deposited state and after a $300°C$ FGA treatment of 15 minutes which optimizes the TiO_x passivation quality. The results are shown in figure 4.3.9 and figure 4.3.10.

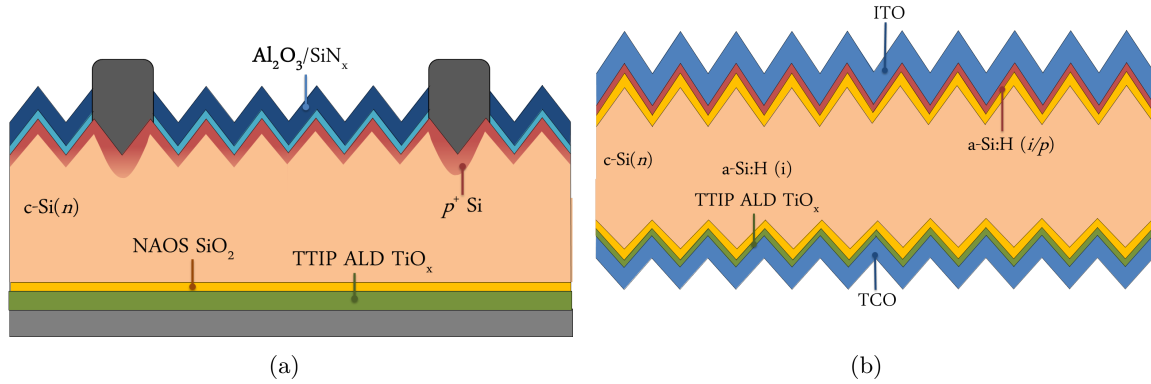

(a) (b)

Figure 4.3.8: *In (a) the n-Pasha cell structure is given schematically. The received samples had a NAOS treatment on the back side. They were transported and stored in atmospheric environment before the TTIP ALD process was run. In (b) a heterojunction cell is given schematically. These samples were transported and stored in a N_2 filled container before the TTIP ALD process was used to deposit the TiO_x films.*

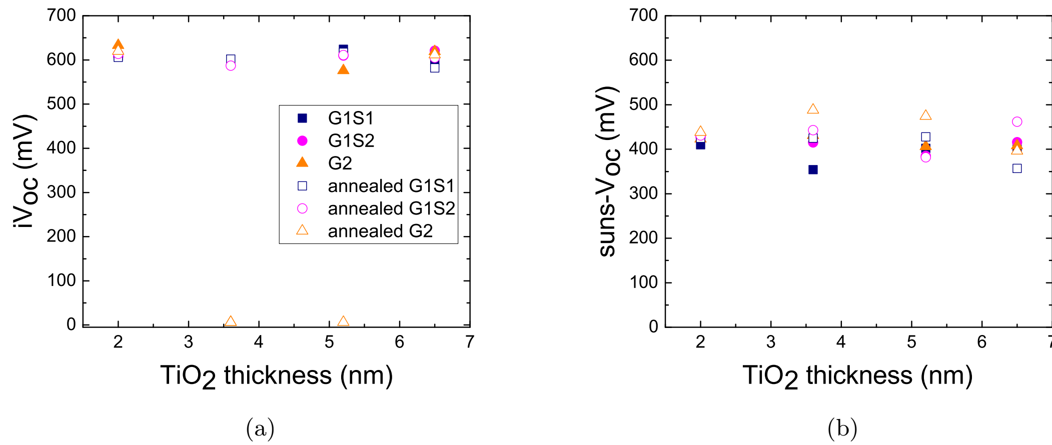

(a) (b)

Figure 4.3.9: *In (a) the iV_{oc} is given for different TiO_x thicknesses deposited on the n-Pasha half-fabricates in the as-deposited state and after a $300°C$ FGA treatment of 15 minutes. In (b) the suns-V_{oc} is given for different as-deposited and annealed TiO_x thicknesses. There are 3 different n-Pasha half-cells supplied; G1S1 is a cell where the SiN_x is deposited in two steps as opposed to one step for G1S2, G2 is a cell which is not fired.*

Looking at the n-Pasha results in figure 4.3.9 it shows no influence from the TiO_x thickness on the iV_{oc} either before and after the annealing treatment. Besides the fact that some cells seem to be defect, an iV_{oc} of $621\,mV$ is achieved. However, the suns-V_{oc} measurements on the n-Pasha cells do show a lesser performance in V_{oc}. A distinction between the processing variation provided by ECN (G1S1, G1S2, G2) can not be made.

The SHJ results in figure 4.3.10 show high iV_{oc} values in the as-deposited state with a maximum of $727\,mV$. No noticeable influence of the TiO_x thickness can be observed. After the anneal treatment on $300°C$ the cells drop in V_{oc} performance which can be due to the thermal instability of the a-Si:H [12]. Moreover, the suns-V_{oc} measurements again show a lesser performance in V_{oc}.

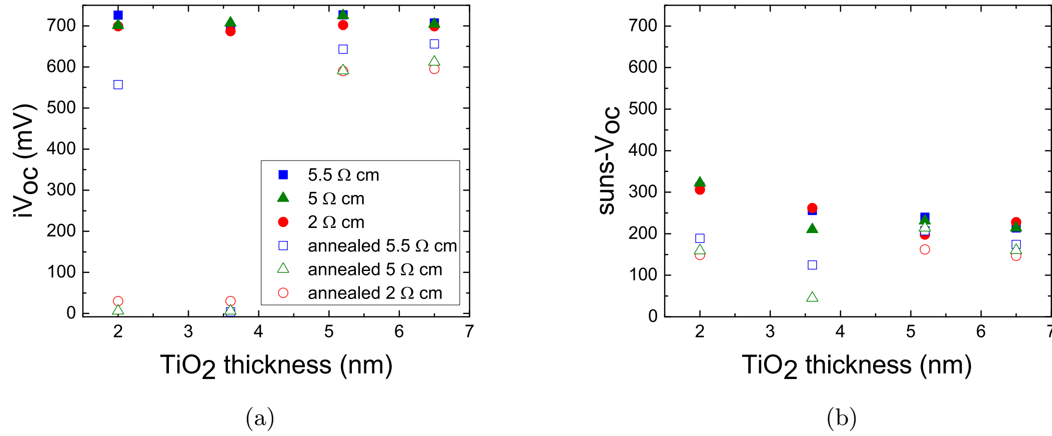

Figure 4.3.10: *In (a) the iV_{oc} is given for different TiO_x thicknesses deposited on the SHJ half-fabricates in the as-deposited state and after a $300°C$ FGA treatment of 15 minutes. In (b) the suns-V_{oc} is given for different as-deposited and annealed TiO_x thicknesses.*

The iV_{oc} is a measure for the quasi-Fermi level splitting in the c-Si for which excellent bulk quality Si and good surface passivation is sufficient to measure high values. The actual V_{oc}, measured with the suns-V_{oc} method, is the measured voltage difference between the front and back side of the solar cell. Here good selectivity for the holes and electrons are additionally required to obtain high values. The iV_{oc} is always higher or equal to the V_{oc} with typically just a few mV difference and can be used as a good estimation for the characterization of the cell. However, the large drop observed in the prepared n-Pasha and SHJ cells show a lack of selectivity for the charge carriers.

The electron-selective quality of the TiO_x layers needs further investigation. A first test could be to perform contact resistance measurements on *p*-type Si instead of *n*-type, the TTIP ALD TiO_x should block the hole current to some extent which indicates its hole-blocking properties. This would induce the asymmetry in hole and electron conductivity which is required as discussed in section 2.2. Avasthi et al. [60] used this method to show the hole-blocking properties of TiO_2 films as was discussed in section 4.1.2. The magnitude of this characteristic could be studied to further improve the selectivity of the TiO_x films. Furthermore, other advanced characterization techniques like UPS and spectroscopy can be used to determine band edge potentials and the respective energy diagrams.
Additionally, it is possible that the unprotected back side without a contact was damaged during transport and handling of the samples. Furthermore, the half-cells acquired from ECN were transported and stored for weeks up to months which can be influential on the performance, especially on the SHJ with a-Si:H layers which could possible oxidise. The n-Pasha samples had a NAOS treatment on the back side and were stored in ambient for a long time which could influence the performance. The damaging of the half-fabricates is a more likely explanation as a n-Pasha like structure without the TiO_x film and the metal back contact directly onto the silicon could already lead up to $V_{oc} = 585\,mV$ and an efficiency of $\eta = 17.5\%$ as was shown by Yang et al. [64]. Their champion cell with a TiO_x film as full-area back contact between the Si and the metal rendered an efficiency of $\eta = 21.6\%$.

4.3.3 Comparison Titanium Precursors

A comparative study is conducted between different precursors and recipes. The passivation quality was determined by the effective minority carrier lifetime for these different precursors and in terms of the ALD recipe and anneal treatment. PEALD and thermal ALD processes were used and exhibited significant differences. The ALD recipe details are shown in table 4.3.1.

Table 4.3.1: *Details of the ALD processes investigated: Various precursors are used and the details of the ALD recipes are given per half cycle. The GPC is determined on a bare FZ Si wafer which had its native oxide removed by a 1 minute HF dip.*

Precursor	T_{dep} ($°C$)	GPC (Å)	First half cycle	Second half cycle
$Ti(Cp^{Me})(NMe_2)_3$	50	0.8	3s precursor dose	O_2 plasma 5s
	[125-350]	0.5		375W
TDMAT	50	0.68	1s precursor dose	H_2O 50ms dose
	75	0.62	10s purge	20s purge
	100	0.56		
	125	0.50		
	150	0.46		
TTIP	200	0.15	2s precursor dose	H_2O 250ms dose
			5s purge	4s reaction time
				20s purge
	250	0.4	4s precursor dose	O_2 plasma 12s
			5s purge	100W 3s purge

Plasma-enhanced ALD

The $Ti(Cp^{Me})(NMe_2)_3$ precursor is only used in a PEALD recipe. No passivation was achieved in the as-deposited state and after annealing (FGA on $275°C$ with $t \geq 100$ minutes) the plasma-induced damage from the ALD process [16, 69] could be repaired up to $\tau_{eff} \approx 360\,\mu s$; this result is shown in the appendix figure 5.0.4. At and above a deposition temperature of $300°C$ the passivation quality decreases as the deposited TiO_x film forms a crystalline anatase phase for $T_h \geq 300°C$ [68], which corresponds to the findings of Liao et al. [62]. At lower deposition temperatures amorphous TiO_x is deposited.

A PEALD recipe is used for the TTIP precursor which is shown in the last section of table 4.3.1. The results for the plasma-enhanced recipe show no passivation in the as-deposited state and after annealing carefully on a temperature just above the deposition temperature (FGA on $275°C$ with $t \geq 1000$ minutes), the effective lifetime could be brought up to $\tau_{eff} \approx 800\,\mu s$ for samples with a NAOS treatment before TiO_x deposition. This result is shown in figure 4.3.11.
A different annealing approach is to use a higher temperatures for a shorter time which is done for 3 minutes on temperatures from $300°C$ to $550°C$. With this approach a maximum lifetime of $\tau_{eff} \approx 900\,\mu s$ is achieved with $5\,nm$ of TiO_x with a NAOS interlayer and a AlO_x capping layer after 3 minutes of FGA treatment on $450°C$. This result is shown in figure 4.3.12.

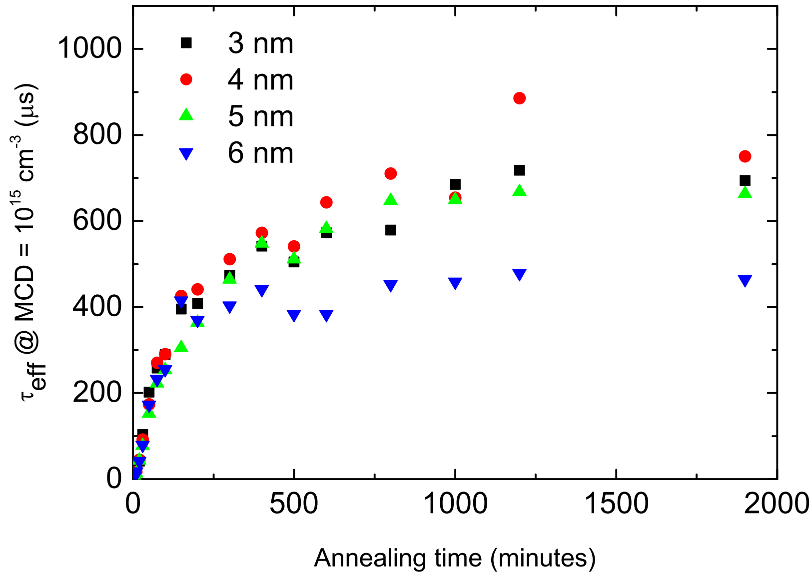

Figure 4.3.11: *Measured effective minority carrier lifetime plotted against anneal time for a $275°C$ FGA. Lifetime samples are made with the TTIP PEALD TiO_x films on clean FZ Si wafers with NAOS treatment.*

A strong TiO_x thickness dependence is noticeable in figure 4.3.12 for film thicknesses between 2.5 and $15\,nm$ with an optimum around $5\,nm$. For an anneal treatment on $550°C$ the passivation quality decreases in comparison with 450-500$°C$ treatments. This can be caused by hydrogen effusion out of the film instead of to the Si interface or crystallization of the

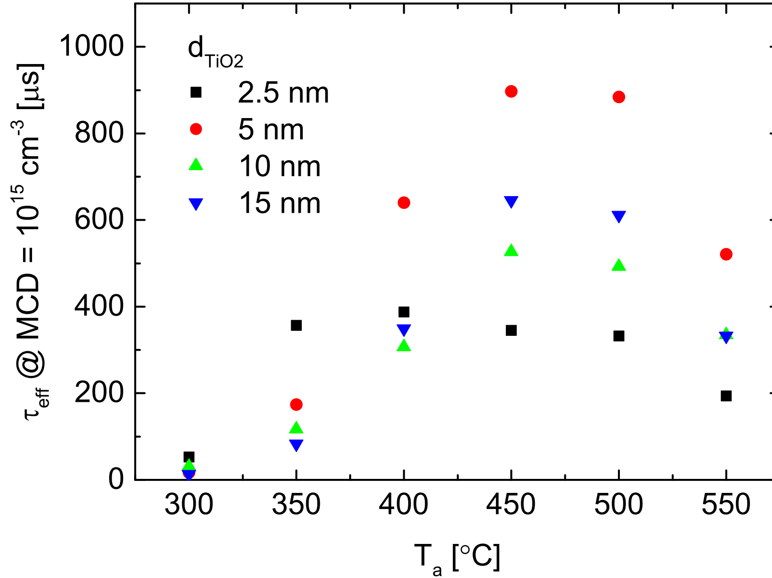

Figure 4.3.12: *Measured effective minority carrier lifetime plotted against anneal temperature for a 3 minute treatment. Lifetime samples are made with the TTIP PEALD TiO_x films on clean FZ Si wafers with NAOS treatment and an ALD AlO_x capping layer.*

TiO_x. In figure 4.3.11 the thickness dependence around the optimum, between 3 and 5 nm, is not apparent any more.

With a short anneal on a higher temperature with an AlO_x capping layer the same passivation result can be acquired as a longer anneal treatment on $275°C$. Although an anneal treatment on too high temperatures can have detrimental effects as is observed for a $550°C$ FGA. The lack of passivation in the as-deposited state is apparent for PEALD. The same precursor (TTIP) used with a thermal ALD recipe showed excellent passivating qualities which were discussed in the previous section. From this one can conclude that a thermal recipe is preferred for the ALD of passivating contacts.

Thermal ALD

Thermal ALD recipes are better for passivation purposes as there is no plasma-induced damage [16, 69] and therefore these are discussed next.

Amorphous TiO_x was deposited with a TDMAT recipe as is shown in table 4.3.1. No passivation is observed in the as-deposited state and after FGA on $200°C$ and $300°C$ lifetimes of $\tau_{eff} \approx 800\,\mu s$ are reached after 300 and 100 minutes annealing, respectively. Some of these results are shown in the appendix figures 5.0.5 and 5.0.6. However, the TiO_x films deposited with the TTIP precursor already showed good passivating qualities in the as-deposited state as was discussed in the previous section. The best performance as-deposited is $\tau_{eff} \approx 900\,\mu s$.

There is a big difference is the as-deposited passivation quality between the thermal ALD recipes with TDMAT and TTIP. TDMAT has the Ti atom bonded to N, which has a lower bond dissociation energy than Ti bonded to O, as is the case in the TTIP molecule [70]. Xie et al. [71] studied the difference in TDMAT and TTIP ALD processes and concluded the

following: To reach the product state of the first half cycle a certain energy barrier needs to be overcome which is activated thermally in the ALD process and the reactivity with H_2O increases with increasing temperature which would cause a higher growth rate. This is not the case for TDMAT. Here, the product state is easily reached at $50°C$ but product desorption, or TDMAT decomposition, becomes more significant with increasing temperature and thus the growth rate decreases. The lower growth rate for TTIP and oxygen in the molecule could enhance the growth of a thermal oxide in the c-Si, as is seen with TEM, which can be important for passivation.

A comparison of the optical constants, n and k, and the bandgap energy E_g can be made for the different TDMAT and TTIP films which are a result from the Tauc-Lorentz SE model. The refractive index at a wavelength of $600\,nm$ and the bandgap energy E_g are given in table 4.3.2 and the extinction coefficients k are given in figure 4.3.13.

Table 4.3.2: *The refractive index n and bandgap energy E_g given for different ALD TiO_x films deposited with the TDMAT and TTIP precursor. The values shown come from the Tauc-Lorentz model which is used to fit the raw SE data.*

Precursor	Deposition Temperature ($°C$)	n @ 600 nm (-)	E_g (eV)
TDMAT	50	2.10	3.11
	75	2.11	3.15
	100	2.18	2.92
	125	2.21	2.99
	150	2.25	2.92
TTIP	200	2.01	3.27

The measured bandgap energy is slightly higher for the with TTIP deposited films and the refractive index slightly lower which can be seen in table 4.3.2. These differences are just minor and could not explain the difference in passivation quality. As can be seen from figure 4.3.13 the TTIP ALD TiO_x films do exhibit lower k values and a somewhat less steep increase in absorption for photon energies higher than the bandgap energy. The steepness of absorption is a quantitative measure of the disorder of an amorphous material [72], so the less steep increase could indicate there is less order in the TTIP ALD TiO_x films than in the TDMAT ALD films. It is known that a crystalline phase is detrimental for the passivation quality of TiO_x on c-Si [62, 68]. However, the difference in the extinction coefficient is small and does not provide any hard evidence for the difference in passivation between the TDMAT and TTIP precursors.

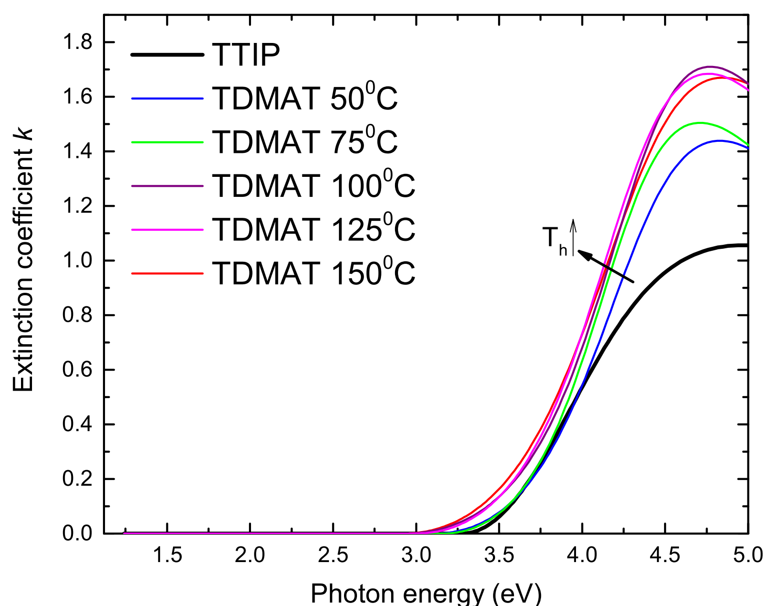

Figure 4.3.13: *Extinction coefficient as a function of photon energy for different ALD TiO_x films deposited with TDMAT and TTIP. The overall trend for the TDMAT films is that there is more absorption for higher deposition temperature for photons with energies higher than the bandgap energy. The TTIP ALD TiO_x film has the highest bandgap energy and a lower extinction coefficient. The absorption curve is also less steep.*

A better comparative study needs to be executed to determine the differences between the TDMAT and TTIP precursor. The biggest benefit of the TTIP thermal ALD recipe is the good passivation property even in as-deposited state. The TDMAT precursor has a significant higher growth rate and a lower deposition temperature which would be beneficial for industrial processing. Furthermore, the passivation quality of the TiO_x films deposited with TDMAT could still be improved by a more extensive anneal treatment study.

4.4 Conclusion and Outlook

Conclusion

Several precursors and ALD recipes were used to deposit amorphous TiO_x films as passivating electron-selective contacts. The passivation quality is strongly dependent on precursor and ALD recipe and there is a clear indication that UV-radiation damage which is induced by the O_2 plasma radiation has a detrimental effect on the minority carrier lifetime and can only be repaired with a FGA treatment up to a certain level. Thermal ALD TiO_x layers need less annealing to improve the passivation quality. For the TTIP precursor, where the Ti atom is bonded to oxygen in the molecule, the passivation quality was superior to that of TDMAT. This effect was most noticeable in the as-deposited state of the TiO_x. Although the TDMAT TiO_x materials could still be optimized further.

With the TTIP ALD TiO_x films a champion lifetime of $\tau_{eff} \approx 2.0\,ms$ is achieved after 15 minutes FGA treatment at $300°C$. This is the best passivation quality of TiO_x films reported so far with an anneal treatment to our knowledge. Furthermore, the contact resistivity is determined of these films with the Cox-Strack method and gives a minimum of $\rho_c = 0.4\,\Omega \cdot cm^2$. This is low enough to potentially create high-efficiency c-Si solar cells.
However, the TiO_x films do not yet show the expected and wanted quality on solar cell level. Suns-V_{oc} measurements show a large drop in V_{oc} compared to the iV_{oc} which indicates a lack of selectivity. The expected band alignment of the TiO_x to the valence band of c-Si and its offset to the conduction band needs more investigation, as is motivated by the excellent lifetime results. This could be done with UPS and spectroscopy.

A better understanding of the TiO_x passivation quality in terms of precursor and ALD recipe has been acquired and excellent passivation results have been achieved. An anneal treatment of up to $500°C$ could be employed without damaging the passivation quality. High temperature anneal treatments cost less time to achieve good passivation and that is beneficial for the processing of solar cells. An additional capping layer of AlO_x did not improve the passivation quality after annealing and is thus unnecessary.

Outlook

As mentioned before; the electron-selective quality of the TiO_x layers needs further investigation. A first test could be to perform contact resistance measurements on p-type Si instead of n-type, the TTIP ALD TiO_x should block the hole current to some extend which indicates its hole-blocking properties. This would induce the asymmetry in hole and electron conductivity which is required as discussed in section 2.2. The magnitude of this characteristic could be studied to further improve the selectivity of the TiO_x films. This method is based on the work of Avasthi et al. [60] which showed the hole-blocking properties of TiO_x on p-type Si.

Different deposition temperatures for the ALD process of TiO_x with TTIP can still be tested. A study on the material quality and the effect on the passivation of c-Si have to be conducted for this variation. Furthermore, the chemical composition can be studied with RBS measurements which could help to understand its effect on passivation and selectivity.

To better identify the contact resistivity a series resistance can be inserted between the contact dot and probe. This way ρ_c could be determined at the operating voltage as the

compliance of the setup, which could not be set higher, is not yet reached with this higher series resistance.

The first step towards a highly conductive Nb-doped ALD TiO_x film is already taken. By doping the TiO_x with Nb the conductivity increases [75] and the electron quasi-Fermi level could line up even further towards the valence band making it more selective for electrons. To properly determine what the band diagrams are in the TTIP ALD TiO_x and the possible Nb-doped TiO_x, energy band diagrams need to be determined by a combination of (COMSOL) simulations and advanced characterization (UPS, IR-SE).

Chapter 5

Overall Conclusion and Outlook

Ruthenium oxide ALD and material properties

A novel thermal ALD process was successfully developed for RuO_x using the zero-valent metal-organic (ethylbenzene)(1,3-cyclohexadiene)Ru(0) precursor and O_2 gas on the home-built ALDii reactor. High pressure reactant steps of molecular oxygen, $p_{O_2} = 1\,mbar$, were used to provide enough exposure to oxidise the Ru in the ALD process. Self-limiting ALD behaviour was confirmed and a relatively long standard ALD recipe was obtained with a $15\,s$ precursor dosing step and $40\,s$ oxygen exposure time. A temperature window in which deposition occurred has been experimentally determined from $150°C$ to $300°C$ table temperature. For deposition temperatures between $200°C$ and $300°C$ a GPC between 1.62 Å to 2.22 Å was found.
Polycrystalline RuO_x was deposited, initially in the Volmer-Weber mode which defines the island growth, in the obtained temperature deposition range. XRD and electron diffraction showed multiple crystalline RuO_2 orientations but also a Ru metal contribution in all deposited RuO_x films. This Ru metal phase could not be prevented with higher oxygen exposure or temperature differences. No C contamination was found with RBS which also showed an increase in O/Ru ratio with increasing O_2 dosing time and decreasing temperature. Moreover, a H content between 4 at.% and 10 at.% was found using ERD. The RuO_x films had an average resistivity of $(338 \pm 43)\,\mu\Omega \cdot cm$ determined with four point probe measurements which is an order of magnitude higher than the literature values, this is caused by the rough an probably not fully closed films. Furthermore, a high charge carrier density in the order of 10^{21}-$10^{23}\,cm^{-3}$ which was determined with Hall measurements. Moreover, a high absorption coefficient was obtained from the extinction coefficient k determined by a SE B-Spline model.

Ruthenium oxide potential in c-Si solar cells

The potential of the ALD RuO_x layers as passivating contact was briefly addressed. The film on itself did not passivate the c-Si but a RuO_x/a-Si:H/c-Si stack achieved an excellent minority carrier lifetime of $1.8\,ms$ with an a-Si:H layer of $5\,nm$ thick. The potential hole-selectivity of RuO_x was not confirmed yet. This selectivity depends on the upward band bending due to a high work function. The work function of the ALD RuO_x was not measured yet which could be done by XPS or UPS. This needs to be one of the first steps towards determining the potential of RuO_x as hole-selective contact.
Furthermore, the contact resistivity ρ_c is also of importance to a passivating contact as it

could lead to significant losses due to series resistance if it were is high. The Cox-Strack method could be used to measure the ρ_c of the stack: metal contact/RuO_x/c-Si. To prevent current spreading in the conductive RuO_x layer the film needed to be etched away in between the metal contacts to have a well defined surface area. This etching step has not yet been performed. The determination of ρ_c is necessary to show that current transport can occur efficiently through the RuO_x contact.
The high absorption of the films already showed that the hole-selective RuO_x layers should be used on the back side of the cell as it does not contribute much to the optical losses there.

Titanium oxide ALD process and precursors

Different ALD recipes and precursors were used to deposit TiO_x with an Oxford Instruments FlexAl ALD system for the purpose of an electron-selective passivating contact. It was concluded that amorphous films deposited with thermal ALD recipes had the best passivation performance on c-Si surfaces. Two different industrial Ti-precursor, tetrakis(dimethylamino) titanium (TDMAT) and titanium isopropoxide (TTIP), were used in thermal ALD processes. TDMAT was used in a [50 - 300]$°C$ temperature window with a GPC between 0.68 Å to 0.46 Å which decreased with increasing temperature. TTIP did not show any growth at 80$°C$ and had a GPC of 0.15 Å at 200$°C$. From the Tauc-Lorentz model used to determine the optical constants and thickness of the films with SE, the band gap energy E_g, refractive index n and extinction coefficient k were determined. The TTIP ALD TiO_x film had the highest $E_g = 3.27\,eV$, lowest $n = 2.01$ at $\lambda = 600\,nm$ and a lower k in comparison with TDMAT but these were just minor differences.
The passivation quality, especially in as-deposited state, was superior for the TTIP ALD TiO_x layers. Deposited on a n-type FZ Si wafer, which had its native oxide removed by a 1 minute dip in a 1% HF solution, the thermal TTIP ALD process oxidized the Si wafer to form a SiO_2 interlayer between the c-Si and the TiO_x which was observed with TEM. This could be the biggest factor in the as-deposited and overall better passivation quality of the TTIP precursor. The influence of deposition temperature on the TiO_x films deposited with TTIP has not been studied yet. Furthermore, the TDMAT precursor has not been intensively investigated yet and could be improved significantly in terms of passivation. Moreover, RBS measurements could be performed to get more insight on the chemical composition of the amorphous TiO_x films and its influence on the passivating and selective qualities.

Titanium oxide with TTIP in c-Si solar cells

An extensive study on the annealing effects has been conducted on the passivation qualities of TiO_x on c-Si. The TTIP precursor showed passivation of the surface even in the as-deposited state which is why this precursor was more extensively studied. The important parameters for a passivating contact are the recombination current density J_0 and the contact resistivity ρ_c which were determined for these TiO_x films.
Firstly, the passivation quality was determined in terms of effective minority carrier lifetime (τ_{eff}), iV_{oc} and J_0. TiO_x films deposited with TTIP on high quality n-type FZ Si wafers with the SiO_2 interlayer created during the ALD process performed better than the NAOS interlayer created before TiO_x deposition. The fact that the growth of this interlayer happened during the ALD process is beneficial as it does not require any additional processing steps. iV_{oc} measurements on lifetime samples showed excellent quality and with $5.2\,nm$

TiO_x the highest lifetime after 15 minutes FGA on $300°C$, $\tau_{eff} \approx 2.0\,ms$, was measured. This was a superior passivation quality of c-Si with TiO_x compared to reported literature with only an anneal treatment. The highest iV_{oc} achieved was $698\,mV$ and the champion $J_0 = 12.3\,fA/cm^2$ was measured on this sample. Thicker layers ($7.5\,nm$) were seen to crystallize after long 100 minutes FGA treatments on $300°C$ which was detrimental for the passivation quality.
The Cox-Strack method was used to determine ρ_c of the Al/TiO_x/c-Si stack for which the minimum and best value measured was $0.4\,\Omega \cdot cm^2$. Together with the achieved J_0 could a full area TiO_x electron contact could lead to a cell efficiency of $\eta = 26 - 27\%$ under the assumption that the front side of the cell is without any loss in the idealized case.
Suns-V_{oc} and iV_{oc} measurements were performed on n-Pasha and SHJ half-fabricates which had an electron-selective back contact with TTIP ALD TiO_x. For both type of cells high iV_{oc} were achieved, the n-Pasha cell reached a maximum of $621\,mV$ and the SHJ cells $727\,mV$. There seemed to be no influence of the TiO_x layer thickness, between 2 and $6.5\,nm$, on cell level. Suns-V_{oc} measurements resulted in low values which indicated a lack of selectivity in the cell. The electron-selective quality of the TiO_x layers needs further investigation. A first test could be to perform contact resistance measurements on *p*-type Si instead of *n*-type, the TTIP ALD TiO_x should block the hole current to some extend which indicates its hole-blocking properties. The magnitude of this characteristic could be studied to further improve the excellent passivating TiO_x films. It has already shown its industrial potential as full area passivating contact which is the motivation for further studies on this material.

Acknowledgements

After a year and a bit of conducting my graduation project I got a list of people who I really need to thank for all their efforts and support. I could not have done this all by myself, the list would probably keep on growing if I keep looking back at it but I do want to give some honourable mentions. First of all, I got the opportunity to do this project at the PMP group for which I thank Erwin. Not only for the opportunity and being the leader of this amazing team but also for his supervision and positive criticism which helps keep an outstanding standard of work here at PMP. Secondly, the technicians, especially Christian and Jeroen for assistance with experiments and keeping the systems running, even when I broke down two ALD systems in one day (sorry for that!).

When I started this project I did not know much about solar cells, but there was no need to worry because PMP provides some excellent teachers. Therefore, I especially want to thank "de Passivisten" Bas, Bart and Jimmy. Now I've mentioned Jimmy I want to say a few words about my daily supervisor. My coffee consumption increased when I started at the TUe and eventually saturated on what I thought was a pretty high level. Well, then I met Jimmy whom seemed to live more on coffee than on water or anything else for that matter. All kidding aside, I would not have wanted any other supervisor for this project and I really want to thank you for everything. One of the few persons I shared a bed with, thanks Jimmy!

My recognition also goes out to all the other helpful hands in the PMP group like René, Nick and Martijn for the help with the ALDii and Marcel for the amazing TEM images.

Luckily it wasn't always hard work and I found myself surrounded by people who like to have fun. The other (graduated) master students at PMP, but also EPG, provided some fun coffee, ping-pong and "borrel" brakes. Unfortunately there are too many to name, but special thanks to Geert, Pim, Yannick, Siebe, and fellow "passivist" Willem-Jan. Furthermore, I loved taking a break and play some futsal with "PEST" and "de Goddelijke Condors" so thank you for some awesome matches and good luck in the future!

Of course I can't forget the people at home (thuis-thuis) back in Limburg. Thank you, pap en mam, for all the love and support. A shout-out to my brother Jeroen for the support and even professional input on my thesis and to my other friends back home for anything but professional input.

I would like to end my thesis by saying I greatly enjoyed my time here. I learned more than I could have hoped for and the level of expertise and the facilities here are great! I'm sorry for leaving but new, exciting adventures await with a beautiful degree in the pocket.

Appendix

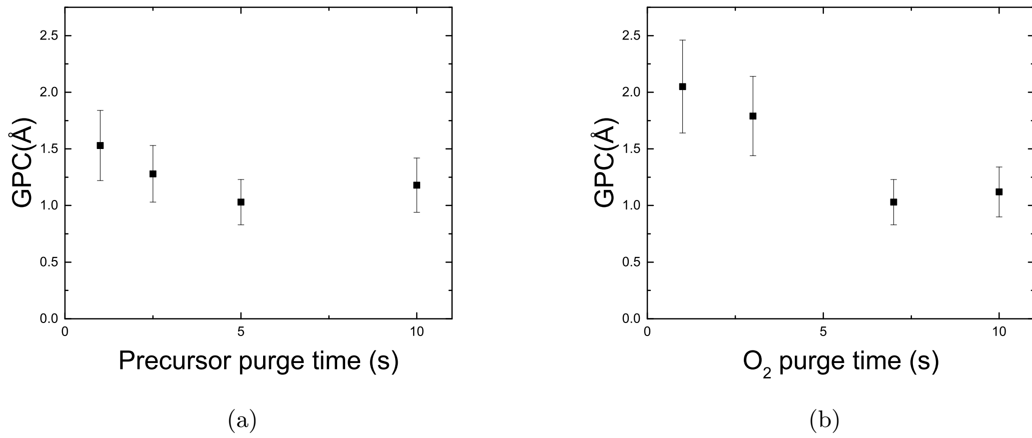

(a) (b)

Figure 5.0.1: *Saturation curves for precursor and reactant purge times in the ALDii reactor where the substrate table is set to $T_h = 200°C$ and the oxygen pressure is kept constant at $p_{O_2} = 1\,mbar$. In (a) the saturation curve of the precursor purge time. In (b) the saturation curve of the oxygen purge time.*

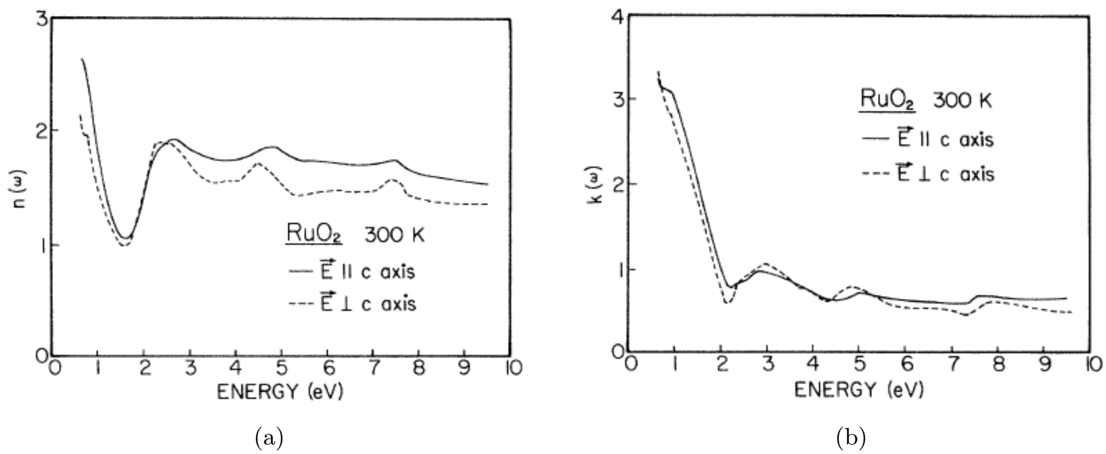

(a) (b)

Figure 5.0.2: *In (a) the measured refractive index n and in (b) the measured extinction coefficient k are given for single-crystal rutile RuO_2 in the range of 0.5 to $9.5\,eV$ by Goel et al. [52]*

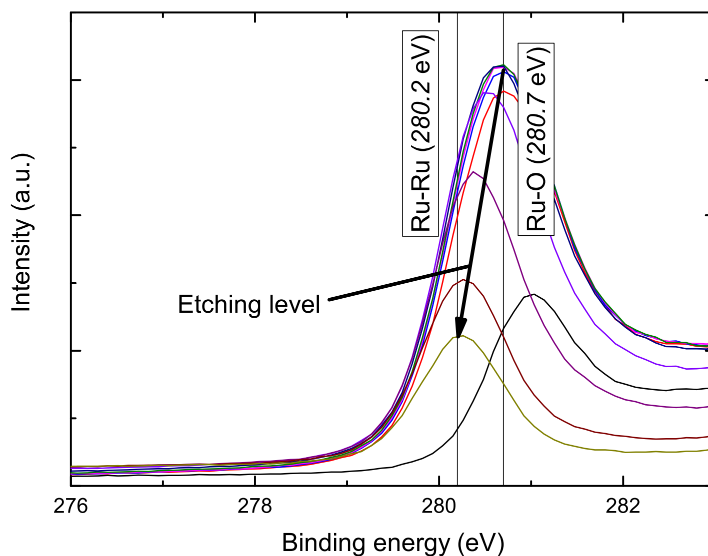

Figure 5.0.3: *XPS depth profile of a standard ALD recipe RuO_x film. The binding energy on the top surface is that of Ru-O bond which transitions to the binding energy of a Ru-Ru bond when the film is sputtered away down to the substrate surface.*

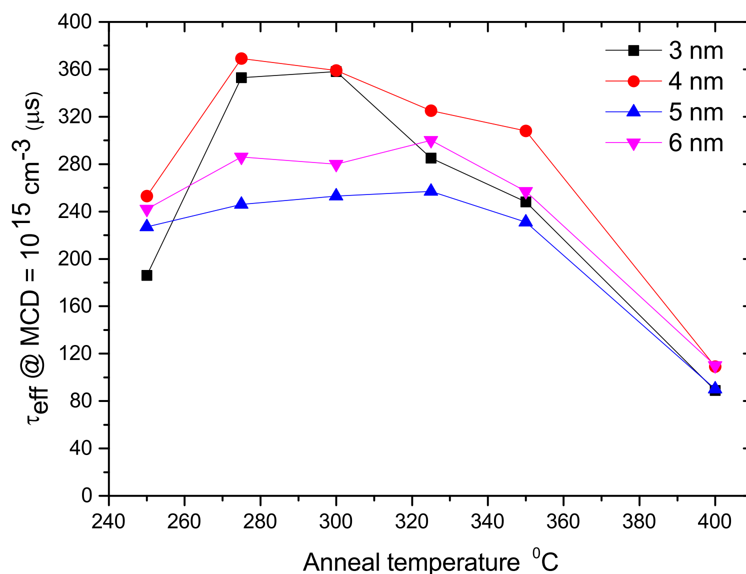

Figure 5.0.4: *Measured effective minority carrier lifetime plotted against FGA temperature treatment for 100 minutes. Lifetime samples are made with the Ti(Cp^{Me})(NMe2)3 precursor on bare FZ Si wafers.*

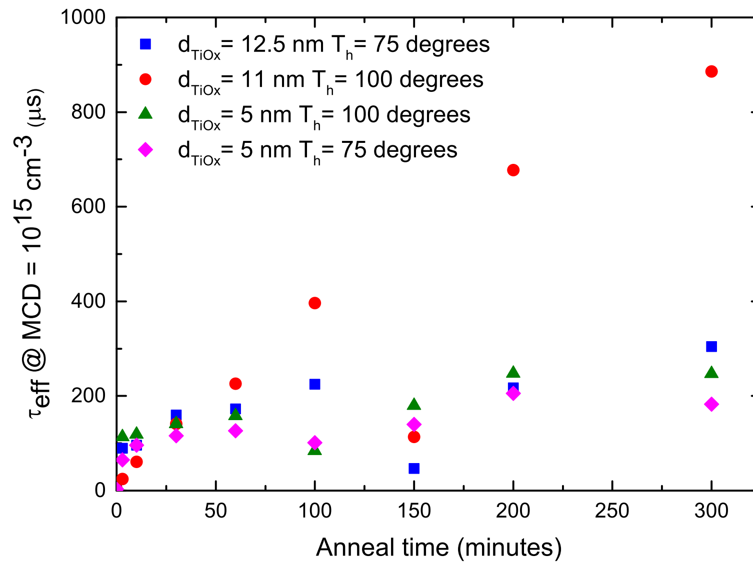

Figure 5.0.5: *Measured effective minority carrier lifetime plotted against anneal time for a 200°C FGA. Lifetime samples are made with the TDMAT ALD TiO_x films on bare FZ Si wafers.*

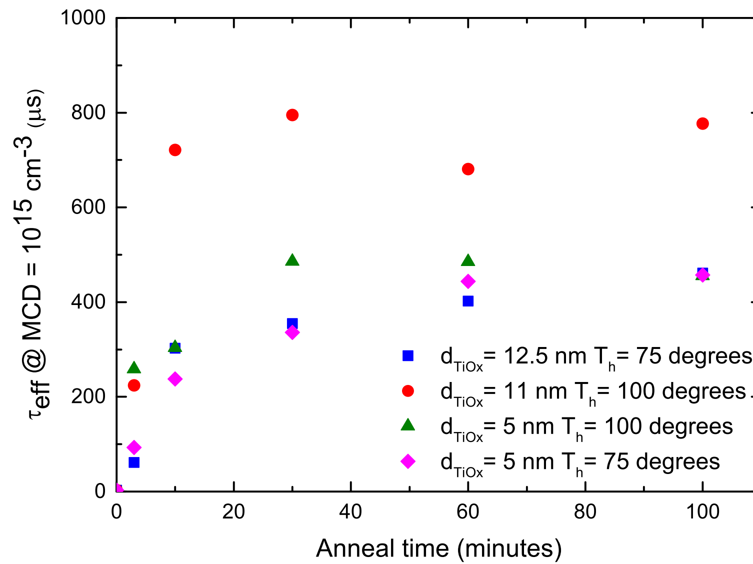

Figure 5.0.6: *Measured effective minority carrier lifetime plotted against anneal time for a 300°C FGA. Lifetime samples are made with the TDMAT ALD TiO_x films on bare FZ Si wafers.*

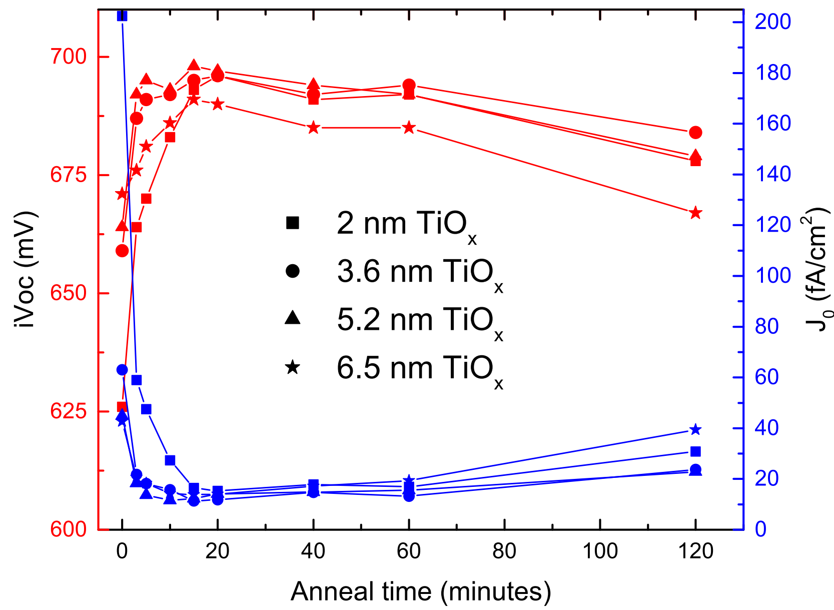

Figure 5.0.7: *Measured values for the iV_{oc} and J_0 plotted against anneal time for a 300°C FGA. Lifetime samples are made with the TTIP ALD TiO_x films on bare FZ Si wafers.*

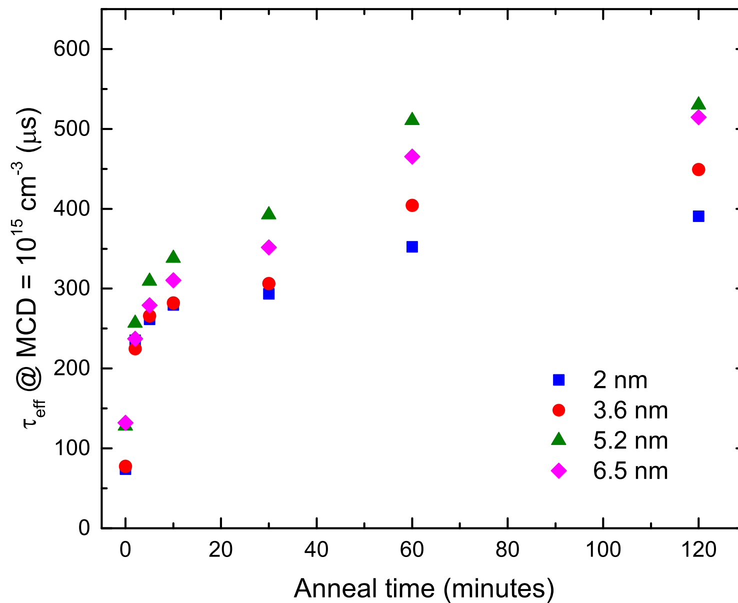

Figure 5.0.8: *Measured effective minority carrier lifetime plotted against anneal time for a 300°C FGA. Lifetime samples are made with the TTIP ALD TiO_x and a 20 nm thick AlO_x capping layer deposited with a thermal TMA ALD recipe.*

Bibliography

[1] Fraunhofer, ©Fraunhofer ISE: Photovoltaics Report, (2016).

[2] A. Richter et al. IEEE Journal of Photovoltaics 3, 1184, (2013).

[3] Kaneka Corporation, *World's Highest Conversion Efficiency of 26.33% Achieved in a Crystalline Silicon Solar Cell. A World First in a Practical Cell Size*, News Release: New Energy and Industrial Technology Development Organization (NEDO), September 14, (2016)

[4] M. A. Green et al. *Solar cell efficiency tables (version 46)*, (2015)

[5] M. A. Green et al. *Third Generation Photovoltaics: Advanced Solar Energy Conversion*, Springer p65. (2003)

[6] Atteq ur Rehman and Soo Hong Lee *Advancements in n-Type Base Crystalline Silicon Solar Cells and Their Emergence in the Photovoltaic Industry*, The Scientific World Journal, Volume 2013, Article ID 470347, 13 pages, (2013)

[7] J. Schmidt et al. *Structure and transformation of the metastable boron- and oxygen-related defect center in crystalline silicon*, Physical Review B, Vol. 69, Iss. 2, 024107, (2004)

[8] D. Macdonald et al. *Recombination activity of interstitial iron and other transition metal point defects in p - and n -type crystalline silicon*, Applied Physics Letter, Vol.85, No.18, 4061, (2004)

[9] S. De Wolf et al. *High-efficiency Silicon Heterojunction Solar Cells: A Review*, Green, Vol.2, p.7-24, (2012)

[10] B. Macco, B.W.H. van de Loo and W.M.M. Kessels, *Atomic Layer Deposition for High Efficiency Crystalline Silicon Solar Cells* in J. Bachmann, *Atomic Layer Deposition in Energy Conversion Applications*, Wiley, (2016)

[11] J. Melskens et al. *Passivating Contacts for Crystalline Silicon Solar Cells: From Concepts and Materials to Prospects*, under review, (2017)

[12] J. Melskens et al. *New Insights in the Nanostructure and Defect States of Hydrogenated Amorphous Silicon Obtained by Annealing*, IEEE JPV, Vol.3, Iss.1, p.65-71, (2013)

[13] Zachary C. Holman et al. *Infrared light management in high-efficiency silicon heterojunction and rear-passivated solar cells*, Journal of Applied Physics, Vol.113, Iss.1, (2013)

[14] P. Poodt et al. *Spatial atomic layer deposition: a route towards further industrialization of atomic layer deposition*, Journal of Vacuum Science and Technology A: Vacuum, Surfaces, and Films, 30(1), 010802-1/11, (2012)

[15] D. Munoz-Rojas et al. *Spatial atmospheric atomic layer deposition: a new laboratory and industrial tool for low-cost photovoltaics*, The Royal Society of Chemistry, Vol.1, p.314-320 (2014)

[16] G. Dingemans and W.M.M. Kessels *Status and prospects of Al2O3-based surface passivation schemes*, J. Vac. Sci. Technol. A, Vol.30, No.4, 040802, (2012)

[17] U. Würfel et al. *Charge Carrier Separation in Solar Cells*, IEEE Journal of Photovoltaics, Vol.5, No.1 (2015)

[18] P. Würfel *Physics of Solar Cells*, Wiley, (2009)

[19] W. Schokley et al. *Statistics on the Recombination of Holes and Electrons*, Phys Rev, Vol.87, Iss.5, p.835-842 (1952)

[20] G. Dingemans et al. *Excellent Si surface passivation by low temperature SiO2 using an ultrathin Al2O3 capping film*, physica status solidi (RRL) - Rapid Research Letters, Vol.5, Iss.1 (2011)

[21] B. Hoex et al. *Silicon surface passivation by atomic layer deposited Al[sub2]O[sub3]*, Journal of Applied Physics, Vol. 104, Iss. 4, (2008)

[22] G. Agostinelli et al. *Very low surface recombination velocities on p-type silicon wafers passivated with a dielectric with fixed negative charge*, Solar Energy materials and Solar Cells Vol. 90, Iss.18-19, p.3438-3443, (2006)

[23] A. Fell, K.R. McIntosh et al. *Input Parameters for the Simulation of Silicon Solar Cells in 2014*, IEEE Journal of Photovoltaics, Vol.5, Iss.4, p.1250-1263, (2015)

[24] D. Adachi et al. *Impact of carrier recombination on fill factor for large area heterojunction crystalline silicon solar cell with 25.1% efficiency*, Applied Physics Letters, Vol. 107, Iss.23, (2015)

[25] S.W. Glunz et al., Presented at the 31st European Photovoltaic Solar Energy Conference and Exhibition (2015)

[26] S. Bowden et al. *implied-Voc and suns-Voc measurements in multicrystalline solar cells*, 29th IEEE Photovoltaic Specialist Conference, p.317-374, (2002)

[27] Mark J. Kerr et al. *Generalized analysis of quasi-steady-state and transient decay open circuit voltage measurements*, Journal of Applied Physics, Vol.91, No.1, p.399 (2002)

[28] IUPAC. *The Compendium of Chemical Terminology*, (1987)

[29] T. Arikado et al. *Electrochemical behaviour of the ruthenium oxide electrode prepared by the thermal decomposition method*, Electrochemica Acta, Vol.22, Iss.5, p.513-518, (1976)

[30] H. Kim *Atomic layer deposition of metal and nitride thin films: Current research efforts and applications for semiconductor device processing*, J. of Vac. Sc. & Tech. B: Microelectronics and Nanometer Structures Processing, Measurement and Phenomena, Vol. 21, Iss. 6, p.2231-2261 (2003)

[31] T. N. Arunagiri et al. *5 nm ruthenium thin film as a directly plateable cupper diffusion barrier*, Applied Physics Letters, Vol. 86, Iss. 8, (2005)

[32] Dong-Soo Yoon et al. *Oxidation resistance of tantalum-ruthenium dioxide diffusion barrier for memory capacitor bottom electrodes*, Applied Physics Leters, Vol. 73, Iss. 3, p.324-326, (1998)

[33] D. Kuang et al. *Progress in Ruthenium Complexes in Dye Sensitised Solar Cells*, Platinum Metals Rev., Vol.53, Iss.4, p.216, (2009)

[34] C. Lokhande et al. *Chemical synthesis of nano-porous ruthenium oxide (RuO2) thin films for supercapacitor applications*, Applied Surface Science, Vol.254, Iss.9, p.2820-2824, (2016)

[35] Gujar et al. *Spray deposited amorphous RuO2 for an effective use in electrochemical supercapacitor*, Electrochemistry Communications, Vol. 9, Iss. 3, p.504-510, (2007)

[36] Y.T. Kim et al. *Effects on non-stoichiometric RuOx thin films on the dielectric properties of of BaTiO3 thin films*, (1996)

[37] J. Hämäläinen, *Atomic Layer Deposition of Noble Metal Oxide and Noble Metal Thin Films*, Academic Dissertation, unpublished (2013)

[38] Noémie Leick-Marius *Atomic Layer Deposition of Ruthenium Films, Properties and Surface Reactions*, PhD thesis, unpublished (2014)

[39] M. Minjauw et al. *Atomic layer deposition of ruthenium at 100°C using the RuO4-precursor and H2*, J. Mater. Chem. C, Vol.3, p.132-137, (2015)

[40] H. Over et al. *Oxidation of Metal Surfaces*, Science, Vol.297, p.2003, (2003)

[41] T. Eom et al. *Low Temperature Atomic Layer Deposition of Ruthenium Thin Films Using Isopropylmethylbenzene-Cyclohexadiene-Ruthenium and O[sub 2]*, Electrochemical and Solid-State Letters, Vol.12, Iss.11, p.85-88, (2009)

[42] Ji-Yoon Park et al. *Growth of highly conformal ruthenium-oxide thin films with enhanced nucleation by atomic layer deposition*, Journal of Alloys and Compounds, Vol.610, p.529-539, (2014)

[43] S. Yeo et al. *Ruthenium and rutheniuim dioxide thin films deposited by atomic layer deposition using a novel zero-valent metalorganic precursor, (ethylbenzene)(1,3-butadiene)Ru(0), and molecular oxygen*, Microelectronic Engineering, Vol.137, p.16-22, (2015)

[44] C. Stampfl et al. *Structure and Stability of a High-Coverage (1x1) Oxygen Phase on Ru(0001)*, Physical Review Letters, Vol.77, No.16, p.3371-3374, (1996)

[45] R. Methaapanon et al. *The low temperature atomic layer deposition of ruthenium and the effect of oxygen exposure*, J. Mater. Chem., Vol.22, p.25154-25160, (2012)

[46] B. Macco et al. *Low-temperature atomic layer deposition of MoOx for silicon heterojunction solar cells*, Phys. Status Solidi RRL, Vol.9, No.7, p.393–396 (2015)

[47] M. Mews et al. *Oxygen vacancies in tungsten oxide and their influence on tungsten oxide/silicon heterojunction solar cells*, Solar Energy Materials and Solar Cells, Vol.158, Part.1, p.77-83, (2016)

[48] Y. Xu et al. *Inorganic Materials Database for Exploring the Nature of Material*, Jpn. J. Appl. Phys. Vol.50, No.11S, (2011)

[49] W. M. Haynes. *CRC Handbook of Chemistry and Physics*, 92nd edition, (2011)

[50] K. Oura et al. *Surface Science: An Introduction*, Springer, p.452, (2010)

[51] J. A. Woollam Co., Inc. *CompleteEASE^{tm} Data Analysis Manual*, version 3.65, (2008)

[52] A. K. Goel et al. *Optical properties of single-crystalline rutile RuO2 and IrO2 in the range 0.5-9.5 eV*, Physical Review B, Vol.24, No.12, p.7342-7350, (1981)

[53] R. Methaapanon et al. *Size Dependent Effects in Nucleation of Ru and Ru Oxide Thin Films by Atomic Layer Deposition Measured by Synchotron Radiation X-Ray Diffraction*, Chem. Mater., Vol.25, p.3458-3463, (2013)

[54] D.W. Turner. *Molecular Photoelectron Spectroscopy*, Philosophical Transactions of the Royal Society of London. Series A, Mathematical and Physical Sciences (1970)

[55] Y. Yi et al. *Characterization of indium tin oxide surfaces and interfaces using low intensity x-ray photoemission spectroscopy*, Journal of Applied Physics, Vol.100, Iss.9, p.093719-093719-7, (2006)

[56] W. Luft *Status of TiO2 antireflection coating in the U.S.*, 10th IEEE Photovoltaics Specialists Conference, p.168–173, IEEE, (1973)

[57] B. Lenkeit et al. *Comparison of Remote Versus Direct PECVD Silicon Nitride Passivation of Phosphorus Diffused Emitters of Silicon Solar Cells*, 2nd World Conference on Photovoltaic Energy Conversion, Vienna, (1994)

[58] J. Cui et al. *Titanium oxide: A re-emerging optical and passivating material for silicon solar cells*, Solar Energy Materials and Solar Cells, Vol. 158, Part.1, p.115-121, (2016)

[59] H.-H. Wang et al. *Improving the TiO2 electron transport layer in perovskite solar cells using acetylacetonate-based additives*, J. of Mat. Chem. A., Vol.3, p.9108-9115, (2015)

[60] S. Avasthi et al. *Hole-blocking titanium-oxide/silicon heterojunction and its application to photovoltaics*, Applied Physics Letters, Vol.102, 203901, (2013)

[61] Ing-Song Yu et al. *Surface Passivation of c-Si by Atomic Layer Deposition Ti02 Thin Films Deposited at Low Temperature*, 40th Photovoltaic Specialist Conference (2014)

[62] B. Liao et al. *Excellent c-Si surface passivation by low-temperature atomic layer deposited titanium oxide*, Applied Physics Letters, Vol.104, Iss.25, (2014)

[63] X. Yang et al. *Silicon heterojunction solar cells with electron selective TiOx contact*, Solar Energy Materials and Solar Cells, Vol.150, p.32-38, (2016)

[64] X. Yang et al. *High-Performance TiO2-Based Electron-Selective Contacts for Crystalline Silicon Solar Cells*, Advanced Materials Vol. 28, Iss. 28, p.5891–5897, (2016)

[65] K. Gad et al. *Ultrathin Titanium Dioxide Nanolayers by Atomic Layer Deposition for Surface Passivation of Crystalline Silicon*, IEEE Journal of Photovoltaics, Vol.6, Iss.3, p.649-653, (2016)

[66] A. Sarkar et al. *Plasma-Enhanced ALD of TiO2 Using a Novel Cyclopentadienyl Alkylamido Precursor [Ti(CpMe)(NMe2)3] and O2 Plasma*, ECS Trans., Vol.33, Iss.2, p.385-393, (2010)

[67] R. H. Cox and H. Strack *Ohmic Contacts for GaAs Devices*, Solid State Electronics, Vol.10, p.1213-1218, (1986)

[68] J. Melskens *Feasibility Study of Titanium Dioxide as Passivating Electron-Selective Contact for Crystalline Silicon Solar Cells*, Presented at Silicon PV 7-9 March, (2016)

[69] Gijs Dingemans et al. *Influence of the Oxidant on the Chemical and Field-Effect Passivation of Si by ALD Al2O3*, Electrochem. Solid-State Lett., Vol.14, Iss.1, p.H1-H4, (2011)

[70] John A. Dean *Lange's Handbook of Chemistry*, fifteenth edition (1999)

[71] Q. Xie et al. *Atomic Layer Deposition of TiO2 from tetrakis-dimethyl-amido titanium or Ti isopropoxide precursors and H2O*, J. Appl. Phys., Vol.102, 083521, (2007)

[72] A. R. S. Kandada et al. *Unconventional Thin Film Photovoltaics*, RSC Energy and Environment Series, No16. Chapter 4, p.110, (2016)

[73] J. Schmidt et al. *Surface passivation of silicon solar cells using plasma-enhanced chemical-vapour-deposited SiN films and thin thermal SiO2/plasma SiN stacks*, Semicond. Sci. Techn., Vol.16, No.3, p.164-170, (2000)

[74] M-I Yeong et al. *Passivation behavior of thermally grown SiO2 layer using wet and dry oxidation processes*, 218th ECS Meeting Abstract No.1654, (2010)

[75] J-P Niemela et al. *Conducting Nb-doped TiO2 thin films fabricated with an atomic layer deposition technique*, Thin Solid Films, Vol.551, p.19-21, (2014)